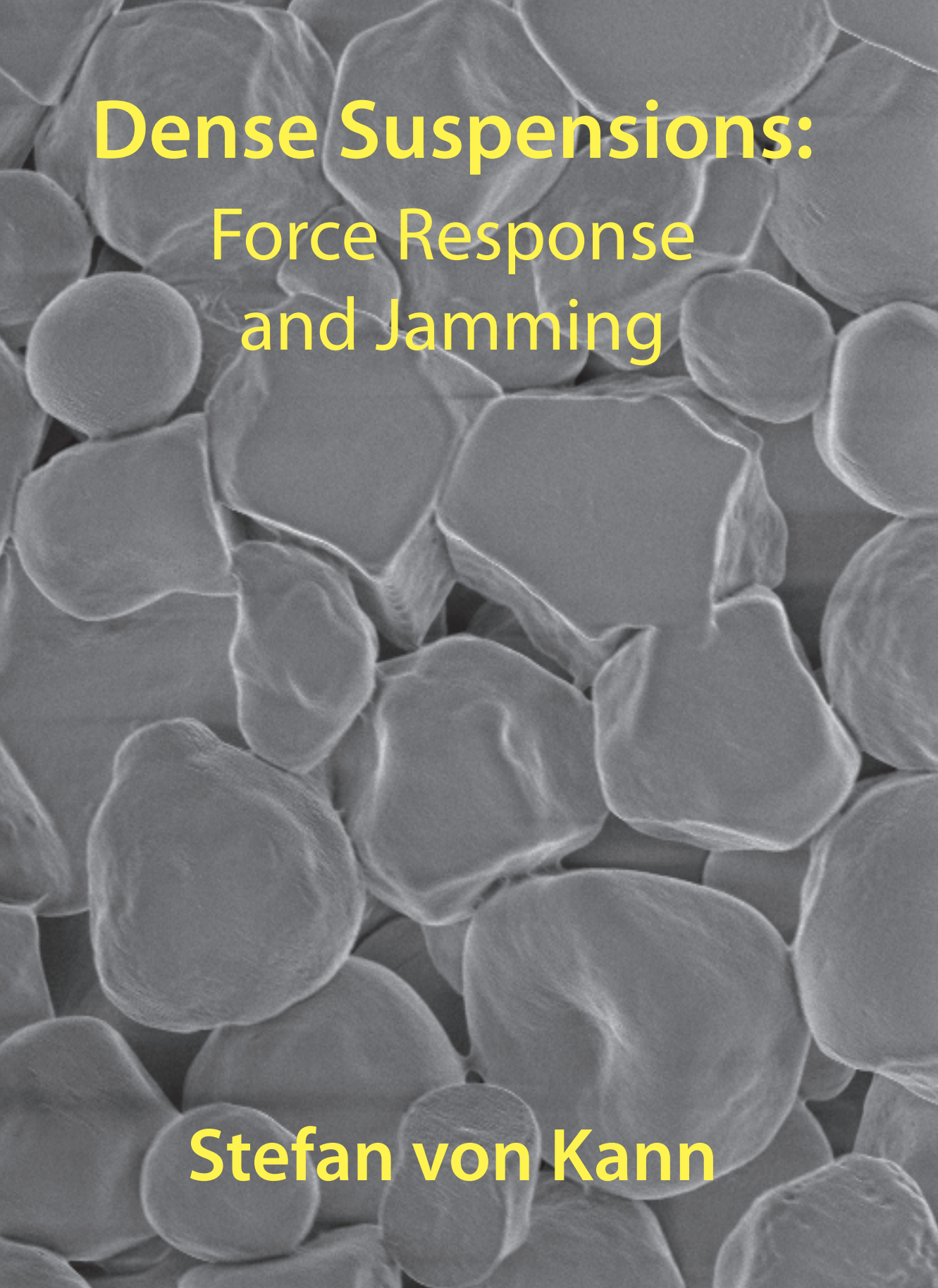

# Dense Suspensions:
## Force Response and Jamming

Stefan von Kann

# Dense suspensions: Force response and jamming

Stefan von Kann

**Samenstelling promotiecommissie:**

| | |
|---|---|
| Prof. dr. Leen van Wijngaarden (voorzitter) | Universiteit Twente |
| Prof. dr. Devaraj van der Meer (promotor) | Universiteit Twente |
| Prof. dr. Detlef Lohse (co-promotor) | Universiteit Twente |
| Dr. ir. Jacco Snoeijer (assistent-promotor) | Universiteit Twente |
| Prof. dr. Douglas J. Durian | University of Pennsylvania |
| Prof. dr. Martin van Hecke | Universiteit Leiden |
| Prof. dr. Allard P. Mosk | Universiteit Twente |
| Dr. ir. Herman L. Offerhaus | Universiteit Twente |

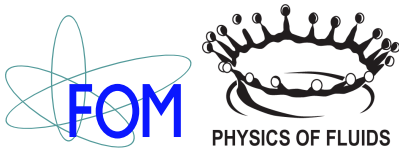


UNIVERSITY OF TWENTE.

The work in this thesis was carried out at the Physics of Fluids group of the Faculty of Science and Technology of the University of Twente. It is part of the research programme of the Foundation for Fundamental Research on Matter (FOM), which is financially supported by the Netherlands Organisation for Scientific Research (NWO).

Nederlandse titel:
*Geconcentreerde suspensies: Reactie op krachten en jamming*

Publisher:
Stefan von Kann, Physics of Fluids, University of Twente,
P.O. Box 217, 7500 AE Enschede, The Netherlands
http://pof.tnw.utwente.nl
stefanvkann@gmail.com

*Cover:* Scanning Electron Microscope picture of cornstarch
*Printed by:* Gildeprint Drukkerijen - Enschede


ISBN: 978-90-365-3471-0

# DENSE SUSPENSIONS: FORCE RESPONSE AND JAMMING

PROEFSCHRIFT

ter verkrijging van
de graad van doctor aan de Universiteit Twente,
op gezag van de rector magnificus,
Prof. dr. H. Brinksma,
volgens besluit van het College voor Promoties
in het openbaar te verdedigen
op vrijdag 21 december 2012 om 16.45

door

Stefan von Kann
geboren op 13 november 1985
te Winterswijk, Nederland

Dit proefschrift is goedgekeurd door de promotor:

Prof. dr. Devaraj van der Meer

de co-promotor:

Prof. dr. rer. nat. Detlef Lohse

en de assistent-promotor:

Dr. ir. Jacco Snoeijer

# Contents

# 1 Introduction

## 1.1 Liquids

Liquid is the state of matter with a fixed volume, but which can still deform continuously under influence of a shear stress. A fluid is called Newtonian, when the relation between the shear stress $\tau$ and the shear rate $\dot{\gamma}$ is linear and passes through the origin. The constant of proportionality is the coefficient of viscosity $\mu$, which is a liquid property that describes the resistance of the fluid to deformation.

A non-Newtonian fluid is a fluid whose flow properties differ in any way from those of Newtonian fluids. Most commonly the viscosity of non-Newtonian fluids is dependent on shear rate or shear rate history. However, there are some non-Newtonian fluids with shear-independent viscosity, that nonetheless exhibit normal stress-differences or other non-Newtonian behavior. Therefore, although the concept of viscosity is commonly used in fluid mechanics to characterize the shear properties of a fluid, it can be inadequate to fully describe non-Newtonian fluids.

### 1.1.1 Shear thinning and shear thickening

Conceptually, non-Newtonian fluids can be very roughly categorized into two groups, the shear thinning and the shear thickening liquids. Shear thinning liquids show a decrease in apparent viscosity with increasing shear rate, whereas shear thickening liquids show the opposite, namely an increase in apparent viscosity with increasing shear rate (see Fig. 1.1). An example of a shear thinning material is paint. When paint

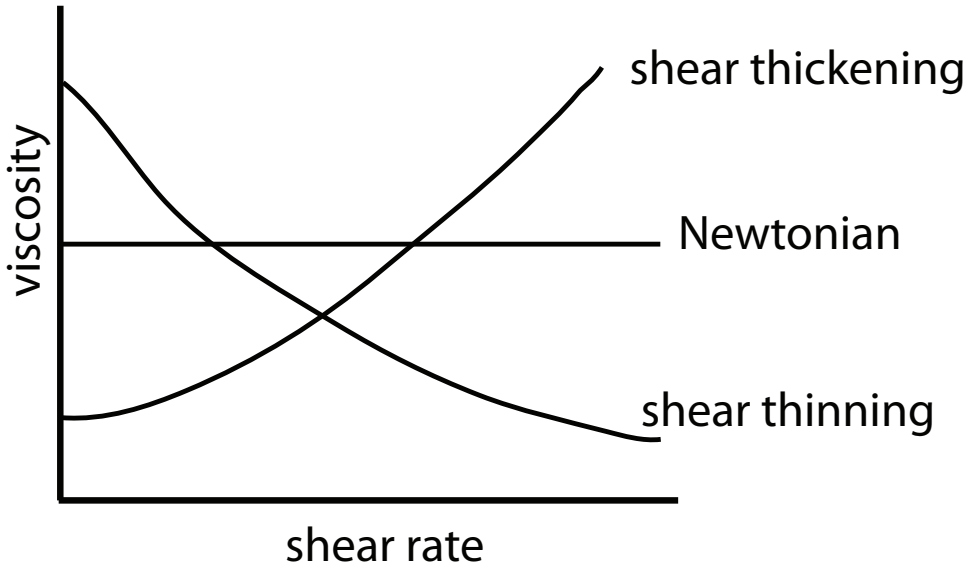


Figure 1.1: Schematic explanation of the difference between Newtonian and non-Newtonian fluids. The horizontal axis shows the shear rate ($s^{-1}$), which provides the amount of shear deformation that is applied per second. The vertical axis shows the liquid's viscosity (Pa·s).

is applied the shear created by the brush or roller will allow them to thin and cover a surface nice and evenly, and it will thicken again afterwards, which avoids drips and runs. Other examples of everyday shear thinning fluids are ketchup, whipped cream and nail polish. Most shear thickening fluids are suspensions, which are the materials that are the center of this thesis.

Non-Newtonian fluids have been studied through several other rheological properties which relate stress and strain rate under many different flow conditions, such as oscillatory shear, or extensional flow which are measured using different devices or rheometers.

### 1.1.2 Suspensions

Suspensions consist of a heterogeneous liquid, containing particles that are larger than 1 $\mu$m. Smaller particles are able to move due to Brownian motion, whereas for larger particles this will be negligible, and external forces will dominate. Suspensions are of great practical interest because they occur frequently in everyday life. These can have desirable properties in a natural or fabricated product (thickening of sauces)

or undesirable ones (unwanted suspension during industrial processes). Some familiar suspensions include those in foods (puddings, sauces), pharmaceutics (cough syrups, laxatives), household products (inks, paints, and waxes), and the environment (sediments, sewage). In spite of their significance, the flow of dense suspensions remains far from understood.

Almost all suspensions are found to be shear thickening under the right circumstances [1]. These circumstances are a combination of liquid and particle properties, as well as the dynamical history of the suspension. The stress-strain curve will in general be not as simple as sketched in Fig. 1.1. Most suspensions will actually show a slight shear thinning for low shear rates which will, at a critical shear rate, abruptly change into a shear thickening regime [1–5]. When increasing the shear rate even further, we may either observe another regime of shear thinning [4], stay at a constant value of viscosity, or witness fracturing of the suspension [6].

The regions in which a suspension, or another particulate system, either flows or jams have been investigated quite intensively, and the variables that control in which state one will be are known as well [7]. The behavior of these materials, however, is not completely understood at this point. Besides this, current models describing shear thickening (and other non-Newtonian phenomena), usually do not take into account the deformation history of the liquid.

Recently, dense suspensions were found to show remarkable behavior in less traditional experiments, which can not be explained by results from rheometry alone, and thus showing the shortcomings in our knowledge of these liquids. The main purpose of this Thesis is to connect this remarkable behavior of dense suspensions to the dynamics of the particle phase in it, which behaves as a granular system that may jam or unjam while the suspension is flowing.

## 1.2 Vibrating liquids

One of the systems alluded to in the previous Section is a thin layer of dense suspension which is vibrated vertically and then perturbed, leading to localized structures. The free surface of a fluid at rest in a container is flat. When this flatness is disturbed, a restoring flow will flatten out the surface again (as long as there is no or negligible yield stress in the fluid). When the container of fluid is vibrated, however, a wide variety of interface phenomena can be observed. The most well-known of these, is that a sinusoidal acceleration produces Faraday waves [8]. As the study and understanding of such spatially extended patterns in out-of-equilibrium systems has matured, attention has turned to localized structures. There are many examples of such localized structures in the Faraday system: pattern defects, solitons, localized jets, and oscillons. These structures usually are period-doubled, which means that

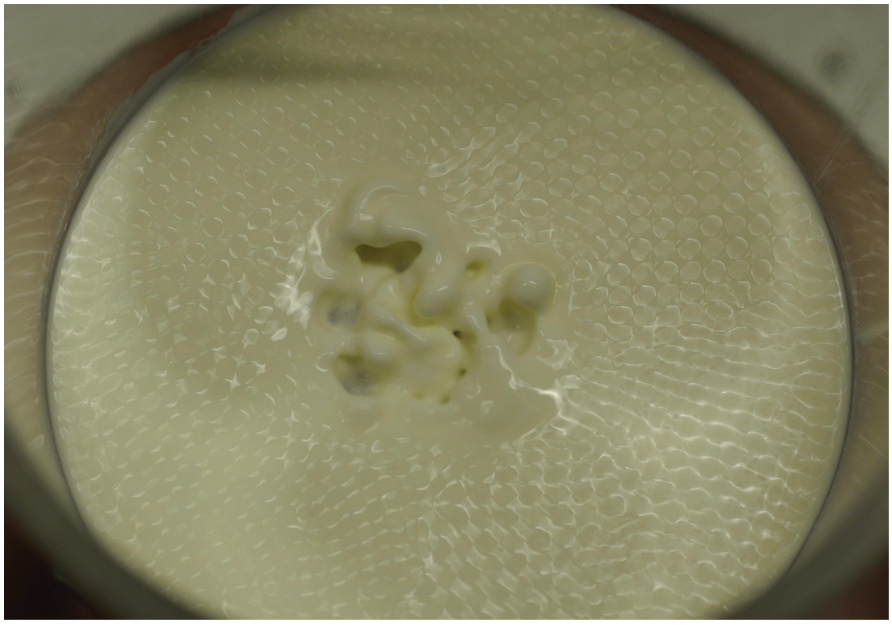

Figure 1.2: Localized structure (fingerlike protrusion), surrounded by Faraday waves in a vibrated cornstarch suspension.

their frequency is half that of the driving. Recently, a new class of localized structures, namely kinks and persistent holes [9, 10] was discovered in the Faraday system with a particulate suspension as the working fluid. These structures need a manual disturbance in the liquid to start, and are markedly different from the other localized structures: They oscillate along with the driving frequency around an unstable state. In Fig. 1.2, an example of such a localized structure in a Faraday system is shown.

The question that arises here is how the vibrations induce these structures in the liquid. Other than that these phenomena are most likely to be connected to the shear-thickening properties of the suspension and a change from a liquid to a more solid-like, jammed state, it is unknown what mechanism causes these shapes.

Research to jamming up to now has focussed on jamming in particulate systems which are quasistatic. In the vibrated system, however, this is of course not the case. This thesis will put the focus on such systems, far from rest. We will have a deeper look in the phenomenology of vibrated suspension, with the objective of unravelling in detail to how the properties of the particles in the suspension influence the behavior of the suspension.

The vibrating system, however, is a complicated system in which driving and resulting movement are in different directions. Besides, the driving is not a constant,

which also adds to the complexity of the problem. Therefore we also turn our attention to a simpler system in which there is movement in a single direction only and a constant driving force, namely an object settling under gravity in a deep bath of liquid.

## 1.3 Impact on and settling in liquids

Upon impact on a liquid surface –depending on both object and liquid– a splash will be created or the liquid will close around the object. The object will subsequently continue to move downward. In the first case however, the object will also create an air void behind itself, which will close due to hydrostatic pressure. When the liquid pinches off in this air void, sometimes a strong jet will be created, shooting out of the liquid bath. When the object travels through the liquid it will at a certain moment find a balance in forces, usually consisting of a driving versus a drag force, and will therefore reach a terminal velocity. When an object falls vertically, driving will be gravity, and the terminal velocity will be kept until a new force comes into play, most likely a full stop on the bottom of the liquid bath.

In some fluids, the object's velocity is less straightforward, as forces that the liquid project on the object are not constant [11–13], and thus lead to a velocity which is not constant. We will perform this same experiment in a deep bath of various suspensions, where we will show some very unexpected settling behavior. A complex rheology and jamming will be shown to at least partly explain this behavior, which, however, will turn out to be very specific to only one kind of suspension, namely a cornstarch suspension. The main question here is whether this system will give us an insight into how an external force can lead to (local) changes in the suspension, leading to the phenomena we observe.

## 1.4 Granulates

The term liquid bath that we used above, can actually be interpreted in a very broad sense, as a granular system can also behave as a liquid, under the right circumstances. Granular materials consist of discrete macroscopic particles which interact mainly through contact forces. In large quantities they can behave like a solid, a liquid, or a gas but often behave differently from what would be expected of these phases [14]. A few every day examples are sand, pills and grains, but also the flow of icebergs in the oceans and cars on the road can be seen as granular 'materials'.

When in a very dilute state, a granular bed can behave remarkably similar to a liquid bath; when an object is thrown in either of those two systems, a splash is formed at impact and after a short time a jet shoots out of the bath. The physics

Figure 1.3: Examples of a granular solid, liquid, and gas.

behind this granular jet has been studied extensively since its discovery [15–31], and in this Thesis, the effect of the proximity of the container walls will be investigated.

Such a dilute granular bed is actually quite similar to a suspension, also consisting of particles with a surrounding fluid, in this experiment air, and thus there are likely to be parallels with the (jamming) behavior of suspensions.

## 1.5 Guide through the thesis

Through our experiments we aim at obtaining a better understanding of suspensions. In our settling experiment we take a deep bath of suspension and let different objects impact onto and settle inside the suspension. We observe several unexpected phenomena during the settling of the objects, which are discussed and, where possible, explained in chapters 2 and 3. In chapter 4 we will have a look in the more complex system of a vertically vibrated layer of suspension. For various suspensions and shaking parameters, we see a wide variety of phenomena beyond those reported in earlier works [9, 10, 32]. Chapter 5 focuses more specifically on the dynamics of holes in various vibrated liquid systems. In chapter 6, we will return to the impact/settling experiment, but now in a very loose, granular medium. Where we observed no jets for dense suspensions, we do see a granular jet in this case and describe its characteristics. In addition we have a look at the trajectory of the impacting sphere for different experimental parameters. In chapter 7 we will draw conclusions based upon the work described in this thesis.

## References

[1] H. Barnes, "Shear-thickening (dilatancy) in suspensions of nonaggregating solid particles dispersed in newtonian liquids", J. Rheol **33**, 329 (1989).

[2] A. Fall, N. Huang, F. Bertrand, G. Ovarlez, and D. Bonn, "Shear thickening of cornstarch suspensions as a reentrant jamming transition", Phys. Rev. Lett. **100**, 018301 (2008).

[3] E. Brown and H. Jaeger, "Dynamic jamming point for shear thickening suspensions", Phys. Rev. Lett. **103**, 086001 (2009).

[4] E. Brown, N. Forman, C. Orellana, H. Zhang, B. Maynor, D. Betts, J.M.DeSimone, and H. Jaeger, "Generality of shear thickening in suspensions", Nat. Mater. **9**, 220 (2010).

[5] C. Bonnoit, T. Darnige, E. Clement, and A. Lindner, "Inclined plane rheometry of a dense granular suspension", J. Rheol. **54**, 65 (2010).

[6] E. B. White, M. Chellamuthu, and J. Rothstein, "Extensional rheology of a shear-thickening cornstarch and water suspension", Rheol. Acta **49**, 119–129 (2010).

[7] A. Liu and S. Nagel, "Jamming is not just cool anymore", Nature **396**, 21 (1998).

[8] M. Faraday, "On a peculiar class of acoustical figures; and on certain forms assumed by groups of particles upon vibrating elastic surfaces", Philosophical Transactions of the Royal Society of London **121**, 299–340 (1831).

[9] F. Merkt, R. Deegan, D. Goldman, E. Rericha, and H. Swinney, "Persistent holes in a fluid", Phys. Rev. Lett. **92**, 184501 (2004).

[10] H. Ebata, S. Tatsumi, and M. Sano, "Expanding holes driven by convectionlike flow in vibrated dense suspensions", Phys. Rev. E **79**, 066308 (2009).

[11] N. Abaid, D. Adalsteinsson, A. Agyapong, and R. McLaughlin, "An internal splash: Levitation of falling spheres in stratified fluids", Phys. Fluids **16**, 1567 (2004).

[12] B. Akers and A. Belmonte, "Impact dynamics of a solid sphere falling into a viscoelastic micellar fluid", J. Non-Newtonian Fluid Mech. **135**, 97 (2006).

[13] M. Arigo and G. McKinley, "The effects of viscoelasticity on the transient motion of a sphere in a shear-thinning fluid", J. Rheol. **41**, 103 (1997).

[14] H. Jaeger, S. Nagel, and R. Behringer, “Granular solids, liquids, and gases”, Rev. mod. Phys. **68**, 1259–1273 (1996).

[15] S. Thoroddsen and A. Shen, “Granular jets”, Phys. Fluids **13**, 4 (2001).

[16] D.Lohse, R. Bergmann, R. Mikkelsen, C. Zeilstra, D. van der Meer, M. Versluis, K. van der Weele, M. van der Hoef, and H. Kuipers, “Impact on soft sand: Void collapse and jet formation”, Phys. Rev. Lett. **93**, 198003 (2004).

[17] J.R.Royer, E. Corwin, A. Flior, M.-L. Cordero, M. Rivers, P. Eng, and H. Jaeger, “Formation of granular jets observed by high-speed x-ray radiography”, Nature Phys. **1**, 164–167 (2005).

[18] J. Royer, E. Corwin, P. Eng, and H. Jaeger, “Gas-mediated impact dynamics in fine-grained granular materials”, Phys. Rev. Lett. **99**, 038003 (2007).

[19] J. Royer, E. Corwin, B. Conyers, A. Flior, M. Rivers, P. Eng, and H. Jaeger, “Birth and growth of a granular jet”, Phys. Rev. E **78**, 011305 (2008).

[20] G. Caballero, R. Bergmann, D. van der Meer, A. Prosperetti, and D. Lohse, “Role of air in granular jet formation”, Phys. Rev. Lett. **99**, 018001 (2007).

[21] J. Marston, J. Seville, Y.-V. Cheun, A. Ingram, S. Decent, and M. Simmons, “Effect of packing fraction on granular jetting from solid sphere entry into aerated and fluidized beds”, Phys. Fluids **20**, 023301 (2008).

[22] J. S. Uehara, M. A. Ambroso, R. P. Ojha, and D. J. Durian, “Low-speed impact craters in loose granular media”, Phys. Rev. Lett. **90**, 194301 (2003).

[23] M. Pica Ciamarra, A. Lara, A. Lee, D. Goldman, I. Vishik, and H. Swinney, “Dynamics of drag and force distributions for projectile impact in a granular medium”, Phys. Rev. Lett. **92**, 194301 (2004).

[24] D. Lohse, R. Rauhé, R. Bergmann, and D. van der Meer, “Granular physics: Creating a dry variety of quicksand”, Nature **432**, 689–690 (2004).

[25] J. R. de Bruyn and A. Walsh, “Penetration of spheres into loose granular media”, Can. J. Phys. **82**, 439–446 (2004).

[26] M. Hou, Z. Peng, R. Liu, K. Lu, and C. K. Chan, “Dynamics of a projectile penetrating in granular systems”, Phys. Rev. E **72**, 062301 (2005).

[27] L. S. Tsimring and D. Volfson, “Modeling of impact cratering in granular media”, in *Powders and Grains 2005, Proceedings of International Conference*

*on Powders and Grains 2005*, edited by R. García-Rojo, H. J. Herrmann, and S. McNamara, volume **93**, 1215–1218 (London: Taylor & Francis) (2005).

[28] H. Katsuragi and D. J. Durian, "Unified force law for granular impact cratering", Nature Phys. **3**, 420–423 (2007).

[29] E. L. Nelson, H. Katsuragi, P. Mayor, and D. J. Durian, "Projectile interactions in granular impact cratering", Phys. Rev. Lett. **101**, 068001 (2008).

[30] A. Seguin, Y. Bertho, and P. Gondret, "Influence of confinement on granular penetration by impact", Phys. Rev. E. **78**, 010301(R) (2008).

[31] R. Mikkelsen, M. Versluis, G. Bruggert, E. Koene, D. van der Meer, K. van der Weele, and D. Lohse, "Granular eruptions: Void collapse and jet formation", Phys. Fluids **14**, S14 (2002).

[32] H. Ebata and M. Sano, "Self-replicating holes in a vertically vibrated dense suspension", Phys. Rev. Lett. **107**, 088301 (2011).

# 2

# Nonmonotonic settling of a sphere in a cornstarch suspension *

*Cornstarch suspensions exhibit remarkable behavior. In this chapter, we present two unexpected observations for a sphere settling in such a suspension: In the bulk of the liquid the velocity of the sphere oscillates around a terminal value, without damping. Near the bottom the sphere comes to a full stop, but then accelerates again toward a second stop. This stop-go cycle is repeated several times before the object reaches the bottom. We show that common shear thickening or linear viscoelastic models cannot account for the observed phenomena, and propose a minimal jamming model to describe the behavior at the bottom.*

*Published as: Stefan von Kann, Jacco H. Snoeijer, Detlef Lohse, and Devaraj van der Meer, Nonmonotonic settling of a sphere in a cornstarch suspension, Phys. Rev. E. **84**, 060401(R) (2011).

## 2.1 Introduction

Concentrated particulate suspensions consist of a homogeneous fluid containing particles, larger than 1 $\mu$m. They can be found everywhere, and their flow is important in nature, industry, and even health care [1]. In spite of their significance, many aspects of the flow of these dense suspensions remain poorly understood. In order to study these materials, people have used methods inspired by classical rheology, and typically characterized them in terms of a constitutive relation of stress versus shear rate [2–6]. A general result is that, when increasing the shear rate, dense suspensions first tend to become less viscous (shear thinning) and subsequently shear thicken.

Probably the most conspicuous example of a dense suspension is formed by a high concentration of cornstarch in water. Recent rheological experiments in cornstarch have revealed the existence of a mesoscopic length scale [6, 7], a shear thinning regime that terminates in a sudden shear thickening [8], a dynamic jamming point [4], and fracturing [9]. Merkt *et al.* [10] observed in a vertically shaken, thin layer of cornstarch suspension that, among other exotic phenomena, stable oscillating holes can be formed at certain frequencies and amplitudes [10, 11], which were subsequently described using a phenomenological model based on a hysteretic constitutive equation [12]. At present, however, we are still far from a detailed understanding of dense suspensions.

In this chapter we subject a cornstarch suspension to a basic experiment, in which we observe and describe the settling of a spherical object in a deep bath of suspension. This yields two interesting observations. In the bulk, we find that the object velocity is oscillating in addition to going toward a terminal value. Near the bottom we observe a second phenomenon: The object comes to a full stop before the bottom, but then accelerates again, and this stop-go cycle can repeat up to seven times. We will show that both bulk and bottom behavior are conceptually different from that observed in a wide range of other fluids. We propose a jamming model for the stop-go cycles near the bottom that specifically includes the liquid-grain interactions.

## 2.2 Setup

Our experimental setup is shown in Fig. 2.1(a). It consists of a $12 \times 12 \times 30$ cm$^3$ glass container containing a mixture of cornstarch and liquid. For the liquid we use either demineralized water or an aqueous solution of Cesium Chloride with a density of 1.5 g/cm$^3$, matching the density of the cornstarch particles. Experiments actually showed negligible differences between the density-matched and the unmatched liquid, except that for the unmatched liquid the suspension has to be stirred well prior to the experiment to counteract sedimentation. The cornstarch particles [Fig. 2.1(b)] are

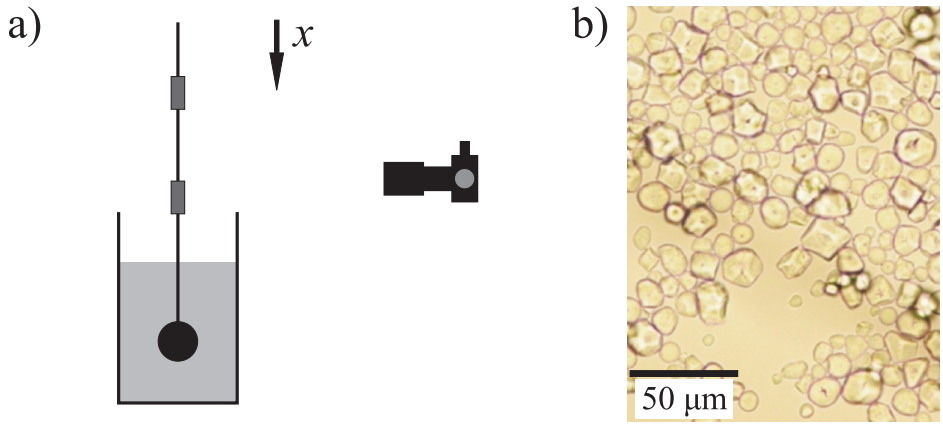


Figure 2.1: (a) Schematic view of the setup, consisting of the container filled with the suspension, the settling sphere with tracers attached, and a high-speed camera. For convenience the positive direction of the vertical coordinate $x$ is chosen downward, with $x = 0$ located at the bottom of the container. (b) Microscopic picture of the cornstarch grains.

irregularly shaped and have a relatively flat size distribution of 5-20 $\mu$m. Although we have varied the packing fraction $\phi$ of the cornstarch, for the data presented here we have fixed it to the high value of $\phi = 0.44$, for which the phenomena of interest are particularly pronounced. All phenomena actually appear when $\phi \geq 0.38$. In a suspension of similarly sized spherical particles, we did not observe the phenomena reported here.

The settling sphere is a $d = 4$ cm diameter pingpong ball, which is filled with bronze beads to vary the buoyancy corrected mass, $\mu = m_{sphere} - \rho_S \pi d^3/6$, from 0 up to 137 g. Here, $\rho_S$ is the density of the suspension. To measure the trajectory of the object inside the suspension, we follow tracers on a thin, rigid metal wire that is attached to the top of the ball (as in Ref. [13]) with a high-speed camera imaging at 5000 frames per second. From the trajectories the velocity and acceleration are determined at each time $t$ using a local quadratic fit around $t$ in a time interval of 12 ms, corresponding to 60 measurement points.

In Fig. 2.2(a) we plot the time evolution of the velocity for three different, buoyancy-corrected masses $\mu$. For the smallest mass (green curve), after some transient directly following the impact (at $t = 0$), there is an approximately exponential decay toward a terminal velocity, as would be found in a Newtonian liquid. When we increase $\mu$, we observe a much more abrupt decrease toward a terminal velocity, but in addition there are oscillations around this terminal value. This is seen most clearly for the highest mass in Fig. 2.2(a) (point 1). Second, instead of stopping at or very close to the bot-

tom -as would happen in a Newtonian liquid- the object actually comes to a sudden, full stop (point 3) at $\sim$10 mm above the bottom for the highest $\mu$ [Fig. 2.2(a), inset] [†]. Surprisingly, the object subsequently reaccelerates (4), only to come to another stop slightly closer to the bottom. This process is repeated several times until the bottom is reached. The observed phenomena are also present when we release the sphere from rest, but to avoid the long acceleration trajectory for small $\mu$ we chose to impact the spheres with non-zero initial velocities to maximize the time in which the bulk effect is observable. To check that the bulk oscillations are not caused by interactions with the side walls, we changed the ratio of container to ball size, qualitatively leading to the same phenomena.

The motion of the settling sphere is described by

$$m\ddot{x} = \mu g + D, \tag{2.1}$$

where $D$ is the drag the sphere experiences inside the suspension and $m = m_{sphere} + m_{added}$ is the total inertial mass, including the added mass for which we will take the standard result $m_{added} = 0.5\rho_S \pi d^3/6$. For a Newtonian fluid with a high dynamic viscosity $\eta$ we have $D = 3\pi\eta d\dot{x}$, leading to an exponential decay toward the terminal velocity $\dot{x}_T = \mu g/(3\pi\eta d)$. When we estimate the effective viscosity of our cornstarch suspension by identifying the (average) plateau velocities in Fig. 2.2(a), we find values between $\eta = 0.87$ and 3.96 Pa·s, which are of the same order as found in Ref. [8], leading to Reynolds numbers on the order of $\mathrm{Re} = 10$. This excludes that we are dealing with path instabilities associated with wake instabilities at $\mathrm{Re} > 100$ in Newtonian fluids (see, e.g., Ref. [14]). In addition, we can also rule out a dominant influence from history forces arising from the build up of the boundary layer for an accelerating object (e.g., the Basset force), as these are expected to be more pronounced for the lighter objects, in contrast to our observations.

We use Eq. (2.1) to determine the drag $D$ on the sphere as a function of its velocity [Fig. 2.2(b)]. From this plot it is clear that a given velocity in general corresponds to more than one value of the drag. Since non-Newtonian fluids with a monotonic stress-strain curve -as, e.g., power-law models for shear thickening and thinning fluids or yield stress fluid models- will lead to a single-valued drag-velocity curve, we necessarily need to turn to a model that includes some history dependence.

[†]Careful examination of the data even reveals a very small negative velocity, corresponding to a tiny bounce upward, which can be interpreted as the elastic response of the jammed region of cornstarch underneath the sphere.

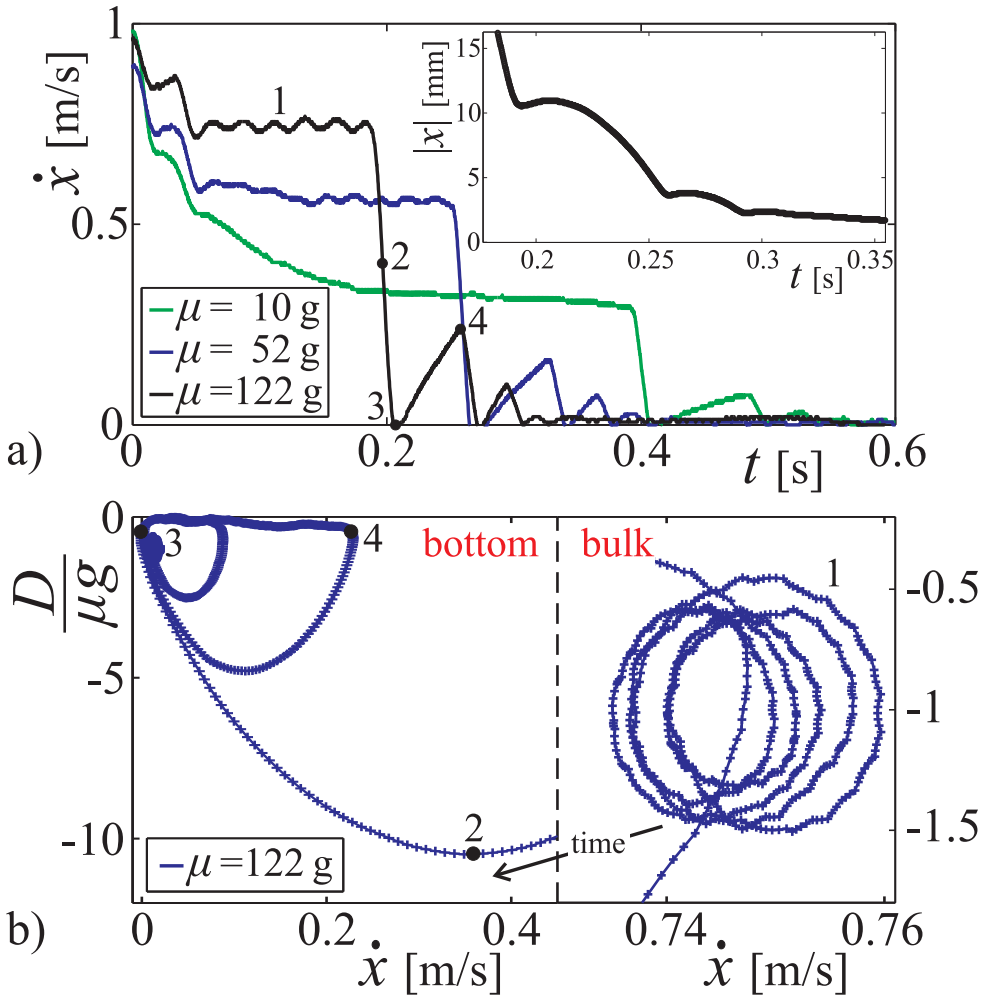


Figure 2.2: (a) Settling velocity $\dot{x}(t)$ of the settling sphere for three different masses $\mu = 10$, 52, and 122 g. The inset shows the last part of the trajectory $|x(t)|$ for $\mu = 122$ g. (b) Drag $D$ vs. velocity $\dot{x}$ of the heaviest sphere in (a) ($\mu = 122$ g). Note the different scales in the right and left half of the plot, which correspond to the bulk oscillations and the stop-go cycles at the bottom, respectively. In the latter, the drag force that causes the ball to come to an abrupt stop is up to ten times as large as gravity, and since it is limited by our fitting procedure, in reality it could be even higher. The numbers correspond to those in (a).

## 2.3 Bulk oscillations

The behavior in the bulk is reminiscent of that of an object sinking in viscoelastic or stratified liquids for which oscillations are known to occur [15–17], albeit with two major experimental differences: First, for viscoelastic fluids there is an elastic rebound (oscillations in the position), whereas for our suspension the object continues to sink, with oscillations in the velocity. Second, in viscoelastic fluids the oscillation is observed to be strongly damped. From a modeling perspective, the damping term in linear viscoelastic fluid models accounts for both the decay of the oscillations and the approach of a terminal velocity [‡]. Clearly, such models fail to describe our observations: The terminal velocity is reached very rapidly after impact, while the oscillations persist without measurable damping.

Another approach is to consider a hysteretic model, such as the one proposed by Deegan [12] to explain why the "persistent holes" in vertically shaken cornstarch [10] do not collapse under hydrostatic pressure. We adapt this model by using a drag force $D$ in Eq. (2.1) which displays two states of damping with different effective viscosities: $D = -B_1\dot{x}$ when $|\dot{x}|$ falls below $\dot{x}_1$ and $D = -B_2\dot{x}$ when $|\dot{x}|$ rises above $\dot{x}_2$. Here, $B_1 < B_2$ and $\dot{x}_1 < \dot{x}_2$, such that there exists a hysteresis loop. Such a model is capable of at least qualitatively describing any of our measurement series, with oscillations occurring when $|B_1\dot{x}| < \mu g < |B_2\dot{x}|$: After impact, the object decelerates in the direction of a terminal velocity $\mu g/B_2$ until it reaches $\dot{x}_1$, after which a jump to the lower drag force branch occurs. Then it starts to accelerate toward a second terminal value $\mu g/B_1$, until $\dot{x}_2$ is reached and the system jumps back to the higher branch ($D = -B_2\dot{x}$). This cycle repeats indefinitely, producing undamped oscillations all the way up to the bottom.

An important drawback of the model, however, is that the experimental findings can only be reproduced by adjusting $\dot{x}_1$ and $\dot{x}_2$ for every $\mu$. This can be appreciated from Fig. 2.3 where we plot the average (terminal) velocity and the equivalent oscillation amplitude [§] of the object in the bulk versus $\mu$. We see that both the terminal velocity, which should be identified with $(\dot{x}_1+\dot{x}_2)/2$ in the model, and the equivalent amplitude ($\approx \dot{x}_2 - \dot{x}_1$) increase with the buoyancy corrected mass. A similar trend was observed in Deegan's rheometer experiments [12]. This implies that the model for the drag force cannot be interpreted as a constitutive model for the cornstarch suspension, therewith greatly diminishing its predictive value.

[‡] We have used the Maxwell model and variations thereof with one spring and up to two dashpots.

[§] The equivalent oscillation amplitude is defined as $\sqrt{2}$ times the standard deviation of the velocity signal, which would be equal to the amplitude for a sinusoidal signal.

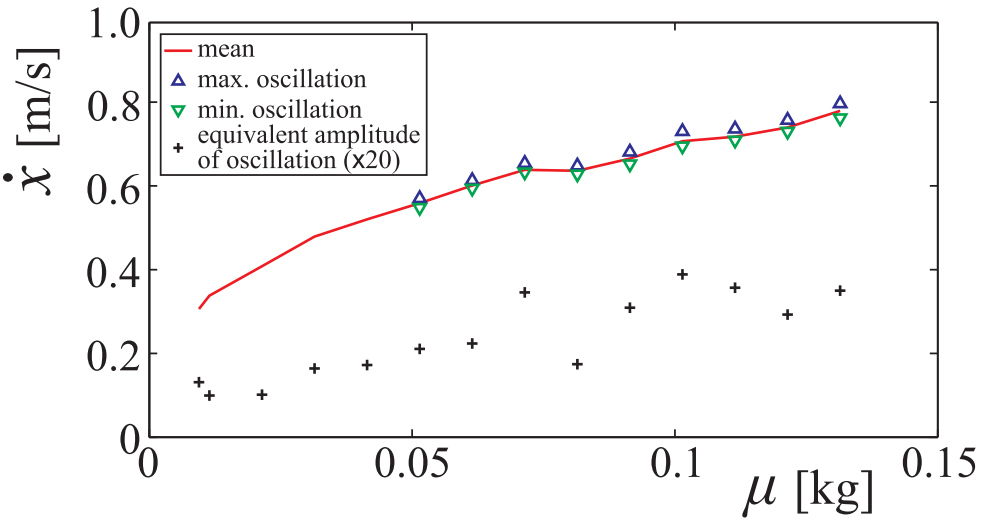


Figure 2.3: Bulk oscillations: Average (terminal) velocity, maximum and minimum velocity (when discernible), and equivalent amplitude of the oscillations, all as a function of the buoyancy-corrected sphere mass $\mu$. Oscillations are only discernible for $\mu > 50$ g. Clearly, the minimum and maximum velocities -which should be identified with $\dot{x}_1$ and $\dot{x}_2$ in the model (see text), respectively- depend on $\mu$.

## 2.4 Stop-go cycles

Near the bottom we find a clear hysteresis between a situation with a sudden, violent deceleration [the large semicircular excursions of the drag force in the left-hand side of Fig. 2.2(b)] and a reacceleration period with a small, Stokes-like drag force $D$ [the almost horizontal parts in the same plot; also see the corresponding $\dot{x}(t)$ curves in Fig. 2.2(a)]. We interpret these stop-go cycles as follows: While the sphere is moving down, the cornstarch below it is slowly being compressed such that at a certain moment a jammed network of particles forms between the object and the container bottom. This jammed layer is responsible for the large force that brings the sphere to a full stop. Stresses build up in the network and therefore also within the interstitial fluid, which triggers a Darcy's flow in the porous medium formed by the cornstarch grains allowing the network to relax through (small) particle rearrangements. This causes the jammed region to unjam and the object will start moving again. Such hardening of a cornstarch suspension has also been reported in Ref. [18], where a ball was pushed toward the bottom, leaving an indent on a clay layer on the bottom. This was attributed to forces being transmitted through a hardened layer beneath the ball.

We model this process by coupling Eq. (2.1) to an equation for an order parameter which indicates whether or not the cornstarch suspension layer between the sphere and the bottom is jammed. We will take this to be the local particle volume fraction $\phi$. When $\phi$ exceeds a critical value $\phi_{cr}$, the layer is jammed and the drag force $D$ is assumed to become infinitely large until the sphere comes to a standstill. This leads to the following modification of Eq. (2.1):

$$\left\{\begin{array}{rcccl} m\ddot{x} & = & \mu g + D & \text{when} & \phi < \phi_{cr} \\ \dot{x} & = & 0 & \text{when} & \phi \geq \phi_{cr} \end{array}\right\}, \tag{2.2}$$

with $D = -B\dot{x}$. The equation for the time rate of change of the packing fraction $\phi$ should contain a term that increases $\phi$ proportional to the compression rate $-\dot{x}/x$ of the -cylindrical- layer of cornstarch below the sphere, which is the process by which the layer jams. Second, there should be a term that decreases $\phi$ through a relaxation process toward its equilibrium, bulk value $\phi_{eq}$. This yields

$$\dot{\phi} = -c\frac{\dot{x}}{x} - \kappa(\phi - \phi_{eq}), \tag{2.3}$$

in which $c$ and $\kappa$ are the proportionality constants of the compression and relaxation processes, respectively. Note that $\kappa^{-1}$ constitutes a time scale for the relaxation dynamics. The critical packing fraction $\phi_{cr}$ is the value at which the cornstarch suspension dynamically jams. It must lie in between the static, sedimented (0.44) and

the maximally compacted (0.57) value [19]. From creating the densest, still flowing cornstarch suspension in our laboratory, we estimate that $\phi_{cr} = 0.46$ at most. As a result, $\phi$ only varies marginally during the process, in agreement with recent research where during jamming of a cornstarch suspension in a Couette cell no density differences where measured within experimental accuracy (0.01) of the Magnetic Resonance Imaging (MRI) device used [8].

In Fig. 2.4(a) we compare the above model to our experiments for three different masses. We find that for a single value for $\kappa = 40$ s$^{-1}$ and $c = 0.025$ ¶, the model provides a reasonably good description of the stop-go cycles for all masses. Moreover, plotting the duration $\Delta t$ of a stop-go cycle and the maximum velocity $\dot{x}_{max}$ reached after the first stop yields the correct trend [Fig. 2.4(b)]. The fact that the second and higher stop-go cycles seem to be predicted too strong and fast by the model may be partly explained from the one dimensionality of the model, which does not fully describe the geometry of the settling sphere. Indeed, the model matches even better to preliminary experiments with a cylinder.

Finally, we connect the relaxation time scale $\kappa^{-1}$ from Eq. (2.3) to Darcy's law which, combined with continuity for an incompressible medium, leads to the porous medium equation $\partial\phi/\partial t = (k/\eta_w)\nabla^2\Delta P$ (see Ref. [20]). Here $\eta_w$ is the dynamic viscosity of water, $\Delta P$ the pressure, and $k$ the permeability, which is estimated using the Kozeny-Carman relation $k = d_g^2(1-\phi)^2/(150\phi^2)$, with $d_g$ the average grain diameter and $\phi \approx \phi_{eq}$. The left-hand side of the porous media equation is equal to the relaxation term in Eq. (2.3), i.e., $\kappa\Delta\phi$. The Laplacian $\nabla^2\Delta P$ can be estimated as the ratio of the pressure generated in the packing due to the buoyancy-corrected weight of the sphere [$\Delta P \approx 4\mu g/(\pi d^2)$] divided by the square of the typical length scale $L$ over which the relaxation flow needs to take place to unjam the suspension. Taking the best-fit value $\kappa = 40$ s$^{-1}$ and $\Delta\phi = \phi_{cr} - \phi_{eq} = 0.02$ yields $L \approx 100 d_g$. This is of the same order as the mesoscopic length scale found by Bonnoit *et al.* [7], dominating the dynamics of highly concentrated cornstarch suspensions.

In conclusion, we presented experiments of objects settling into a bed of a cornstarch suspension, which revealed pronounced non-Newtonian behavior: Instead of reaching a terminal velocity and monotonously stopping at the bottom, the object's velocity oscillates within the bulk and goes through a series of stop-go cycles at the bottom. Common shear thickening and linear viscoelastic models fail to account for the observed phenomena, and we proposed a jamming model to describe the behavior at the bottom, which is in fair agreement with the experiment. A remaining question is to what extent a similar model would be able to explain the oscillations

¶The value $B$ we found near the bottom was fixed at 10 kg/s. The best fit for the parameters $B_1$ and $B_2$ lies at 5 and 15 kg/s if we look at the experiment with the highest mass, thus in the same order of magnitude.

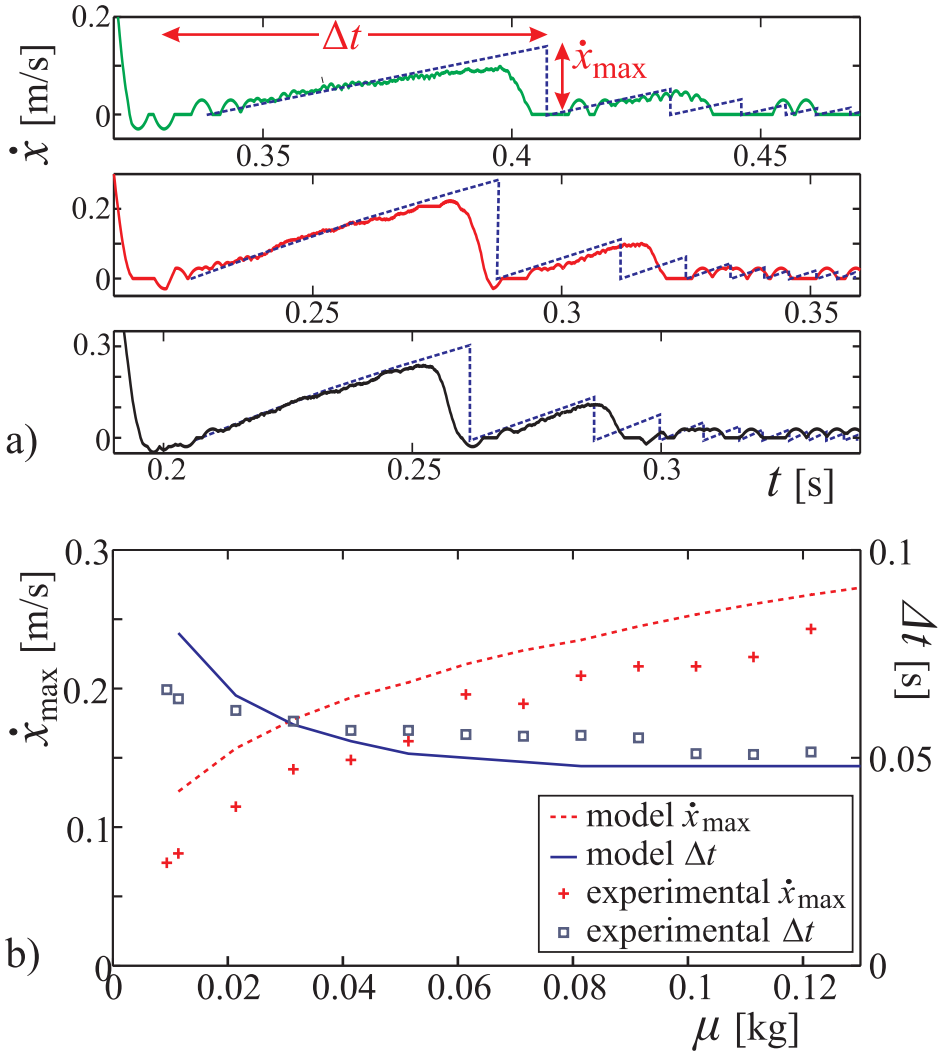


Figure 2.4: (a) Stop-go cycles: Comparison of the experimental velocity (solid lines) and that in the model (dashed blue lines) vs time for three different masses ($\mu = 17$, 77, and 132 g from top to bottom). Note that the time axis has the same scale in all three plots. (b) Stop-go cycles: Comparison of the reacceleration time $\Delta t$ (blue squares) and the maximum velocity $\dot{x}_{max}$ (red crosses) reached after the first stop as a function of the buoyancy corrected mass $\mu$, for both the experiment (symbols) and model (lines).

in the bulk. One could imagine that during the downward motion a layer of (nearly) jammed cornstarch forms around the sphere, as also proposed recently in Ref. [18], which somewhat increases drag and slows it down. This lower velocity in turn would allow the relaxation process to dissolve part of the jammed layer and the object would start to accelerate again. These competing effects would thus induce the oscillatory motion observed in the bulk. Clearly, more research is necessary to quantitatively substantiate such a mechanism.

## References

[1] N. Wagner and J. Brady, "Shear thickening in colloidal dispersions", Phys. Today **62**, 27 (2009).

[2] H. Barnes, "Shear-thickening (dilatancy) in suspensions of nonaggregating solid particles dispersed in newtonian liquids", J. Rheol **33**, 329 (1989).

[3] A. Fall, N. Huang, F. Bertrand, G. Ovarlez, and D. Bonn, "Shear thickening of cornstarch suspensions as a reentrant jamming transition", Phys. Rev. Lett. **100**, 018301 (2008).

[4] E. Brown and H. Jaeger, "Dynamic jamming point for shear thickening suspensions", Phys. Rev. Lett. **103**, 086001 (2009).

[5] E. Brown, N. Forman, C. Orellana, H. Zhang, B. Maynor, D. Betts, J.M.DeSimone, and H. Jaeger, "Generality of shear thickening in suspensions", Nat. Mater. **9**, 220 (2010).

[6] C. Bonnoit, T. Darnige, E. Clement, and A. Lindner, "Inclined plane rheometry of a dense granular suspension", J. Rheol. **54**, 65 (2010).

[7] C. Bonnoit, J. Lanuza, A. Lindner, and E. Clement, "Mesoscopic length scale controls the rheology of dense suspensions", Phys. Rev. Lett. **105**, 108302 (2010).

[8] A. Fall, F. Bertrand, G. Ovarlez, and D. Bonn, "Shear thickening of cornstarch suspensions", .

[9] E. B. White, M. Chellamuthu, and J. Rothstein, "Extensional rheology of a shear-thickening cornstarch and water suspension", Rheol. Acta **49**, 119–129 (2010).

[10] F. Merkt, R. Deegan, D. Goldman, E. Rericha, and H. Swinney, "Persistent holes in a fluid", Phys. Rev. Lett. **92**, 184501 (2004).

[11] H. Ebata, S. Tatsumi, and M. Sano, "Expanding holes driven by convectionlike flow in vibrated dense suspensions", Phys. Rev. E **79**, 066308 (2009).

[12] R. Deegan, "Stress hysteresis as the cause of persistent holes in particulate suspensions", Phys. Rev. E **81**, 036319 (2010).

[13] D. Lohse, R. Rauhé, R. Bergmann, and D. van der Meer, "Granular physics: Creating a dry variety of quicksand", Nature **432**, 689–690 (2004).

[14] N. Mordant and J.-F. Pinton, "Velocity measurement of a settling sphere", Eur. Phys. J. B **18**, 343 (2000).

[15] B. Akers and A. Belmonte, "Impact dynamics of a solid sphere falling into a viscoelastic micellar fluid", J. Non-Newtonian Fluid Mech. **135**, 97 (2006).

[16] M. Arigo and G. McKinley, "The effects of viscoelasticity on the transient motion of a sphere in a shear-thinning fluid", J. Rheol. **41**, 103 (1997).

[17] N. Abaid, D. Adalsteinsson, A. Agyapong, and R. McLaughlin, "An internal splash: Levitation of falling spheres in stratified fluids", Phys. Fluids **16**, 1567 (2004).

[18] B. Liu, M. Shelley, and J. Zhang, "Focused force transmission through an aqueous suspension of granules", Phys. Rev. Lett. **105**, 188301 (2010).

[19] J. Willett, "Packing characteristics of starch granules", Cereal Chem. **78**, 64 (2001).

[20] D.-V. Anghel, M. Strauss, S. McNamara, E. Flekkøy, and K. Måløy, "Erratum: Grains and gas flow: Molecular dynamics with hydrodynamic interactions [phys. rev. e 61, 4054 (2000)]", Phys. Rev. E **74**, 029906 (2006).

# 3

# Velocity oscillations and stop-go-cycles: The trajectory of an object settling in a cornstarch suspension *

*We present results for objects settling in a cornstarch suspension. Two surprising phenomena can be found in concentrated suspensions. First, the settling object does not attain a terminal velocity but exhibits oscillations around a terminal velocity when traveling through the bulk of the liquid. Second, close to the bottom, the object comes to a full stop, but then reaccelerates, before coming to another stop. This cycle can be repeated up to 6 or 7 times before the object reaches the bottom to come to a final stop. For the bulk, we show that shear-thickening models are insufficient to account for the observed oscillations, and that the history of the suspension needs to be taken into account. A hysteretic model, that goes beyond the traditional viscoelastic ones, describes the experiments quite well, but still misses some details. The behavior at the bottom can be modeled with a minimal jamming model. This Chapter provides a more extensive presentation and discussion of the phenomena that have been introduced in the previous Chapter.*

*Submitted as: Stefan von Kann, Jacco H. Snoeijer, and Devaraj van der Meer, Velocity oscillations and stop-go-cycles: The trajectory of an object settling in a cornstarch suspension, to Phys. Rev. E.

## 3.1 Introduction

A suspension is a heterogeneous fluid that contains dispersed solid particles which are large enough to sediment over time when undisturbed. They are literally found all around us and the flow of dense suspensions is important in nature (mud slides), industry (paint), and even health care (blood flow) [1]. In spite of their significance, the flow of these dense suspensions remains far from understood. In previous studies, people have used methods inspired by classical rheology, and typically characterized these materials in terms of a constitutive relation of stress versus shear rate [2–7]. A general result is that, when increasing the shear rate, dense suspensions first tend to become less viscous (shear thinning) and subsequently shear thicken.

Probably the most conspicuous example of a dense suspension is formed by a high concentration of cornstarch in water, also known as oobleck or ooze. In earlier work, rheology experiments with cornstarch suspensions have revealed the existence of a mesoscopic length scale [6, 8], a shear thinning regime that terminates in a sudden shear thickening [9], a dynamic jamming point [4], and fracturing [10]. In an experiment that goes beyond the classical rheological ones, Merkt *et al.* [11] observed that stable oscillating holes can be formed in a thin layer of cornstarch suspension, when shaken vertically at certain frequencies and amplitudes [11]. These holes were subsequently described using a phenomenological model based on a hysteretic constitutive equation [12]. In other dense suspensions, Ebata *et al.* found growing and splitting holes [13, 14], where the first are contributed to a convection-like flow and the latter are still not understood. Another set of remarkable observations were made for settling objects. These displayed non-monotonic settling [15] and jamming between the object and container bottom was found [15, 16]. At present we are thus still far from a detailed understanding of dense suspensions, and why different suspensions behave differently.

In this work we subject a cornstarch suspension to a basic experiment, in which we observe and describe the settling of objects in a deep bath of suspension. The settling dynamics exhibits two remarkable features that are not observed in other types of liquids, but also not in other dense suspensions. In the bulk, we find that the object velocity is oscillating in addition to going towards a terminal value. Near the bottom we observe a second phenomenon: The object comes to a full stop before the bottom, but then accelerates again, and this stop-go cycle can repeat up to seven times. Although non-monotonic settling has been observed in various other systems, like stratified [17] and (visco)elastic [18, 19] liquids, we will show that both bulk and bottom behavior in cornstarch are fundamentally different. We study a wide range of experimental parameters and suspensions to get a detailed insight in these phenomena, discuss several candidates for the (phenomenological) modeling of the observed phenomena, and evaluate their appropriateness.

This chapter is organized as follows. In Section 3.2 we discuss the experimental setup and some data analysis tools. Subsequently, the main experimental observations are presented in Section 3.3, where the influence of various parameters such as the concentration of the cornstarch suspension, the object mass, the object shape and the container size are discussed. Section 3.4 focusses on the bulk oscillations by presenting its particular experimental characteristics and by subsequently discussing the validity of several modeling approaches. The stop-go cycles at the bottom obtain a similar treatment in Section 3.5, a large part of which is devoted to the comparison of a jamming model and the experiments, expanding the material presented in [15]. Finally, in Section 3.6 we briefly discuss the settling dynamics in other particulate suspensions and Section 3.7 concludes the chapter.

## 3.2 Experimental setup

The experimental setup is shown in Fig. 3.1(a). Objects were dropped into either a vertical perspex container of size 12x12x30 $cm^3$ or a cylindrical glass container with a diameter of 5.0 cm, containing a dense mixture of particles and liquid. For the latter, we use either demineralized water or an aqueous solution of Cesium Chloride (CsCl) with a density of $\sim$1600 $kg/m^3$, which matches the density of the cornstarch particles. Experimental results actually showed negligible differences between the density matched and the unmatched liquid, provided that the latter has to be stirred well prior to the experiment, to counteract sedimentation. The cornstarch particles [Fig. 3.1(b)] are irregularly shaped and have an approximately flat size distribution in the range of 5-20 $\mu$m, i.e., small and large particles are present in approximately equal numbers.

The settling objects that were used in this study are stainless steel balls ($\rho = 8000$ $kg/m^3$), with diameters of 1.6 and 4.0 cm, a 4.0 cm pingpong ball, and a 1.5 cm diameter hollow cylinder with a flat bottom, and a length, longer than the liquid bad depth. The latter two can be filled with bronze beads to vary their mass: For the pingpong ball, the buoyancy corrected mass ($\mu = m_{sphere} - \rho_S V$ of the objects, where $\rho_S$ is the suspension density, and $V$ is the submersed volume) could be varied from 0 to 137 grams and the actual mass $m$ of the cylinder was varied from 40 (empty cylinder) up to 120 grams. For the cylinder, the buoyancy corrected mass is not constant over time: The buoyancy increases when the cylinder penetrates deeper into the cornstarch, such that $\mu$ decreases over time. The results for the cylinder will therefore be given in terms of the actual mass.

To measure the trajectory of the objects inside the opaque suspension, we follow tracers on a thin, rigid metal wire that is attached to the top of the object (as in [20]) with a high speed camera imaging at 5000 frames per second. The mass of the wire

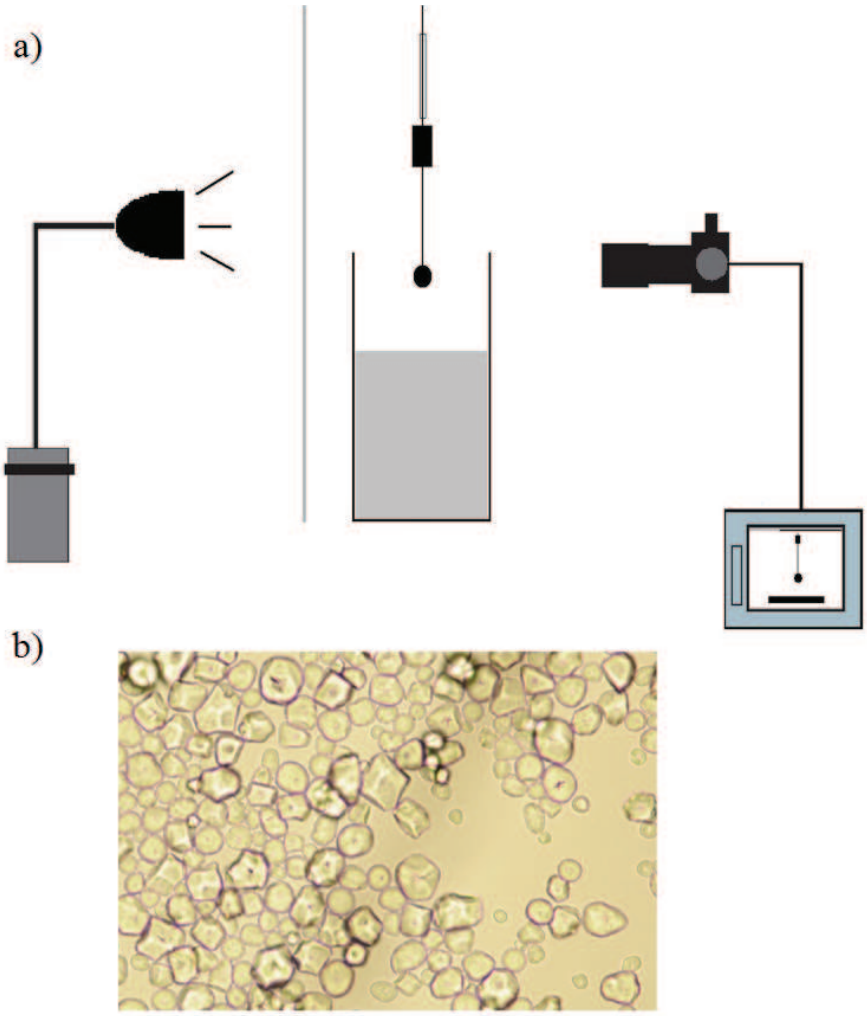


Figure 3.1: (a) Schematic view of the setup, with from left to right: A light source and diffusing plate, the container filled with suspension, above that the object with tracers attached, and a high-speed-camera. (b) Microscopic picture of the cornstarch, used in the experiments.

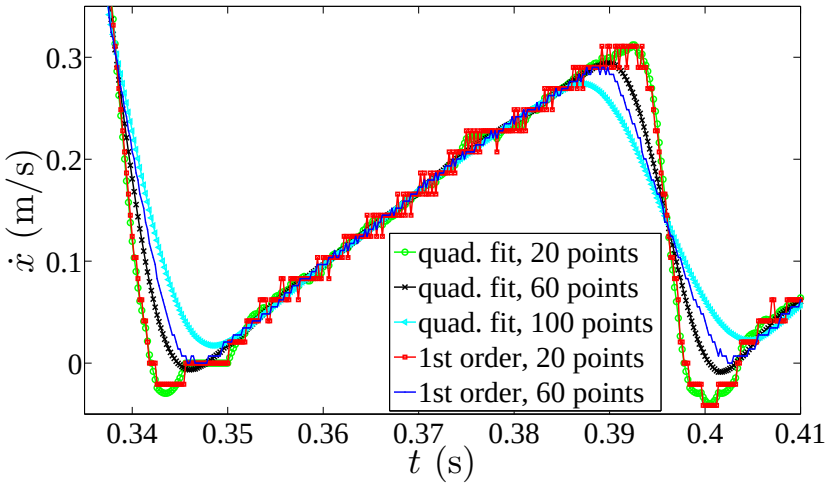


Figure 3.2: The velocity $\dot{x}$ of the settling object versus time $t$, determined by two different methods, namely (i) using a local quadratic fit and (ii) employing a first order difference. The two methods are shown for different time intervals of the fitting procedures, namely 4.0, 12, and 20 ms, to illustrate the trade-off when choosing between higher spatial or temporal resolution.

and the resulting buoyancy of the immersed wire are negligible compared to the larger object to which it is attached. Namely, the mass of the wire is less than 1 gram and the immersed tail volume is smaller than 0.1 times the volume of the smallest object that was used. The velocity and acceleration are determined from the trajectories at each time $t$, using either (i) a local quadratic fit around $t$, or (ii) a direct first and second order difference, both determined over a time interval of 12 ms (corresponding to 60 measurement points). The difference between both methods and the influence of the interval are illustrated in Fig. 3.2, where we show the results of both procedures for the velocity of the object during a particularly sensitive part of the trajectory with abrupt jumps in the velocity. Clearly, when an interval of 4.0 ms (corresponding to 20 measurement points is used, the signal suffers from pixel noise due to the limited spatial resolution of our camera. For an interval of 20 ms (100 points) we observe that a lot of information is lost: The abrupt decreases in velocity flatten out, and also the maximum and minimum velocities are resolved insufficiently. For the above reasons, the time interval was fixed to 12 ms, as it showed the best trade-off when choosing between losing pixel noise due to limits in spatial resolution and losing temporal resolution. In addition, the local quadratic fit leads to a more accurate determination of the acceleration than the method using the second order difference.

## 3.3 Experimental observations

In this Section we will present the main experimental observations. We will start by comparing the settling in a viscous Newtonian liquid to the settling in a cornstarch suspension and show that the behavior of the latter is highly non-Newtonian. This will be followed by a discussion of the effects that various parameters have on the experiment.

### 3.3.1 General observations

In Fig. 3.3 we plot the time-evolution of the velocity of a steel sphere for two different impact experiments: one on glycerin and the other on a cornstarch suspension. The sphere is released and accelerates up to $t = 0$, which is the moment of impact. For glycerin (blue line), a Newtonian liquid, we find the expected behavior for such a liquid: The sphere gradually decelerates and exponentially decays towards a terminal velocity, which is determined by the object and the liquid properties. The experiment ends when the object stops at the container bottom. When looking at the dense cornstarch suspension (black line), we observe some remarkable phenomena: Upon impact, we first see an abrupt decrease towards a lower velocity, which in recent experiments by Waitukaitis *et al.* [21] was explained to be caused by jamming of the suspension upon impact. Subsequently, instead of monotonously approaching a terminal velocity, there appear velocity oscillations around this terminal value: The object alternately goes through periods of acceleration and deceleration. The oscillations show no sign of damping out in the time span that is available to us experimentally. These extraordinary oscillations are quite unlike oscillations that have e.g. been observed in viscoelastic fluids, for which the amplitude rapidly decays. We refer to the oscillations in our experiment as bulk oscillations, to distinguish them from the second phenomenon: Instead of stopping at the bottom, the object actually comes to a sudden, full stop at about 10 mm above the bottom. Surprisingly, instead of just staying there, the object subsequently reaccelerates, only to come to another stop a little closer to the bottom. This process repeats itself several times until the bottom is reached. From here on, we will call these phenomena stop-go-cycles.

As the density matching of such a large bath requires a forbiddingly large amount of salt, we repeated the experiment in an unmatched suspension. Although the cornstarch particles are heavier than the liquid, the settling of particles is negligible for at least several minutes, as we were able to ascertain by performing experiments after different waiting times after stirring, which showed identical behavior. Most of the experiments presented in the current chapter are therefore performed after stirring well, but without density matching.

Before taking a more detailed look at the origin of both effects, we will first

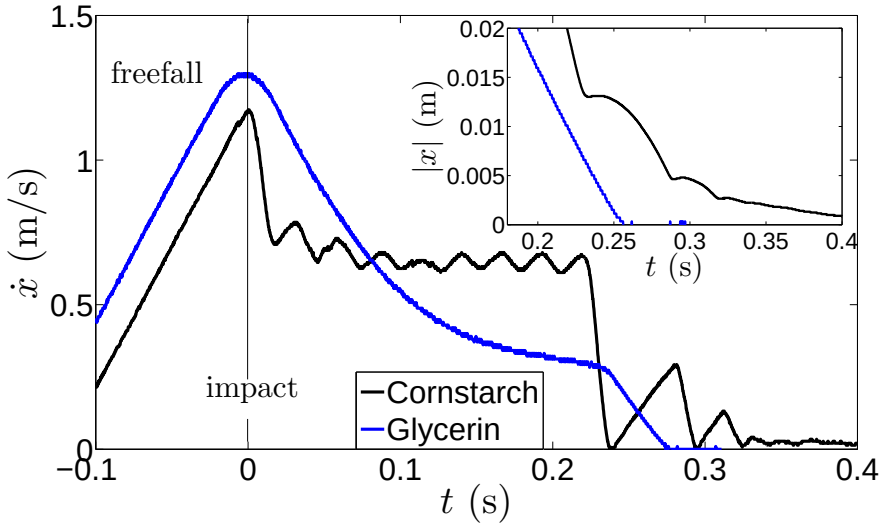


Figure 3.3: The settling velocities $\dot{x}$ of a steel sphere with a diameter of 0.5 cm in glycerine (blue line) and a steel sphere of diameter 1.6 cm in a cornstarch suspension with $\phi = 0.41$ (black line) as a function of time $t$. The inset shows the last part of the actual trajectory, clearly showing the stop-go cycles near the bottom in cornstarch in the position versus time curve.

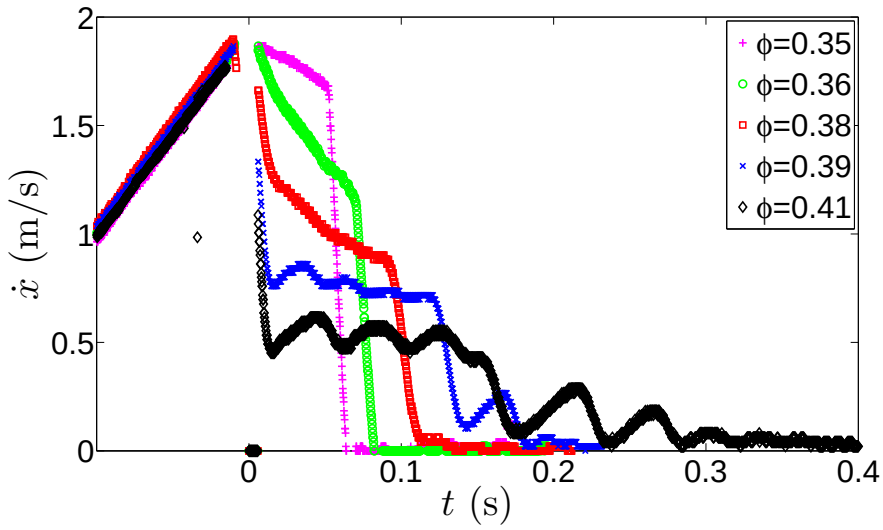


Figure 3.4: Settling velocity $\dot{x}$ of a stainless steel sphere (diameter 1.6 cm) in a cornstarch suspension as a function of time $t$ and for different cornstarch packing fractions $\phi$ varying from 0.35 to 0.41.

discuss how these bulk oscillations and stop-go cycles are influenced by changing the experimental parameters of the liquid bath and the settling object. We only find minor changes when varying the impact velocity and the bed depth.

### 3.3.2 Packing fraction

To determine the influence of the packing fraction, we focus on results of a 1.6 cm stainless steel ball settling in suspensions of different packing fractions ($\phi$), where $\phi$ is the volume occupied by the particles over the total volume of the suspension. The velocity of the ball for different concentrations is plotted in Fig. 3.4 as a function of time. In the plots, $t = 0$ coincides with the moment of impact on the suspension.

First of all we observe that the velocity of the sphere within the suspension has none of the particular characteristics for cornstarch concentrations up to volume fractions of $\phi = 0.38$. The behavior is similar to what is observed for a Newtonian liquid and the only difference is the way the fluid responds upon impact, where we observe a sudden decrease of the velocity. This may well be connected to compaction upon impact as discussed in [21]. While increasing the concentration of cornstarch we see the velocity drop become more pronounced, which is an indication of a larger jammed region created upon impact, consistent with the observations in [21]. Another observation is that the terminal velocity is smaller and appears to be reached at

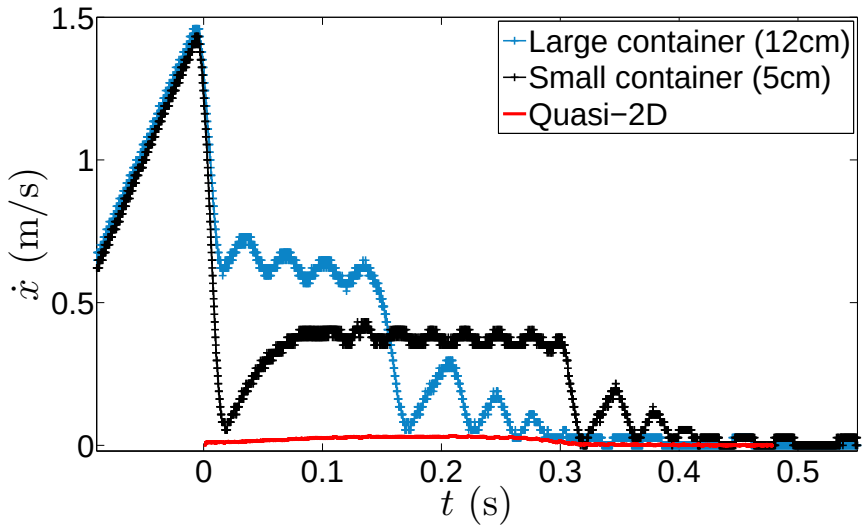


Figure 3.5: The settling velocity $\dot{x}$ versus time $t$ in a square container with a $12 \times 12$ cm$^2$ and a cylindrical container with a diameter of 5.0 cm for a ball of 1.6 cm diameter impacting with a velocity of 1.5 m/s on a cornstarch suspension with a concentration of $\phi = 0.42$. For comparison, also the result of a cylindrical disk settling in a quasi-2D setup is added.

an earlier point in time for higher $\phi$, which can be explained from an overall increase of the apparent (or average) viscosity of the suspension.

When reaching $\phi = 0.39$, we start to observe the non-monotonic settling behavior that was discussed in the previous subsection: After impact we first observe velocity oscillations in the bulk and afterwards, when the sphere approaches the bottom, the stop-go cycles. For increasing cornstarch concentration, we observe a significant increase of the amplitude of the bulk oscillations on the one hand, and of the amplitude, the duration and the number of stop-go cycles on the other. The frequency of the bulk oscillations seems to be less affected by $\phi$.

Clearly, both phenomena are most pronounced for high $\phi$, which is why for the remainder of this study we will will fix our bath concentration at the particularly high value $\phi = 0.44$, unless specified differently.

### 3.3.3 Container size

We performed identical impact experiments with the 1.6 cm steel sphere in two different containers (one with a circular cross section of 5 cm, and the other with a square cross section of 12x12 cm$^2$) containing a single batch of suspension ($\phi = 0.42$) and

compared the results to see whether the proximity of the side walls influences, or maybe even causes, the observed phenomena. The results are shown in Fig. 3.5.

Already immediately after impact the behavior deviates for the different containers: The ball decelerates in both cases, but for the smaller container even comes to an almost full stop. This is likely to be caused by jamming of the suspension in a cone-shaped region below the sphere, as observed in [21]. Whereas this jammed region may move along with the sphere in the larger container, this region may extend all the way up to the wall of the smaller container, such that the sphere is not able to move down in that case.

After this initial velocity drop, both experiments reach a terminal velocity, that is a bit lower for the smaller container. This can be attributed to the proximity of the container wall as well, which will increase the drag in a similar way as it would in a viscous Newtonian liquid. The bulk oscillations are discernible in both containers, but are much less pronounced in the smaller one. This leads to the important conclusion that the bulk oscillations are truly a bulk effect, i.e., they are *weakened* by the proximity of the side walls rather than being reinforced.

By contrast, the stop-go cycles at the bottom are qualitatively the same, only the maximum velocities that are reached during the re-acceleration phase differ slightly. The smaller container again reaches somewhat lower velocities. This may, however, well be connected to the fact that the terminal velocity is smaller for the small container.

In addition to varying the container size, we repeated the experiment in a quasi two-dimensional setup, in a rectangular container with a cross section of $100 \times 5$ mm$^2$ and a depth of 50 mm, using a cylindrical disk with a diameter of 1.5 cm and a thickness of 4 mm as a settling object. In this experiment, we hoped to be able to discern variations in suspension concentration below the settling object. What we observed however, was that all effects actually fully disappeared due to the large friction between the object and the lateral container walls. We added this quasi 2D experiment to Fig. 3.5, where it can be appreciated that the (terminal) settling velocity is only a few centimeters per second.

### 3.3.4 Object mass

Whereas in the previous subsections we discussed the influence of the bath properties on the observed phenomena, we now turn to the settling object itself. First, we consider the effect of the buoyancy corrected mass ($\mu = m_{sphere} - 4/3\pi r^3 \rho_S$ with $\rho_S$ the density of the suspension), by using a hollow pingpong ball, with a radius $r = 2.0$ cm, that can be filled with bronze beads to a mass $m_{sphere}$. This allows us to vary the difference in density between the impactor and the suspension while keeping all other parameters constant. By completely filling the ball we can reach a maximum density

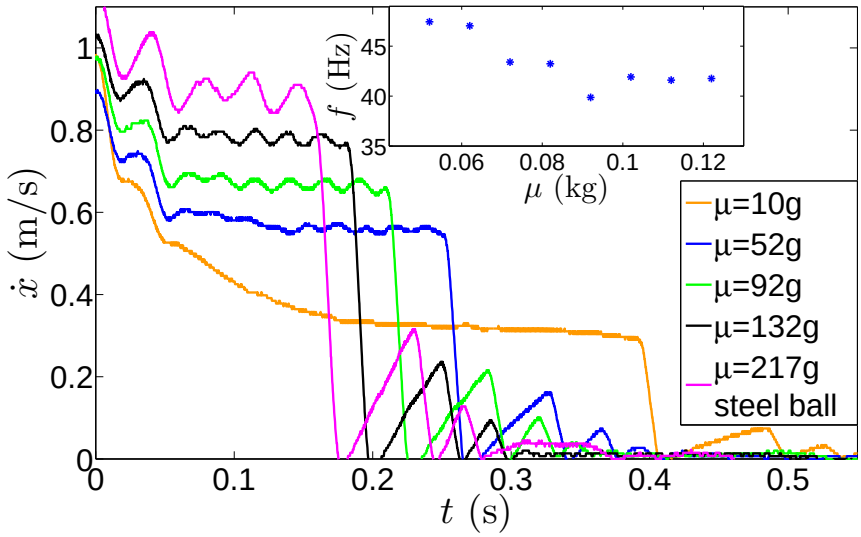


Figure 3.6: Time evolution of the velocity $\dot{x}$ of a hollow pingpong ball filled with different masses settling in a cornstarch suspension with $\phi = 0.44$. The buoyancy corrected mass varies from $\mu = 10$ to $\mu = 132$ gram. Also added is an experiment with a steel sphere of $\mu = 217$ gram, with the same diameter (4.0 cm) as the pingpong ball. The inset shows the frequency of the bulk oscillations for the pingpong ball.

of $5.4 \cdot 10^3$ kg/m$^3$, which is around 3.5 times the suspension density, but lower than the density of the steel sphere used before ($\rho_{steel} \approx 8.0 \cdot 10^3$ kg/m$^3$). The resulting velocity versus time curves for these measurements can be found in Fig. 3.6.

We observe no pronounced bulk oscillations (and even something that looks like an exponential decay) for the experiments with lighter spheres (up to 90 grams, corresponding to $\mu = 47$ g). When we keep increasing the object's mass, the bulk oscillations appear. These start out at very small amplitude, but increase with increasing mass. Another remarkable observation is that the oscillation period is only slightly varying over the entire range of masses where the bulk oscillations are visible: While the buoyancy corrected mass grows over a factor 2, the oscillation frequency only shows a slight decrease of around 20 percent (Fig. 3.6, inset).

In contrast to the bulk oscillations, the stop-go cycles are observed for all masses, even for the smallest buoyancy corrected mass of $\mu = 10$ g which corresponds to a density difference between object and suspension of only 23 %. The magnitude of the stop-go cycles, i.e., both the maximum velocity and the number of cycles, is found to increase with the mass of the object.

For comparison, we also used a massive steel sphere, with $r = 2.0$ cm, and

$\mu = 217$ g. Thus we obtain an even higher density contrast, but at the expense of changing the surface of the object. During settling of this sphere, we observe the same phenomena as for the pingpong ball. The increasing trend we found for the amplitude of the bulk oscillations and the maximum velocity and number of stop-go cycles is continued. The main difference is the fact that we measure a frequency which is a factor 1.5 lower for the bulk oscillations. This may be connected to the different structure of the surface of the object.

### 3.3.5 Object shape

Besides changing the mass of the object, we also varied its shape. We used a hollow cylinder with a diameter of 1.5 cm and a height that exceeds the depth of the cornstarch bath. This changes two aspects: First, the object has a larger contact area with the liquid, and second, we have a flat bottom rather than a curved one. The fact that the cylinder is longer than the depth of the bad allows us to keep it aligned vertically while it is settling towards the bottom. However, this implies that the buoyancy corrected mass changes with the object's position. Finally, due to the fact that the cylinder is hollow, we can vary the mass in the same way as we have done for the pingpong ball, namely by filling it with bronze particles.

All the phenomena observed for the sphere are also present for the settling cylinder (Fig. 3.7): We observe both the bulk oscillations and the stop-go cycles near the bottom. A few differences are clearly visible as well: First, the bulk oscillations are significantly larger in amplitude, which could be either due to the increase in contact surface or to the flatness of the bottom of the cylinder. The frequency is again independent of the mass of the object, however it is approximately a factor two lower than that observed for the sphere. Although only a few oscillations are visible, they appear undamped for the higher masses, but seem to be damped for the lowest mass. This is most likely due to the change in the buoyancy corrected mass, which for this lightest case decreases from 35 to 20 grams between impact and the first stop-go-cycle. Second, we see that the number of consecutive stop-go cycles is larger than for the sphere. We observe up to seven cycles, while for the sphere this was limited to only two or three cycles. In addition, we observe that the first stop appears at a larger distance from the bottom, namely several centimeters as compared to typically one centimeter for the sphere. Finally, the drop in maximum velocity between consecutive stops is smaller for the cylinder.

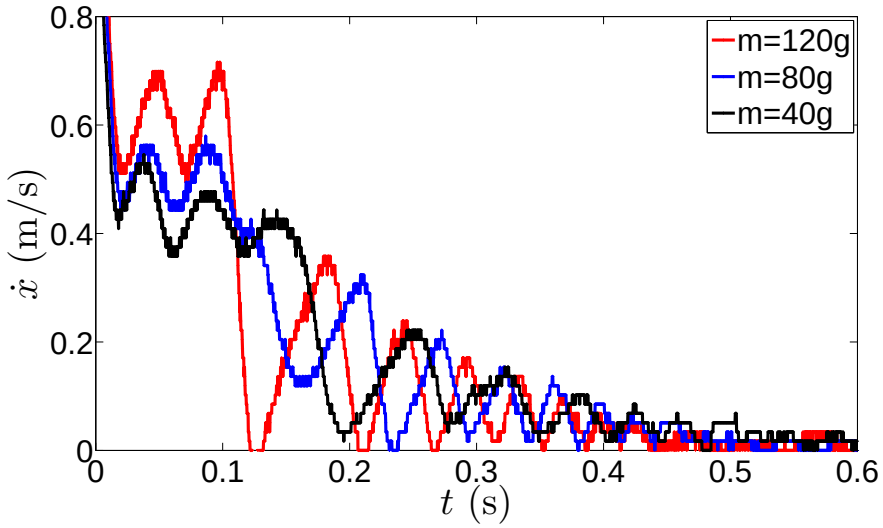


Figure 3.7: Time evolution of the velocity $\dot{x}$ of a settling cylinder in a cornstarch suspension ($\phi = 0.44$) for different cylinder masses $m_{cyl}$, varying from 40 to 120 gram. A buoyancy corrected mass can not be used here since it changes along the trajectory of the cylinder.

## 3.4 Bulk oscillations

When an object is settling in a fluid it can be described by the following equation:

$$m\ddot{x} = \mu g + D(x,\dot{x},t), \tag{3.1}$$

in which $x(t)$ is the trajectory of the object, where $x = 0$ has been chosen to coincide with the bottom of the container and $x$ increases in the downward direction. Furthermore, $g = 9.81$ m/s$^2$ is the acceleration of gravity, $\mu$ is the previously introduced buoyancy corrected mass, and $m = m_{object} + m_{added}$ is the sum of the mass of the object and the added mass. For a sphere we use the traditional result for Newtonian liquids $m_{added} = 0.5\rho_S V_{sphere}$ with $V_{sphere}$ the volume of the sphere and $\rho_S$ the density of the suspension. Finally, $D$ is the drag force which in general is a function of the object's velocity $\dot{x}$ and position $x$. The drag force could even be a functional of $x(t)$ if the history of the objects trajectory is important (which will indeed be argued to be the case). The aim of the next two Sections is to find an appropriate model for the drag force $D$.

In the present Section, we will start with the bulk oscillations. We will attempt to describe this phenomenon using various models, and discuss their appropriateness. As we are using a shear thickening suspension, we start off with traditional shear thickening models, that have a monotonic stress-strain curve. We then consider several viscoelastic models, which are appropriate for the description of the position oscillations that have been observed in viscoelastic liquids. Finally, we investigate a hysteresis model based on a model proposed by Deegan [12] in the context of holes in vibrated cornstarch layers [11].

### 3.4.1 Shear thickening model

As cornstarch is well-known for its shear thickening behavior, the most logical first model to try is a shear thickening model, i.e., a model in which the viscosity increases with increasing shear rate. Or, as an alternative one could think of a model that combines a shear rate region where the viscosity is decreasing with a region where it is increasing to model the shear-thinning to shear-thickening transition that has been observed in rheometer experiments in both cornstarch and other suspensions [2–7]. All these models have in common that the stress increases monotonically with the strain rate, which will lead to a monotonically increasing drag $D$ as a function of the magnitude of the objects settling velocity $\dot{x}$.

We use Eq. (3.1) to determine the drag force from the experimental trajectory, i.e., when we compute $D \equiv m\ddot{x} - \mu g$ for the measured acceleration $\ddot{x}$ and plot the result as a function of the velocity $\dot{x}$ we obtain Fig. 3.8. Clearly, during the bulk oscillations the drag $D$ is *not* a monotonic function of $\dot{x}$. Therefore, we can immediately discard

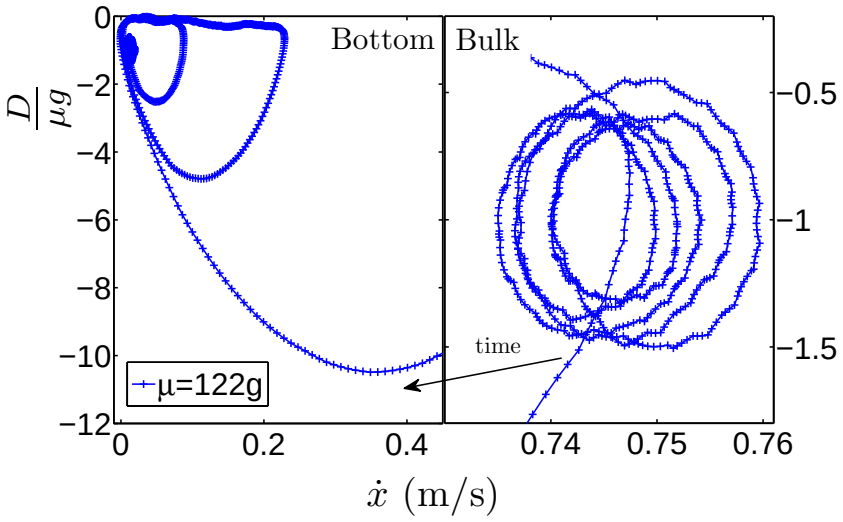


Figure 3.8: The drag $D = m\ddot{x} - \mu g$ on a pingpong ball with buoyancy corrected mass $\mu = 122$ g versus its velocity $\dot{x}$, calculated from the object's trajectory $x(t)$ during a settling experiment in a cornstarch suspension with $\phi = 0.44$.

shear thinning/shear thickening models where the drag (stress) is a monotonically increasing function of the velocity (strain rate). We therefore necessarily need to turn to a model in which the object's history is important.

### 3.4.2 Viscoelastic model

One of the most conspicuous candidates to model the oscillatory behavior is to try a (linear) viscoelastic model, not in the least because oscillations in the position of settling objects have been observed in viscoelastic liquids [18] and modeled by such models [19]. The simplest of such models is the Maxwell fluid, in which the total deformation is decomposed into an elastic term in series with a viscous term. For the elastic part, stress is proportional to strain and the proportionality constant is an elastic modulus; or the viscous part stress is proportional to strain rate with (dynamic) viscosity as a proportionality constant. This translates into the following model for the drag $D$ in Eq. (3.1)

$$-\dot{x} = \frac{\dot{D}}{E} + \frac{D}{\eta}, \tag{3.2}$$

where $E$ corresponds to the elastic part of the drag term and has the dimensions of a spring constant (elastic modulus times a length scale), and $\eta$ corresponds to the viscous part and has the dimensions of viscosity times length. The minus sign reflects

the fact that the direction drag force will generally be opposite to the velocity of the object. The above equation can be integrated to obtain an expression for the drag in terms of $\dot{x}(t)$

$$D = -E \int_{t'=0}^{t} \exp\left[-\frac{E\,(t-t')}{\eta}\right] \dot{x}(t')\,dt'\,. \tag{3.3}$$

As is shown in Section 3.8, the equation we obtain when we insert this expression into Eq. (3.1) can be solved exactly using Laplace transformations, leading to

$$\dot{x}(t) = u_T + e^{-\alpha t}\left[v_0 \cos\omega t + \left(\frac{\mu g}{\omega m} + \frac{E v_0}{2\omega\eta}\right)\sin\omega t\right], \tag{3.4}$$

in which the damping rate $\alpha$, angular frequency $\omega$, the terminal velocity $u_T$, and $v_0$ are given by

$$\begin{aligned} \alpha &= \frac{E}{2\eta}\,; \quad \omega = \sqrt{\omega_0^2 - \alpha^2} = \sqrt{\frac{E}{m} - \left(\frac{E}{2\eta}\right)^2}\,; \\ u_T &= \frac{\mu g}{\eta}\,; \quad \text{and} \quad v_0 = \dot{x}(0) - \frac{\mu g}{\eta}\,. \end{aligned} \tag{3.5}$$

Indeed, this solution displays oscillatory behavior as the object approaches its terminal velocity. However, the terminal velocity is directly coupled to the damping factor $\alpha = E/(2\eta)$, which in turn is coupled to the (minimum) amplitude $\mu g/(\omega m) \lesssim \mu g/(\omega_0 m) = \mu g/\sqrt{mE} \equiv A$ which is obtained by setting $v_0 = 0$ in Eq. (3.4). So when we divide the amplitude over the terminal velocity we obtain

$$\frac{A}{u_T} = \frac{\mu g}{\sqrt{mE}}\frac{\eta}{\mu g} = \tfrac{1}{2}\frac{2\eta/E}{\sqrt{E/m}} = \tfrac{1}{2}\frac{\omega_0}{\alpha} = \pi\frac{\tau}{T}\,, \tag{3.6}$$

in which $\tau = \alpha^{-1}$ is the damping time and $T = 2\pi\omega_0^{-1}$ is the period of the oscillation. This implies that in order to have an amplitude (much) smaller than the terminal velocity, $\tau/T$ needs to be (much) smaller than one, i.e., the damping time should be smaller than the oscillation period. Vice versa, to obtain oscillations that do not damp for several periods, one needs an amplitude which is several times larger than the terminal velocity. Therefore we conclude that it is impossible to describe the bulk oscillations observed in cornstarch within the context of a Maxwell fluid.

It is possible to extend the Maxwell fluid to more complicated linear viscoelastic models, like the extended Maxwell fluid and the modified Kelvin-Voigt solid discussed in Section 3.8, that contain additional dissipative elements in the hope that this would decouple terminal velocity, damping constant, and oscillation amplitude. However, as shown in Section 3.8 all of these models have a coupling similar to the

one expressed in Eq. (3.6) which makes them unsuitable for the description of the observed phenomena. The conclusion is that the bulk oscillations in cornstarch cannot be described by a simple linear viscoelastic model like the ones we considered here. Clearly, one could think of turning to complicated viscoelastic models with multiple length and time scales. However, such an approach would not teach us much about the system.

### 3.4.3 Hysteresis model

We therefore now turn to a model that has been proposed for the behavior of a cornstarch suspension in a different setting, namely a vertically shaken one. As mentioned in the introduction, Merkt *et al.* [11] have observed long-living stable holes in a vertically shaken cornstarch suspension, which they attributed tentatively to the shear thickening properties of cornstarch. In a later paper, Deegan proposed a model to describe this behavior based on a hysteretic rheology [12]. More specifically, he proposed a coexistence of two branches in the stress versus strain rate diagram of the cornstarch suspension, the existence of which was backed up by oscillatory shear measurements in a cone-plate rheometer. This phenomenological model is able to predict the existence of growing holes in a cornstarch suspension.

We now apply this idea for our experiment of an object settling in a deep bed of cornstarch, using Eq. (3.1) with a hysteretic model for the drag force. More specifically

$$D(\dot{x}) = -B(\dot{x})\dot{x}, \tag{3.7}$$

where

$$B(\dot{x}) = \begin{cases} B_1 & \text{when } \dot{x} \text{ falls below } u_1, \\ B_2 & \text{when } \dot{x} \text{ rises above } u_2. \end{cases} \tag{3.8}$$

Here, $u_1$ and $u_2$ (with $u_2 > u_1$) are the turnover velocities of the system and the drag coefficients $B_1$ and $B_2$ (with $B_2 > B_1$) are the slopes of the two branches, namely one corresponding to a low viscosity ($B_1$) and the other to a high one ($B_2$). Between $u_1$ and $u_2$ the system can be in either of the two branches, as illustrated in Fig. 3.9(a).

How this model for $D$ is able to produce oscillations in the context of Eq. (3.1) is illustrated schematically in Fig. 3.9(b). After impact, the object will be in the higher branch with drag coefficient $B_2$ and will decelerate until it reaches the lower boundary $u_1$. There the system will switch to the lower branch and its drag coefficient will decrease to $B_1$. As this results in a drag force smaller than the downwards acceleration of gravity, the object will accelerate again towards the terminal velocity $\dot{x}_1 = \mu g/B_1$, which is the steady state of Eq. (3.1) when the system is in the lower branch, i.e., $D = -B_1\dot{x}$. Before reaching $\dot{x}_1$ however, the object will hit the velocity $u_2$, where the drag coefficient jumps to $B_2$. Now the object will decelerate again towards a

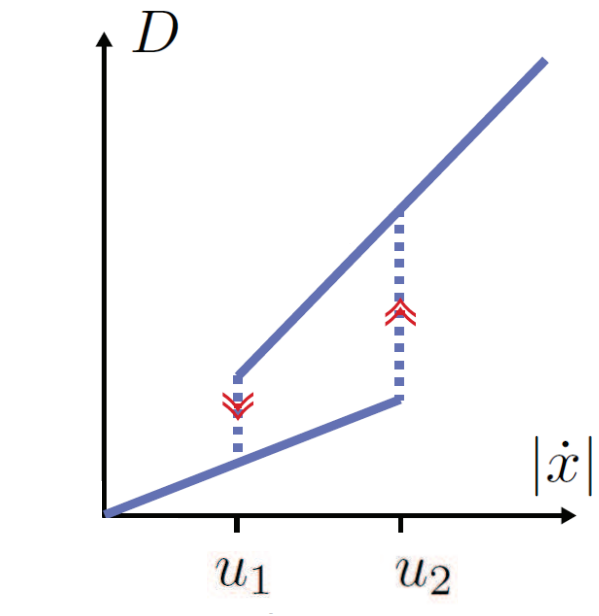


(a)

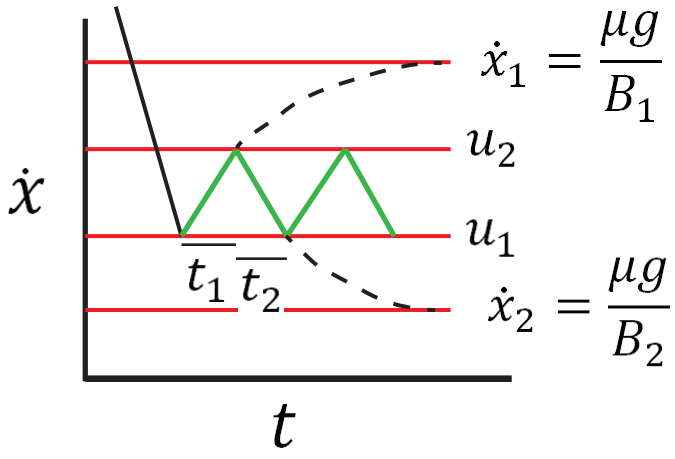


(b)

Figure 3.9: (a) Schematic of the drag force $D$ defined by Eq. (3.7) as a function of the velocity $\dot{x}$, with the hysteresis loop between $\dot{x} = u_1$ and $\dot{x} = u_2$. (b) Schematic of the oscillatory solution of Eq. (3.1) using the drag force of (a): For suitable values of $B_1$, $B_2$, $u_1$, and $u_2$ the system alternately switches from the low to the high branch in the hysteresis loop and back. In these schematics, all quantities are in arbitrary units.

second terminal velocity $\dot{x}_2 = \mu g/B_2$ (corresponding to Eq. (3.1) in the higher branch $D = -B_2\dot{x}$), but before arriving there, $u_1$ will be reached again. This restarts the cycle that will now repeat over and over again.

To relate $B_1$ and $B_2$ to experimental observables, we solve equation 3.1 for $\dot{x}$ in each of the two branches, starting at an arbitrary time $t = t_0$ at one of the boundaries $u_1$ or $u_2$ of the hysteresis loop. This leads to

$$\dot{x} = \dot{x}_i + (u_i - \dot{x}_i)\exp\left[\frac{-\mu B_i}{m}(t - t_0)\right], \tag{3.9}$$

for $i = 1, 2$. Here, $\dot{x}_i \equiv \mu g/B_i$ are the terminal velocities introduced above.

Now we linearize this equation in $t$ between $u_1$ and $u_2$. This leads to the following expression for $B_1$

$$B_1 = \left(\frac{-u_2 + u_1}{\Delta t_1}\frac{m}{\mu} + g\right)\frac{1}{u_1}, \tag{3.10}$$

and similarly for $B_2$ with the indices 1 and 2 interchanged. Here, $\Delta t_1$ and $\Delta t_2$ are the time intervals it takes for the object to accelerate or decelerate from the one switching velocity to the other. By determining $\Delta t_1$, $\Delta t_2$, $u_1$, and $u_2$ from our experiments we can now calculate $B_1$ and $B_2$.

The next step is to compare the model to the experiments. First we assumed that the drag coefficients $B_1$ and $B_2$ are determined by fluid properties, i.e., that they are independent of the object mass or velocity. We thus calculated the drag coefficients for the experiment with the highest mass and applied them to the other masses. Here, we do have to adjust the turnover velocities $u_1$ and $u_2$, to obtain an oscillation between the observed velocity boundaries. The result is shown as the solid lines in Fig. 3.10(a). We apply the model after all impact related effects have disappeared, and clear fluctuations around a terminal velocity are visible. For the four measurements between $\mu = 62$ and $\mu = 132$ gram in Fig. 3.10(a), we see that the model fits nicely for the heaviest balls, and quite well for the lighter balls, from which we conclude that the assumption of constant $B_1$ and $B_2$ is reasonable. This can also be checked by calculating $B_1$ and $B_2$ for every experiment separately, the results of which are shown in Fig. 3.11. We observe that both $B_1$ and $B_2$ only vary very slightly for all masses.

For further comparison, we plot the hysteresis loop in a drag versus velocity plot for both the experiment and the model in Fig. 3.10(b). It is clear that the modeled loop is a very simplified representation of the actual loop, and that, especially for the lower masses the variations in the observed accelerations are considerably smaller than those of the model.

We compared the experiments with a spherical object to those with a cylinder (discussed in Section 3.3.5). The cylinder diameter is 1.5 cm, which is smaller than the ball, and also we now have a flat bottom instead of a round one. Due to the length

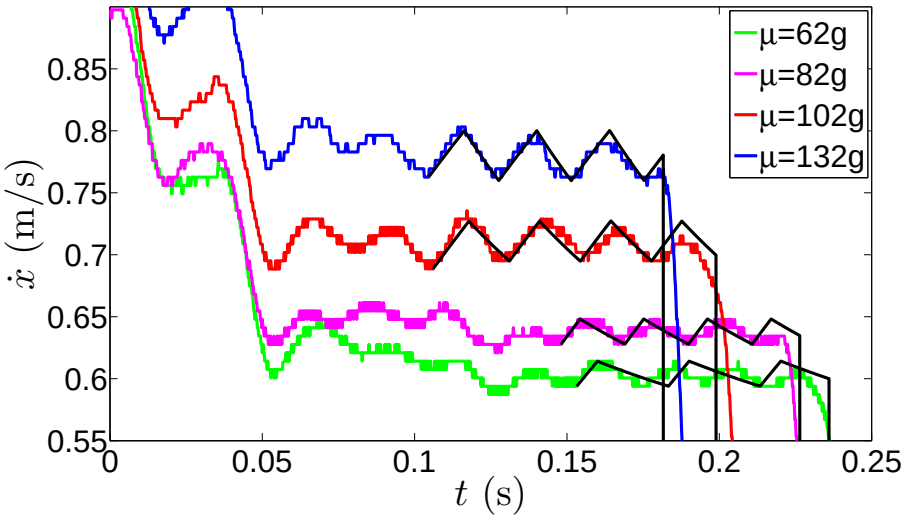


(a)

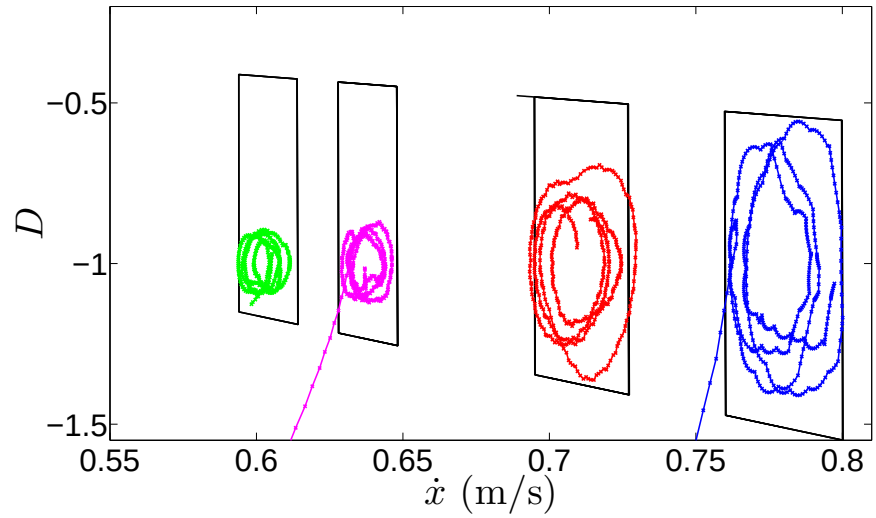


(b)

Figure 3.10: Comparison of the experimental results to the hysteresis model. (a) In the region where bulk oscillations are observed, the velocity of the sphere is plotted versus time for four different buoyancy corrected masses ($\mu$ = 62, 82, 102, and 132 gram) for both the experiment (colored symbols) and the model (black lines), where the values for $B_1$ and $B_2$ have been obtained from the experiment with the highest mass. (b) The corresponding drag $D = m\ddot{x} - \mu g$ versus velocity $\dot{x}$ plots also for both the experiment (colored symbols) and the model (black lines).

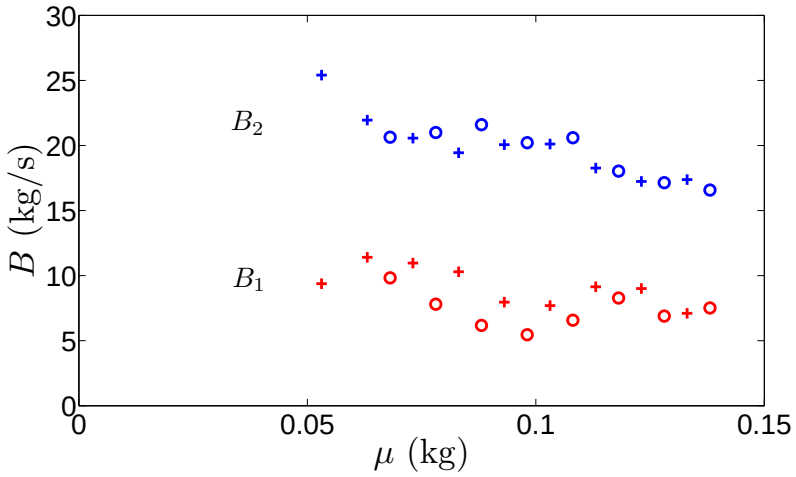


Figure 3.11: The drag coefficients $B_1$ and $B_2$ as a function of buoyancy corrected mass $\mu$, now calculated from the experiment using Eq. (3.10) separately for each value of $\mu$. Below $\mu = 62$ g no bulk oscillations could be discerned. The different symbols correspond to two different series of experiments.

of the cylinder we expect more interaction between the liquid and the object, but we also have to keep in mind that we now have a buoyancy that increases during sedimentation. Again, we calculate $B_1$ and $B_2$ from the measurements with the heaviest mass, where the effect is most pronounced, and adjust $u_1$ and $u_2$ for each mass. The results are shown in Fig. 3.12 where we see that (as expected) the fit is very nice for the highest mass and that there are larger discrepancies for the lower masses. The used values for $B_1$ and $B_2$ for the cylinder are respectively approximately a factor 2 lower and higher compared to the values used for the sphere, 3 and 35 for the cylinder vs. 7 and 18 for the sphere.

Concluding this Section, we found that traditional shear-thinning/shear-thickening models are not able to describe the bulk oscillations due to the presence of history dependence (hysteresis) in the experiments. In addition, we found that simple linear viscoelastic models fail to describe the observed oscillations due to an intrinsic coupling between the terminal velocity and the oscillation amplitude in these models that is inconsistent with the experiments. The best candidate is a description in terms of a hysteretic drag term inspired by the work of Robert Deegan [12]. One could say that the major drawback of the model is that it is entirely phenomenological, i.e., a physical mechanism to relate its parameters to the physics of the system, is still lacking.

The experiments point to a physical mechanism where the origin of the oscil-

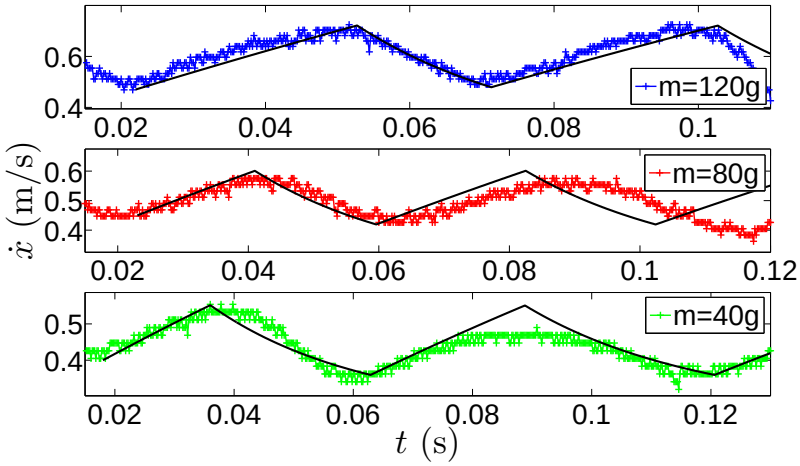


Figure 3.12: Comparison of the experimental results to the hysteresis model for a cylindrical object in the region where bulk oscillations are observed. The velocity of the cylinder is plotted versus time for three different masses ($m_{cyl} = 40$, 80, and 120 gram) for both the experiment (colored symbols) and the model (black lines), where the values for $B_1$ and $B_2$ have been obtained from the experiment with the highest mass.

lations is a modulation on top of the terminal velocity, due to periodically changing properties in the liquid. More specifically, one could imagine a jammed region around the object which grows when it moves fast, through which the drag increases causing the object to decelerate. The object would than obtain a lower velocity which would allow relaxation and shrinking of the jammed layer, i.e., a decrease of the drag and an acceleration of the object. For the bulk oscillations there are many open questions to propose such a model, but for the stop-go cycles at the bottom the formulation of such a model is feasible, as we will show in the next Section.

## 3.5 Stop-go cycles

As was shown in Section 3.3, we always observe stop-go-cycles near the bottom at cornstarch concentrations higher than $\phi = 0.38$. Here, the object suddenly stops one or a few centimeters above the bottom of the container. Then it accelerates again and comes to another abrupt stop a little closer to the bottom. This cycle repeats itself several times.

As explained in [15], we interpret these stop-go cycles as follows: While the object is moving down, the cornstarch below it is slowly being compressed such that at a certain moment a jammed network of particles forms between the object and the container bottom. This jammed layer is responsible for the large force that brings the object to a full stop. Stresses build up in the network and therefore also within the interstitial fluid, which triggers a Darcy's flow in the porous medium formed by the cornstarch grains allowing the network to relax through (small) particle rearrangements. This causes the jammed region to unjam and the object will start moving again. Such hardening of a cornstarch suspension has also been reported in [16], where a ball was pushed towards the bottom, leaving an indent on a clay layer on the bottom. This was attributed to forces being transmitted through a hardened layer beneath the ball.

In Fig. 3.13 we compare the stop-go cycles for the settling pingpong ball (which we previously presented in [15]) with those for the settling cylinder, both for three different values of the buoyancy corrected mass $\mu$. Clearly, for the cylinder there are more stop-go cycles than there are for the pingpong ball. To further quantify the stop-go cycles, we measure the distance from the bottom at which the object stops for the first time ($|x_0|$), Fig. 3.14(a), the maximum velocity it reaches after the first stop ($\dot{x}_{max}$), Fig. 3.14(b), and the time it needs to reach this velocity ($t_{acc}$), Fig. 3.14(c), for both the pingpong ball and the hollow cylinder. Although in general the cylinder has a variable buoyancy-corrected mass during its trajectory, due to the proximity of the bottom we could define a meaningful buoyancy corrected mass here. Namely, we choose the cylinder mass minus the buoyancy the cylinder would experience when it

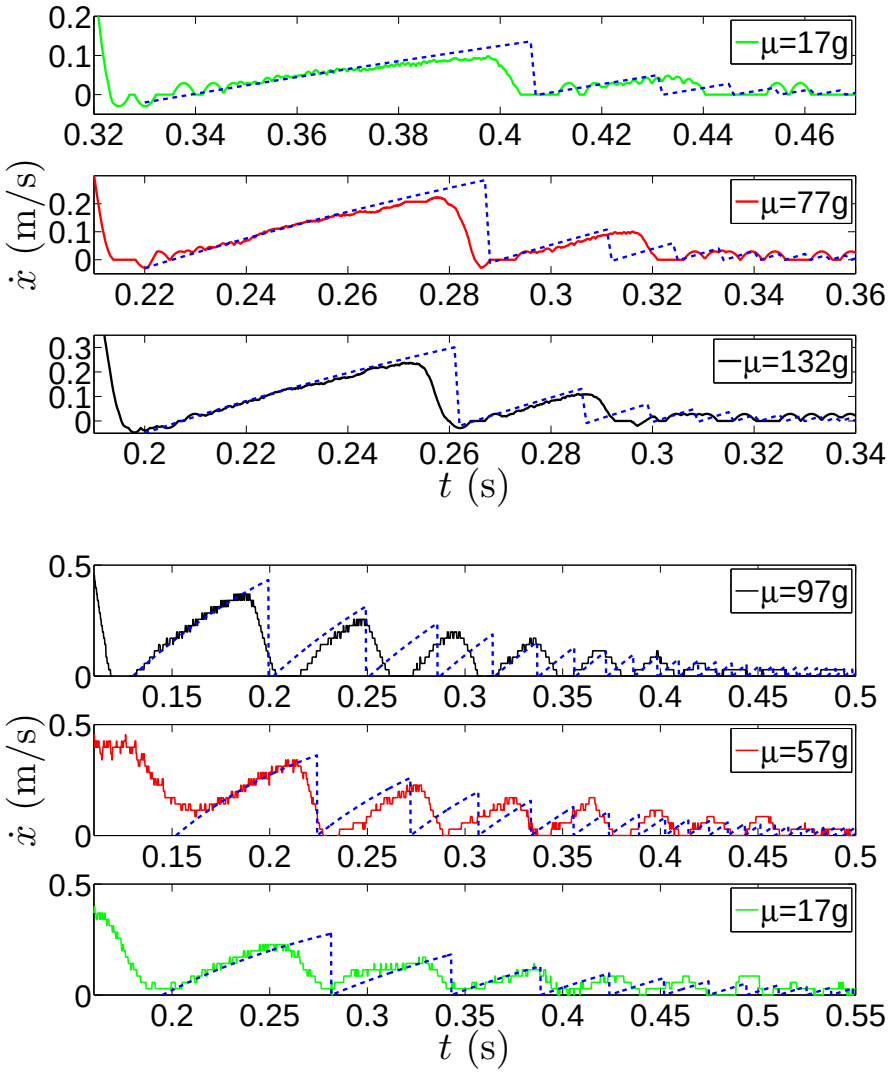


Figure 3.13: Time evolution of the velocity during the stop-go cycles for the settling pingpong ball for three different (buoyancy corrected) masses $\mu = 17$, 77, and 132 g, and for the settling cylinder, also for three different buoyancy corrected masses $\mu = 97$, 57, and 17 g. The noisy lines represent the experimental results and the dashed blue lines correspond to the model of Eq. (3.11).

would be at the bottom.

We see that the cylinder stops several centimeters above the bottom, i.e., several centimeters above the first stop of the pingpong ball. Furthermore, in comparison with the ball it reaches higher velocities after the first jump, but requires approximately the same time to get there. The earlier stop can be explained by a relatively larger jammed region due to the flat bottom of the cylinder, which might also give a more confined region as compared to that below the curved surface of the ball. The fact that the cylinder accelerates to a higher velocity is presumably due to the first stop being at a larger distance from the bottom, such that it takes longer for the material to jam again.

We model this process by coupling the equation of motion Eq. (3.1) to an equation for an order parameter which indicates whether the cornstarch suspension layer between the object and the bottom is jammed or not. For this, we will use the local particle volume fraction $\phi$. More specifically, we assume that when $\phi$ exceeds a critical value $\phi_{cr}$ the layer is jammed and the drag force $D$ is assumed to become infinitely large until the sphere comes to a standstill. This leads to the following modification of the freefall equation:

$$\left\{\begin{array}{rcccl} m\ddot{x} & = & \mu g + D & \text{when} & \phi < \phi_{cr} \\ \dot{x} & = & 0 & \text{when} & \phi \geq \phi_{cr} \end{array}\right\}. \tag{3.11}$$

Due to the comparatively low velocities in this regime compared to those of the bulk-oscillations regime, we can take $D = -B\dot{x}$. Since the cornstarch layer below the object jams through compression, the equation for the time rate of change of the packing fraction $\phi$ should contain a term that increases $\phi$ proportional to the compression rate $-\dot{x}/x$ of this layer. In addition, there should be a term that decreases $\phi$ through a relaxation process towards its equilibrium value $\phi_{eq}$, which is taken to be equal to the value that it has in the quiescent cornstarch suspension. This yields

$$\dot{\phi} = -c\frac{\dot{x}}{x} - \kappa(\phi - \phi_{eq}), \tag{3.12}$$

in which $c$ and $\kappa$ are the proportionality constants of the compression and relaxation processes respectively. Note that $c$ is dimensionless, while $\kappa$ is a relaxation time.

The critical packing fraction $\phi_{cr}$ is the value at which the cornstarch suspension dynamically jams. It must lie in between the static, sedimented (0.44) and the maximally compacted (0.57) value [22]. In our lab we tried to create the densest, still flowing cornstarch suspension from which we estimate that $\phi_{cr} = 0.46$ at most. As a result $\phi$ only varies marginally during the process, in agreement with recent research where during jamming of a cornstarch suspension in a Couette cell no density differences where measured within experimental accuracy (0.01) of the MRI device used [9].

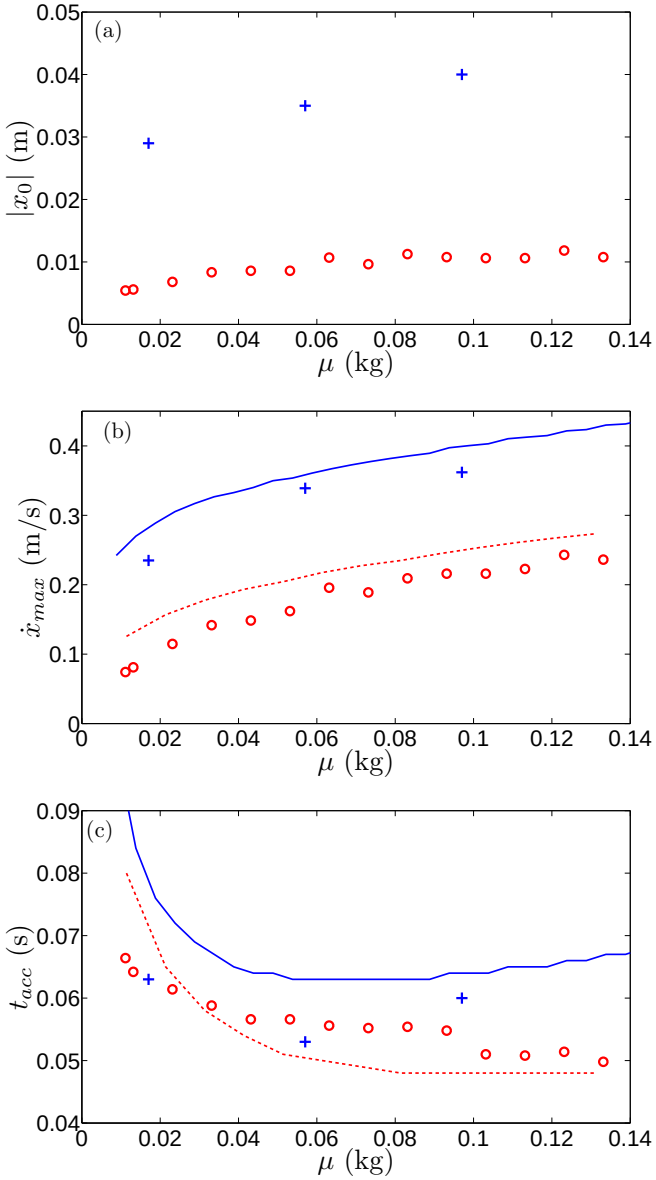


Figure 3.14: Three quantities that characterize the first stop-go cycle as a function of buoyancy-corrected mass for the cylinder (blue crosses) and pingpong ball (red circles): (a) Distance $x_0$ to the bottom at which the first stop takes place. (b) The maximum velocity reached in the relaxation period after the first stop. (c) The time needed to reach the maximum velocity after the first stop. The solid lines in (b) and (c) represent the results obtained with the model of Eq. (3.11).

To obtain the time-evolution of $x(t)$, $\dot{x}(t)$, and $\phi(t)$ this set of equations needs to be solved with the initial conditions the system has reached just after the first stop: $x(0) = -x_0$, the position the object at the first stop (with $x_0 > 0$), $\dot{x}(0) = 0$ and $\phi(0) = \phi_{cr}$. This immediately points to a convenient way of non-dimensionalizing the equations, namely by using $x_0$ and $\sqrt{x_0/g}$ as the appropriate length and time scales. With the non-dimensional variables $\widetilde{x} \equiv x/x_0$, $\widetilde{t} \equiv t/\sqrt{x_0/g}$ and $\delta\widetilde{\varphi} \equiv (\phi(t) - \phi_{eq})/(\phi_{cr} - \phi_{eq})$, the set of equations becomes:

$$\begin{aligned} \ddot{\widetilde{x}} &= \mu/m - \widetilde{B}\dot{\widetilde{x}} \qquad \text{when } \delta\widetilde{\varphi} < 1 \\ \dot{\widetilde{x}} &= 0 \qquad\qquad\qquad \text{when } \delta\widetilde{\varphi} \geq 1 \\ \delta\dot{\widetilde{\varphi}} &= -\widetilde{c}\frac{\dot{\widetilde{x}}}{\widetilde{x}} - \widetilde{\kappa}\delta\widetilde{\varphi}, \end{aligned} \tag{3.13}$$

with initial conditions $\widetilde{x}(0) = -1$, $\dot{\widetilde{x}}(0) = 0$, and $\delta\widetilde{\varphi}(0) = 1$. The dimensionless model parameters are now $\mu/m$, $\widetilde{B} \equiv (B/m)\sqrt{x_0/g}$, $\widetilde{c} = c/(\phi_{cr} - \phi_{eq})$, and $\widetilde{\kappa} = \kappa\sqrt{x_0/g}$, which is the ratio between the gravitational time scale and the relaxation time scale.

What can we say about the parameters in these equations with respect to our experiments? First of all, $\mu/m$ is expected to be of order unity. Second, for most of our experiments the acceleration phase in a cycle appears to be dominated by gravity, such that the second term in Eq. (3.11) is much smaller than the first, implying that $\widetilde{B} \ll 1$. Third, since $x$ and changes in $x$ during a single cycle are of the same order, we expect by neglecting the last term in the last equation for that $\delta\widetilde{\varphi} \sim \widetilde{c}$. Since on the other hand $\delta\widetilde{\varphi} \approx 1$, because the compression is expected to change $\phi$ from its bulk value $\phi_{eq}$ to the critical value $\phi_{cr}$, we expect $\widetilde{c}$ to be of order one.

If we fit our model to the experimental data of the pingpong ball we find a best fit for $c = 0.025$, which with $\phi_{cr} - \phi_{eq} \approx 0.02$ implies that $\widetilde{c} \approx 1.3$, in agreement with our expectation.

Finally, for the last parameter of our model, $\kappa$, some more extensive analysis is necessary. To this end, let us note that the last equation of Eq. (3.13) can be immediately solved implicitly using the integrating factor method. We then find that $\exp(\widetilde{\kappa}t)$ is the integrating factor for this equation leading to:

$$\delta\widetilde{\varphi}(\widetilde{t}) = e^{-\widetilde{\kappa}\widetilde{t}}\left[1 + \widetilde{c}\int_{\widetilde{t}'=0}^{\widetilde{t}} \frac{\dot{\widetilde{x}}(\widetilde{t}')}{\widetilde{x}(\widetilde{t}')} e^{\widetilde{\kappa}\widetilde{t}'} d\widetilde{t}'\right], \tag{3.14}$$

where we have used the initial condition $\delta\widetilde{\varphi}(0) = 1$. Of course, the solution $\widetilde{x}(\widetilde{t})$ of the first equation still needs to be inserted in this equation. Since $\widetilde{B} \ll 1$, we now neglect the second term in the first equation of Eq. (3.13) we simply find that $\widetilde{x}(\widetilde{t}) = -1 + \frac{1}{2}(\mu/m)\widetilde{t}^2$. Using this approximation with $\mu/m = 1$ and setting $\widetilde{c} = 1$ in Eq. (3.14), we can calculate the duration $\Delta\widetilde{t}$ of and the travelled distance $\Delta\widetilde{x}$ during the cycle.

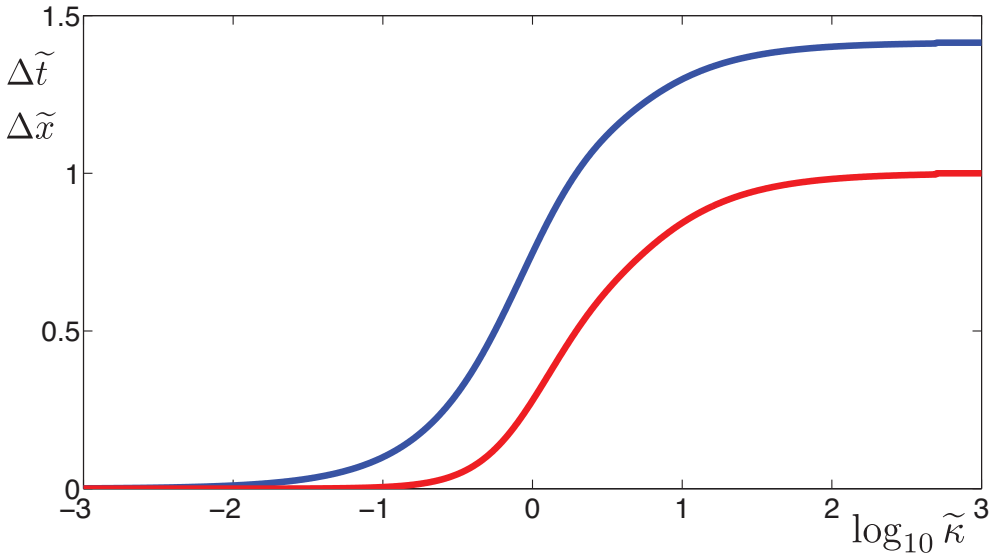


Figure 3.15: The duration $\Delta\widetilde{t}$ (blue curve) of and the travelled distance $\Delta\widetilde{x}$ (red curve) during a stop-go cycle as a function of the logarithm of the relaxation parameter $\widetilde{\kappa}$. Modeled with Eq. 3.14, using $\widetilde{B} \ll 1$ and $c = 1$;

These quantities are plotted as a function of the relaxation parameter $\widetilde{\kappa}$ in Fig. 3.15. For very small values of $\widetilde{\kappa}$ ($< 0.1$) we have very small durations and travelled distance. This happens because now the relaxation time scale is much larger than the gravitational time scale, which implies that as soon as the jammed layer starts to relax, the system quickly reaccelerates and jams again. $\delta\widetilde{\phi}$ will never move far from 1, i.e., $\phi$ will always be close to $\phi_{cr}$. Here the object effectively gets stuck inside the cornstarch suspension (at the observable, gravitational time scales). On the other hand, for very large values of $\widetilde{\kappa}$ ($> 10$) the opposite happens: we have a duration close to $\sqrt{2}$ corresponding to a travelled distance of $\Delta\widetilde{x} \approx 1$, which means that in this single cycle the object moves all the way to the bottom and only jams when it very quickly squeezes the very last thin layer of suspension. Here, the relaxation time scale is much smaller than the gravitational time scale, which implies that the system very quickly relaxes to the quiescent state $\phi \approx \phi_{eq}$ and the gravitational acceleration is not fast enough to jam the material. Here the object effectively never jams and never goes into a stop-go cycle.

Now, when we fit our model to the experimental data of the pingpong ball we find a best fit for $\kappa \approx 40$ s$^{-1}$, which corresponds to a relaxation time scale of $1/\kappa \approx 0.025$ s. Since for $x_0 \approx 1$ cm the gravitational timescale is $\sqrt{x_0/g} \approx 0.032$ s, this leads to $\widetilde{\kappa} \approx 1.3$. In [15] we found the value of $\kappa \approx 40$ s$^{-1}$ to be connected to a Darcy's flow

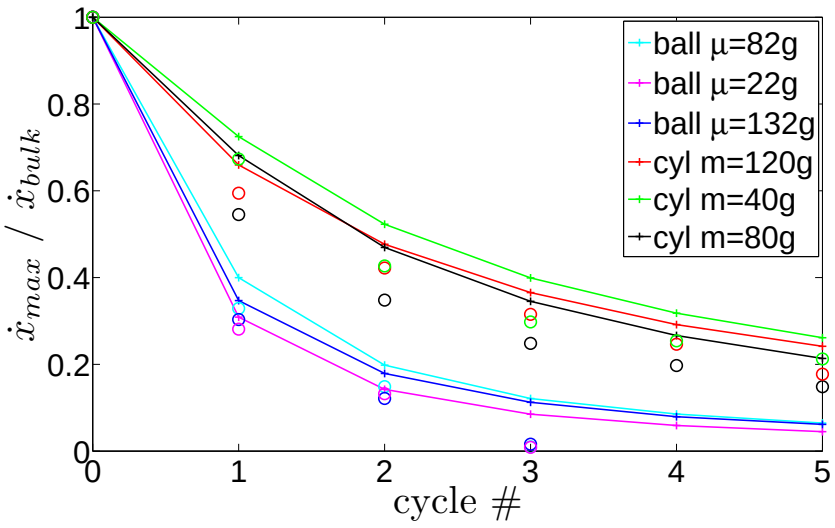


Figure 3.16: The maximum velocities reached during the stop-go-cycles in the experiments (circles) and the model (lines) per jump, normalized by the mean bulk velocity, positioned at cycle 0.

on a scale of 100 cornstarch particle diameters, which is consistent with mesoscopic length scales that have been found in these suspensions [8]. With this model we also understand why we do not see the stop-go cycles for lower packing fractions, as $\kappa$ will be larger and $c$ will be smaller. As a result, the effect will move closer to the bottom, such that it is not measurable within our experimental resolution.

Above, and in [15] we observed that the model works quite well for the first stop-go cycle of the spherical object, but fails for the subsequent cycles which we attributed to the curved surface of the sphere. However, we expect the model to work better for a cylinder, which has a flat bottom and therefore the jammed cornstarch suspension layer is expected to be closer to the modeled cylindrical shape than for the sphere. When we compare the model to the experiments, see Fig. 3.13, we indeed see that now the second stop-go cycle also matches the experiment quite well, and also the experimentally observed number of cycles comes closer to the number we see in the model. Another important point to make is that we kept the same value for $\kappa = 40$ s$^{-1}$ as for modeling the pingpong ball, which indeed should be just dependent on the suspension. We did increase the compression factor from 0.025 for the sphere to 0.07 for the cylinder, which also stands to reason given the different geometry.

To quantify this difference between the ball and the cylinder we plot the maximal velocities in the successive stop-go cycles in Fig. 3.16, normalized by the average

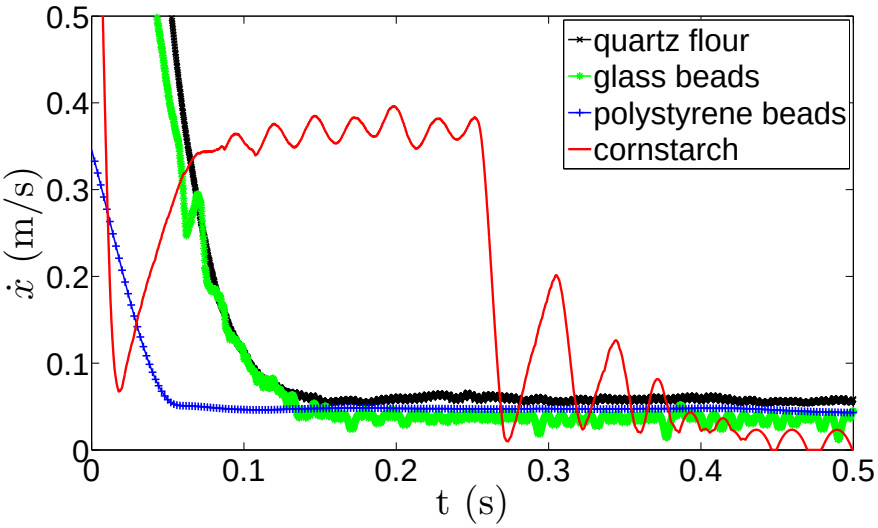


Figure 3.17: Time evolution of the velocity of a steel sphere with a diameter of 1.6 cm in three different suspensions: quartz flower, polystyrene beads, glass beads, and cornstarch. Clearly, both the bulk oscillations and the stop-go cycles are only observable in the cornstarch suspension.

bulk velocity, for both the experiments and the model. Clearly, the experiments of the ball and those of the cylinder follow two different paths: In the case of the pingpong ball the cycles damp out very fast, whereas the cylinder has a more gradual decrease in maximal velocities. The model follows both sets quite well, but overpredicts the number of cycles for the ball to a larger extent than for the cylinder, consistent with the above arguments.

## 3.6 Other suspensions

It is known that different suspensions can behave quite differently, which is presumably connected to particle shape and size distribution. An example of this is their behavior when shaken vertically [11–14], where for comparable solid fractions one may e.g. observe stable holes, growing or even splitting holes, or closing holes, depending on the suspension that was used. We therefore repeated our settling experiments in a variety of other suspensions. Although dense suspensions of particles are all shear thickening [2], both the bulk oscillations and the stop-go-cycles observed in cornstarch are absent in the other suspensions we studied. This can be seen in Fig. 3.17, where we present settling velocities for suspensions containing quartz flour, glass

beads, polystyrene beads, and compare these with a cornstarch suspension.

More specifically, as alternatives to cornstarch, we used monodisperse spherical particles made of polystyrene with a diameter of 20 $\mu$m, polydisperse glass spheres with diameters between 0 and 20 $\mu$m, and quartz flour of 0-50 $\mu$m, in which the particles have edgy, irregular shapes.

For the glass and quartz flour particles, only thin layers were used without full density matching and with a very high solid fraction. In these thin layers, we hoped to encounter stop-go-cycles, but these were not observable. It is possible that the absence of the stop-go-cycles is caused by the size distribution of these particles, because in both cases there is a large amount of small particles that can get between the fewer larger ones. This causes that no sudden rearrangements of particles can happen, which we believe to be the cause of the phenomena we see. For the monodisperse spherical polystyrene beads ($d = 20$ $\mu$m, $\phi \sim 0.6$) we did use a deep bath of suspension. However, also in this case no bulk oscillations or stop-go-cycles were observed. Another difference is that the instant velocity drop after impact on a cornstarch suspension [21] is far less abrupt for the other suspensions we used, which suggests that a much smaller jammed region is created below the impacting object compared to cornstarch.

The remaining questions is what sets aside cornstarch to these particles. If the origin is geometrical, it is most likely a combination of size, size distribution and shape. It would be interesting if there would exist an alternative to cornstarch, i.e., a rather monodisperse sample of edgy, cube-like particles with diameters of 20 $\mu$m or somewhat larger, that could be produced in large enough quantities to perform settling experiments. To our knowledge such an alternative is not available.

## 3.7 Conclusions

In conclusion, we presented experiments of objects settling into a dense bed of a cornstarch suspension, which revealed pronounced non-Newtonian behavior: Instead of reaching a terminal velocity and monotonously stopping at the bottom, the object's velocity oscillates within the bulk and goes through a series of stop-go cycles at the bottom. These effects are not observed in a wide range of other dense suspensions, leading us to believe that cornstarch particles have some unique property. We were not able to pinpoint this property, but suggest that it may be connected to the particular shape and size distribution of the particles.

We studied the influence of several parameters on the observed phenomena, and found that both disappear if the solid fraction of cornstarch particles is below $\phi \approx$

0.38. This suggests that contact forces must play an important role in creating the observed behavior. If the density ratio between the object and the cornstarch suspension (which always is larger than 1) becomes low, the bulk oscillations disappear, but the stop-go cycles are still clearly observable. Other parameters that were studied are the object shape and the container size.

We discussed several models in the context of the bulk oscillations and concluded that common shear thickening and linear viscoelastic models fail to account for the observed phenomena. A hysteretic drag model captures the basic phenomenology in the bulk. However, the model is entirely phenomenological, and a link between the model parameters and the physical properties of the system still needs to be established.

We proposed a jamming model that describes the stop-go cycles near the bottom, and discuss its properties and its plausibility. The model is capable of describing both our experiments with spheres and cylinders of variable mass, and works particularly well for the experiments done with a cylinder. This stands to reason because the geometry of the cylinder is closest to the geometry assumed in the model.

## 3.8 Appendix: Linear viscoelastic models

In this Appendix we will first discuss a model for the drag a sphere experiences based on the Maxwell fluid rheology. Subsequently we will solve the equation of motion for a settling sphere [Eq. (3.1)] in such a fluid using Laplace transformations, and finally we will discuss extensions to the Maxwell fluid, namely the extended Maxwell model and the modified Kelvin-Voigt solid, that contain additional dissipative elements.

Linear viscoelastic models for the drag force $D$ (just like the constitutive stress-strain (rate) relations for a viscoelastic fluid) are equations composed of elastic and viscous terms which provide a relation between drag and displacement for the first and drag and velocity for the second, or

$$\dot{D} = -E\dot{x}\,; \quad D = -\eta\dot{x}\,, \tag{3.15}$$

in which we have taken the time derivative of the first relation for practical reasons. The proportionality constant $E$ has the dimensions of a spring constant and $\eta$ has the dimensions of viscosity times length.

A Maxwell fluid consists of an elastic and a viscous term in series (Fig. 3.18a), such that $\dot{x}$ is the sum of an elastic and a viscous part that both are subject to the same force such that

$$-\dot{x} = \frac{\dot{D}}{E} + \frac{D}{\eta}\,. \tag{3.16}$$

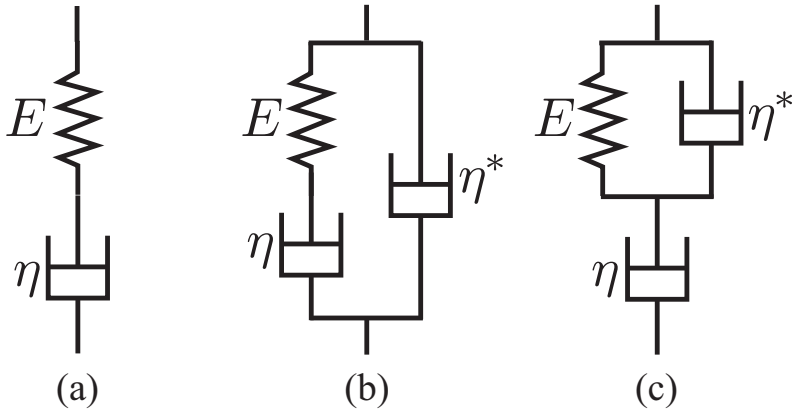


Figure 3.18: Schematics of the three linear viscoelastic models discussed in this Appendix: (a) Maxwell fluid, (b) extended Maxwell fluid, and (c) modified Kelvin-Voigt solid.

Writing $D = \int_0^t \psi(t-t')\dot{x}(t')dt'$ and inserting this into Eq. (3.16) impliess that $\psi(t)$ should be the solution of that equation with $\dot{x} = \delta(t)$, the Dirac delta function. This can be solved by first finding the solution to the homogeneous problem [inserting $\dot{x} \equiv 0$ in Eq. (3.16)] and subsequently integrating the full equation (with $\dot{x} = \delta(t)$) over a short interval around $t = 0$. This yields

$$\psi(t) = -E \exp\left[-\frac{E\,t}{\eta}\right], \tag{3.17}$$

leading to the drag of Eq. (3.3) and by insertion into the equation of motion Eq. (3.1) we obtain

$$m\ddot{x} = \mu g - E \int_{t'=0}^{t} \exp\left[-\frac{E\,(t-t')}{\eta}\right] \dot{x}(t')\,dt'. \tag{3.18}$$

Introducing the Laplace transforms of the velocity $u = \dot{x}$ and the function $\psi$, namely $\widetilde{u}(s) \equiv \int_0^\infty \exp(-st)\dot{x}(t)dt$ and $\widetilde{\psi}(s) \equiv \int_0^\infty \exp(-st)\psi(t)dt$ respectively, we obtain by transforming Eq. (3.18) using standard Laplace techniques

$$ms\widetilde{u}(s) - mu(0) = \frac{\mu g}{s} + \widetilde{\psi}(s)\,\widetilde{u}(s). \tag{3.19}$$

Also, we obtain from Eq. (3.17) that $\widetilde{\psi}(s) = -E/(s+E/\eta)$ with which

$$\left(ms + \frac{E}{s+E/\eta}\right)\widetilde{u}(s) = \frac{\mu g}{s} + mu(0). \tag{3.20}$$

The limit $t \to \infty$ corresponds to the limit $s \downarrow 0$ of the Laplacetransform, which when applied to Eq. (3.20) leads to $\lim_{s\downarrow 0} \widetilde{u}(s) = \mu g/(\eta s)$ or $\lim_{t\to\infty} u(t) = \mu g/\eta$. Therefore there is a terminal velocity $u_T = \mu g/\eta$. Subtracting this terminal velocity by introducing a new variable $\widetilde{v} = \widetilde{u} - \mu g/(\eta s)$ (or, equivalently $v(t) = u(t) - \mu g/\eta$) we obtain after some algebraical manipulation of Eq. (3.20)

$$\widetilde{v}(s) = v_0 \frac{s+\alpha}{(s+\alpha)^2+\omega^2} + \left(\frac{\mu g}{\omega m} + \frac{E v_0}{2\omega\eta}\right) \frac{\omega}{(s+\alpha)^2+\omega^2}, \tag{3.21}$$

with $\alpha = E/(2\eta)$, $\omega = \sqrt{E/m - \alpha^2}$, and $v_0 = u(0) - \mu g/\eta$. The (standard) inverse transform of this equation directly leads to Eq. (3.4)

$$\dot{x}(t) = u_T + e^{-\alpha t}\left[v_0 \cos\omega t + \left(\frac{\mu g}{\omega m} + \frac{E v_0}{2\omega\eta}\right)\sin\omega t\right]. \tag{3.22}$$

The slightly more complicated extended Maxwell fluid (Fig. 3.18b) and modified Kelvin-Voigt solid (Fig. 3.18c) are defined by

$$\begin{aligned} D &= D_L + D_R \\ -\dot{x} &= \dot{D}_R/E + D_R/\eta = D_L/\eta^*, \end{aligned} \tag{3.23}$$

for the extended Maxwell fluid, and

$$\begin{aligned} D &= D_L + D_R \\ -\dot{x} &= D/\eta + D_R/\eta^* = D/\eta + \dot{D}_L/E, \end{aligned} \tag{3.24}$$

for the modified Kelvin-Voigt solid. Along a similar path leading to Eq. (3.17), this leads to the following equation for the extended Maxwell fluid (eM) kernel $\psi_{\rm eM}(t)$

$$\psi_{\rm eM}(t) = -\left[E\exp\left(-(E/\eta)t\right) + \eta^*\delta(t)\right], \tag{3.25}$$

which leads directly to its Laplace transform

$$\widetilde{\psi}_{\rm eM}(s) = -\left[\frac{E}{s+E/\eta} + \eta^*\right]. \tag{3.26}$$

For the modified Kelvin-Voigt solid (mKV) the situation is slightly more complicated because the analysis leads to an integral equation for $D$ and $\dot{x}$ that appears hard to solve for $D$

$$\begin{aligned} &\textstyle\int_0^t \left[(1+\eta^*/\eta)\delta(t-t') + E/\eta\right] D(t')dt' \\ &\quad = -\textstyle\int_0^t \left[E + \eta^*\delta(t-t')\right]\dot{x}(t')dt', \end{aligned} \tag{3.27}$$

however, we only are interested in the Laplace transform $\widetilde{\psi}_{\mathrm{mKV}}(s)$ which is readily obtained from the Laplace transform of the above equation realizing that $\widetilde{\psi}_{\mathrm{mKV}}(s) \equiv \widetilde{D}(s)/\widetilde{u}(s)$

$$\widetilde{\psi}_{\mathrm{mKV}}(s) = -\frac{E/s+\eta^*}{(1+\eta^*/\eta)+E/(\eta s)}\,. \tag{3.28}$$

Actually, both kernels are equivalent which can be seen by introducing a set of new parameters, namely for eM: $\bar{E} \equiv E(1+\eta^*/\eta)$, $\bar{\eta} \equiv \eta(1+\eta^*/\eta)$, and $\bar{\eta}^* \equiv \eta^*$ and for mKV: $\bar{E} \equiv E/(1+\eta^*/\eta)$, $\bar{\eta} \equiv \eta$, and $\bar{\eta}^* = \eta^*/(1+\eta^*/\eta)$. With this, both kernels become:

$$\widetilde{\psi}(s) = -\frac{\bar{E}+\bar{\eta}^* s}{s+E/\bar{\eta}}\,. \tag{3.29}$$

Inserting this $\psi(s)$ into the equation of motion Eq. (3.19) gives

$$\left(ms+\frac{\bar{E}+\bar{\eta}^* s}{s+E/\bar{\eta}}\right)\widetilde{u}(s) = \frac{\mu g}{s}+mu(0)\,. \tag{3.30}$$

Again, the limit $t\to\infty$ teaches us that there is a terminal velocity $u_T = \mu g/\bar{\eta}$ and introducing a new variable $\widetilde{v} = \widetilde{u} - \mu g/(\bar{\eta} s)$ some algebraical manipulation leads to

$$\begin{aligned}\widetilde{v}(s) &= v_0\frac{s+\alpha}{(s+\alpha)^2+\omega^2}+ \\ &\left[(1-\bar{\eta}^*/\bar{\eta})\frac{\mu g}{\omega m}+\left(\frac{\bar{E}}{\bar{\eta}}-\frac{\bar{\eta}^*}{m}\right)\frac{v_0}{2\omega}\right]\frac{\omega}{(s+\alpha)^2+\omega^2}\,,\end{aligned} \tag{3.31}$$

with $\alpha \equiv (\bar{E}/\bar{\eta}+\bar{\eta}^*/m)/2$, $\omega = \sqrt{\bar{E}/m-\alpha^2}$, and $v_0 = u(0)-\mu g/\bar{\eta}$. The above equation can be instantly transformed back into the time domain leading to a similar expression as Eq. (3.22). The particular case $v_0 = 0$ of this inverse transform reads

$$\dot{x}(t) = u_T + e^{-\alpha t}\left[\left(1-\frac{\bar{\eta}^*}{\bar{\eta}}\right)\frac{\mu g}{\omega m}\right]\sin\omega t\,. \tag{3.32}$$

Note that now the oscillational term has its smallest amplitude $A$. When we follow a similar line of reasoning as we did in Section 3.4.2 and compute the ratio of amplitude and terminal velocity we obtain

$$\frac{A}{u_T} = \left(1-\frac{\bar{\eta}^*}{\bar{\eta}}\right)\frac{\mu g}{m\omega}\frac{\bar{\eta}}{\mu g} = \frac{\bar{\eta}-\bar{\eta}^*}{m\omega} \approx \frac{\bar{\eta}-\bar{\eta}^*}{m\omega_0}\,. \tag{3.33}$$

This ratio can be small if $\bar{\eta}^* \approx \bar{\eta}$, which equation for both eM and mKV lead to $\eta^* \approx \eta^* + \eta$, which means that $\eta$ and $\eta^*$ both need to be small (compared to $m\omega_0$).

What does this imply for the ratio of the damping time $\tau = 1/\alpha$ and the oscillation period $T = 2\pi/\omega$? We have

$$2\pi\frac{\tau}{T} = \frac{\omega}{\alpha} = \frac{2\omega}{(E/\bar{\eta} + \bar{\eta}^*/m)} \approx \frac{2\omega\bar{\eta}}{E} = \frac{2\omega\bar{\eta}}{m\omega_0^2} \approx \frac{2\bar{\eta}}{m\omega_0}\,, \tag{3.34}$$

where for the first approximate equality we used that $\bar{\eta}$ and $\bar{\eta}^*$ are both small and for the second one that $\omega$ is of the same order as $\omega_0 = \sqrt{E/m}$. Now, both $A/u_T$ and $\tau/T$ are of order $\bar{\eta}/(m\omega_0)$. So if $A/u_T$ is small (as it should be in order to have the oscillations with amplitude smaller than drift velocity we observe), then so should $\tau/T$. And if $\tau/T$ is small, this means that the oscillation will damp out well within a single period, which contradicts the observations. Therefore, also the eM and mKV models are not capable of describing the observed bulk oscillations.

## References

[1] N. Wagner and J. Brady, "Shear thickening in colloidal dispersions", Phys. Today **62**, 27 (2009).

[2] H. Barnes, "Shear-thickening (dilatancy) in suspensions of nonaggregating solid particles dispersed in newtonian liquids", J. Rheol **33**, 329 (1989).

[3] A. Fall, N. Huang, F. Bertrand, G. Ovarlez, and D. Bonn, "Shear thickening of cornstarch suspensions as a reentrant jamming transition", Phys. Rev. Lett. **100**, 018301 (2008).

[4] E. Brown and H. Jaeger, "Dynamic jamming point for shear thickening suspensions", Phys. Rev. Lett. **103**, 086001 (2009).

[5] E. Brown, N. Forman, C. Orellana, H. Zhang, B. Maynor, D. Betts, J.M.DeSimone, and H. Jaeger, "Generality of shear thickening in suspensions", Nat. Mater. **9**, 220 (2010).

[6] C. Bonnoit, T. Darnige, E. Clement, and A. Lindner, "Inclined plane rheometry of a dense granular suspension", J. Rheol. **54**, 65 (2010).

[7] E. Brown and H. Jaeger, "Generality of shear thickening in dense suspensions", J. Rheol. **56**, 875–923 (2012).

[8] C. Bonnoit, J. Lanuza, A. Lindner, and E. Clement, "Mesoscopic length scale controls the rheology of dense suspensions", Phys. Rev. Lett. **105**, 108302 (2010).

[9] A. Fall, F. Bertrand, G. Ovarlez, and D. Bonn, "Shear thickening of cornstarch suspensions", .

[10] E. B. White, M. Chellamuthu, and J. Rothstein, "Extensional rheology of a shear-thickening cornstarch and water suspension", Rheol. Acta **49**, 119–129 (2010).

[11] F. Merkt, R. Deegan, D. Goldman, E. Rericha, and H. Swinney, "Persistent holes in a fluid", Phys. Rev. Lett. **92**, 184501 (2004).

[12] R. Deegan, "Stress hysteresis as the cause of persistent holes in particulate suspensions", Phys. Rev. E **81**, 036319 (2010).

[13] H. Ebata, S. Tatsumi, and M. Sano, "Expanding holes driven by convectionlike flow in vibrated dense suspensions", Phys. Rev. E **79**, 066308 (2009).

[14] H. Ebata and M. Sano, "Self-replicating holes in a vertically vibrated dense suspension", Phys. Rev. Lett. **107**, 088301 (2011).

[15] S. von Kann, J. Snoeijer, D. Lohse, and D. van der Meer, "Nonmonotonic settling of a sphere in a cornstarch suspension", Phys. Rev. E **84**, 060401 (2011), chapter 2 of this thesis.

[16] B. Liu, M. Shelley, and J. Zhang, "Focused force transmission through an aqueous suspension of granules", Phys. Rev. Lett. **105**, 188301 (2010).

[17] N. Abaid, D. Adalsteinsson, A. Agyapong, and R. McLaughlin, "An internal splash: Levitation of falling spheres in stratified fluids", Phys. Fluids **16**, 1567 (2004).

[18] B. Akers and A. Belmonte, "Impact dynamics of a solid sphere falling into a viscoelastic micellar fluid", J. Non-Newtonian Fluid Mech. **135**, 97 (2006).

[19] M. Arigo and G. McKinley, "The effects of viscoelasticity on the transient motion of a sphere in a shear-thinning fluid", J. Rheol. **41**, 103 (1997).

[20] D. Lohse, R. Rauhé, R. Bergmann, and D. van der Meer, "Granular physics: Creating a dry variety of quicksand", Nature **432**, 689–690 (2004).

[21] S. Waitukaitis and H. Jaeger, "Impact-activated solidification of dense suspensions via dynamic jamming fronts", Nature **487**, 205–209 (2012).

[22] J. Willett, "Packing characteristics of starch granules", Cereal Chem. **78**, 64 (2001).

# 4

# Phase diagram of vertically vibrated dense suspensions *

*When a hole is created in a layer of a dense, vertically vibrated suspension, phenomena are known to occur that defy the natural tendency of gravity to close the hole. Here, an overview is presented of the different patterns that we observed in a variety of dense particulate suspensions. Subsequently, we relate the occurrence of these patterns to the system parameters, namely the layer thickness, the particle concentration, and the shaking parameters. Special attention is given to the geometric properties of the particles in the various suspensions such as shape and particle distribution.*

*Stefan von Kann, Jacco H. Snoeijer, and Devaraj van der Meer, Phase diagram of vertically vibrated dense suspensions, preprint (2012).

## 4.1 Introduction

Concentrated particulate suspensions consist of a homogeneous fluid containing particles larger than one micrometer, so that Brownian motion is negligible. They can be found in many places, and their flow is important in nature, industry and even health care [1]. In spite of their significance, many aspects of the flow of dense suspensions remain poorly understood. In order to study these materials people have used methods inspired by classical rheology, and typically characterized them in terms of a constitutive relation of stress versus shear rate [2–6]. A general result is that, when increasing the shear rate, dense suspensions first tend to become less viscous (shear thinning) and subsequently shear thicken.

Probably the most conspicuous example of a dense suspension is formed by a high concentration of cornstarch in water. One could actually run over a bath filled with a cornstarch suspension, but one would sink when standing still [7]. This is caused by solidification, activated by impact [8].

Rheological experiments in cornstarch have revealed the existence of a large shear-thinning regime that terminates in an extremely sudden shear thickening [9]. In other rheological experiments people found a mesoscopic length scale [6, 10], a dynamic jamming point [4], and fracturing [11].

Not only is the rheology of cornstarch suspensions very distinct, but unexpected phenomena were also found in experiments beyond the classical rheological ones. In experiments in which an object was left to sink into a cornstarch suspension, non-monotonic settling was observed [12], together with the formation of a jammed region between the object and container bottom [12, 13]. Merkt *et al.* [14] observed in a vertically shaken, thin layer of cornstarch suspension that, amongst other exotic phenomena, stable oscillating holes can be formed at certain frequencies and amplitudes [14]. These were subsequently described using a phenomenological model based on a hysteretic constitutive equation [15]. In other suspensions similar stable holes have not been reported, except for [14], where they were also found in glass bead suspensions. In potato starch and glass bead suspensions, Ebata *et al.* found growing and splitting holes, and a separated state respectively [16, 17]. They attributed the first to a convection-like flow, but do not comment on the origin of the latter phenomenon. Stable holes and kinks (which are markedly similar to the separated state of [16, 17]) have recently also been observed in emulsions [18]. At present we are still far from a quantitative understanding of why the above phenomena occur, and why different suspensions may behave differently.

The purpose of this work is to make an extensive inventory of the different phenomena that can occur in various vertically shaken dense particulate suspensions and in what sense cornstarch suspensions occupy a unique position amongst them. We will do this by subjecting several suspensions, including several of the suspensions

mentioned before, to vertical vibrations. We then observe, describe and, whenever possible, explain the different phenomena. For cornstarch we present a wider range of variables, including layer depth and packing fraction, which actually leads to the observation of some hitherto unreported phenomena. From the experiments with other particles we find a dependence of particle properties on the observed phenomena.

This chapter is organized as follows: In Section 4.2 the experimental setup and working procedure are introduced, after which we present the various phenomena we observe in a variety of vibrated suspensions in Section 4.3. After that, in Section 4.4, we will turn to the suspensions we have examined and quantify how these phenomena depend on the concentration, layer depth, and shaking parameters. In doing so we will use cornstarch as our "benchmark" material and relate the properties of the other particles used in suspension to those of cornstarch. Section 4.5 will conclude the chapter.

## 4.2 Experimental setup and procedure

### 4.2.1 Setup

The experimental setup is shown in Fig. 4.1. The core consists of a cylindrical container with a diameter $D = 11.0$ cm and a height $H$ of 8.0 cm. This container is vertically vibrated by a shaker (TiraVib 50301) with frequencies $f$ between 20 and 200 Hz and a dimensionless acceleration $\Gamma$ from 0 up to 60. Here, $\Gamma = a(2\pi f)^2/g$, where $a$ is the shaking amplitude and $g$ the gravitational acceleration. Like any electromagnetic shaker, the parameter range attainable by the TiraVib 50301 is limited in amplitude ($< 12.8$ mm), velocity ($< 1.5$ m/s) and acceleration ($< 110g$). The container is filled up to a variable height $h$ between 0.4 and 2 cm with a suspension of varying composition. The suspension layer in the container is recorded with a high speed camera at various frame rates, given in frames per second (fps), and is either imaged from the side or from the top.

### 4.2.2 Procedure

Suspensions consist of a suspending liquid and particles. However, mixing two arbitrary constituents of these types does not always lead to a useful and stable suspension. First of all, when particles are hydrophylic water can be used as a suspending liquid, but for hydrophobic particles we have to turn to other suspending liquids. Secondly, even when a suitable suspending liquid has been found, particles denser than the liquid are likely to sediment, such that a density matching agent needs to be used. We used a variety of particles to create our suspensions, each with their own properties, an overview of which is presented in table 4.1. A more detailed description of

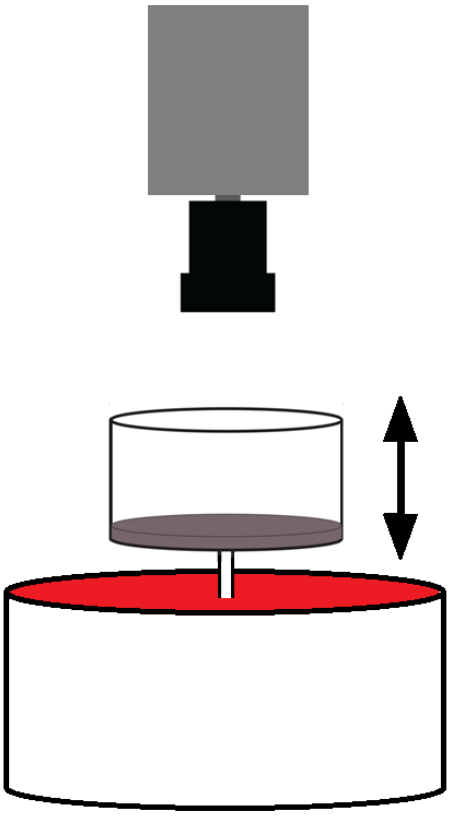

Figure 4.1: A schematic view of the used setup. At the lower end we have the shaker, on top of which the container with the suspension is mounted, which is subsequently vibrated vertically. Above that is the high speed camera, in this case recording the suspension from above.

each suspension can be found in the experimental part where their properties will be discussed in relation to the experimental results.

For the hydrophylic particles we used demineralized water as the suspending liquid, but the particles are typically more dense than water. When this density contrast is large (e.g. glass in water) density matching of the liquid is required. To this end we used two different salts: Cesium Chloride (CsCl) for densities up to $1.8 \cdot 10^3$ kg/m$^3$ and Sodium Polytungstate ($Na_6[H_2W_{12}O_{40}]$) for densities up to $2.5 \cdot 10^3$ kg/m$^3$. Some of our particles are hydrophobic, making water unsuitable as the suspending liquid. For suspending these particles we used sunflower oil. An important parameter for our suspensions is the concentration, which we express as the volume fraction $\phi$ that is occupied by the solid phase in the suspension. In this work we will concentrate on dense suspensions, and it should be kept in mind that all of the described phenomena will disappear when the suspension is sufficiently diluted.

For the suspensions and (quite viscous) Newtonian liquids we have used in our container and the shaking amplitudes and frequencies used in this study, the vibrated fluid is typically at rest. The liquid surface is typically smooth, on top of which, if the shaking conditions are favorable we may observe Faraday waves [19] of very small wavelength. The phenomena we report in this work occur only after a manual disturbance has been made in the liquid. This was either done by puffing air into the layer using a straw, or by poking a hole into the fluid with a stick.

## 4.3 Phenomenology

In this Section we will describe the several possible states and phenomena we observe after the initial perturbation has been created in the liquid.

### 4.3.1 Newtonian liquid

Let us first briefly discuss what happens when a very viscous Newtonian liquid is vibrating vertically, and a perturbation is created in the form of a hole. To this end, we put a layer of honey with a thickness $h = 0.6$ cm and a dynamic viscosity $\mu \approx 6.3$ Pa·s in our setup. Without vibration, the hole will collapse under the influence of hydrostatic pressure. The same happens when the layer is vibrated and a hole is created, only now we observe that the edges of the hole oscillate along with the driving frequency. In Fig. 4.2 we plot the time evolution of the diameter of the hole and we observe that the diameter actually decreases approximately linearly in time. On top of this decrease, we observe an oscillation at the same frequency as that of the shaker.

| Particles | Size and distribution | Density | Shape | Liquid used |
|---|---|---|---|---|
| cornstarch | 5-20 $\mu$m flat | $1.7 \cdot 10^3$ kg/m$^3$ | edgy | demineralized water |
| glitter | 50 or 100 $\mu$m monodisperse | $1.5 \cdot 10^3$ kg/m$^3$ | flat quadrangles | sunflower oil |
| polystyrene beads | 20 $\mu$m monodisperse | $1.05 \cdot 10^3$ kg/m$^3$ | spheres | demineralized water |
| glass beads | 0-20$\mu$m* | $2.5 \cdot 10^3$ kg/m$^3$ | spheres | demineralized water |
| quartz flour | 0-70$\mu$m* | $2.5 \cdot 10^3$ kg/m$^3$ | edgy | demineralized water |

Table 4.1: Schematic overview of the particles and their properties, used in this study. A flat size distribution stands for an equal amount of particles for every size. The * indicates a very inhomogeneous size distribution, consisting mainly of smaller particles and a strongly decreasing amount of particles when going bigger in size.

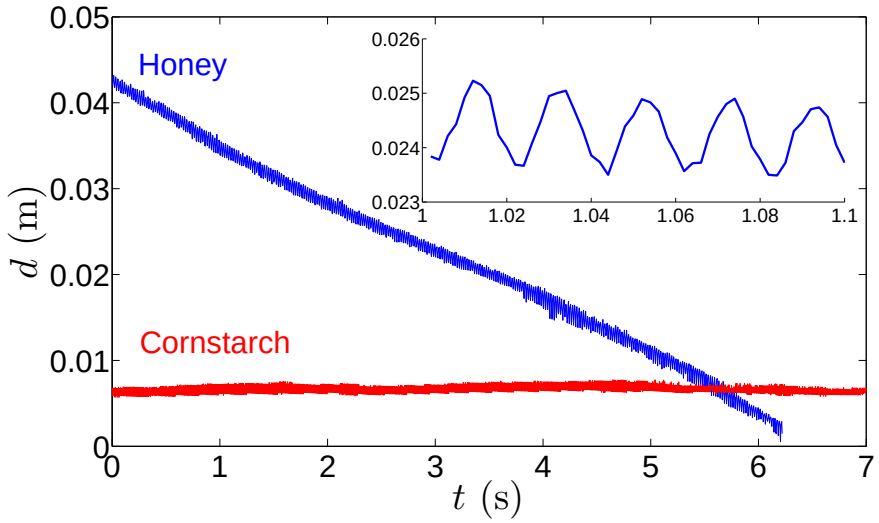


Figure 4.2: Comparison of the time evolution of the diameter of a hole created in a layer of honey of thickness $h = 6$ mm which is vibrated at a frequency $f = 50$ Hz and a dimensionless acceleration $\Gamma = 30$, recorded at 250 fps, and that of a hole created in a layer of cornstarch suspension ($h = 7$ mm) at $f = 100$ Hz and $\Gamma = 20$, recorded at 500 fps. The inset shows a few cycles from the experiment in honey (at 500 fps), clearly showing the oscillations of the edge with the driving frequency.

### 4.3.2 Cornstarch suspensions

Contrary to Newtonian fluids, in suspensions hydrostatic pressure can be dynamically overcome due to the imposed vibration. The hole will not (fully) close, and a rich variety of phenomena can be observed. The richest phenomenology is found in cornstarch suspensions, where upon varying our experimental parameters we found four different phenomena. In accordance with the existing literature we named stable holes, and fingers [14]. We also found two unreported phenomena which we will call rivers, and jumping liquid. From each of these states, a snapshot can be found in Fig 4.3. We will now discuss the characteristics of these phenomena in detail.

#### Stable holes

When an initial perturbation either grows or shrinks to a circular hole of constant average diameter, we speak of a stable hole [see Fig. 4.3(a)]. In the vertical direction such a hole typically extends to the bottom of the container, and the hole edge oscillates along with the driving frequency.

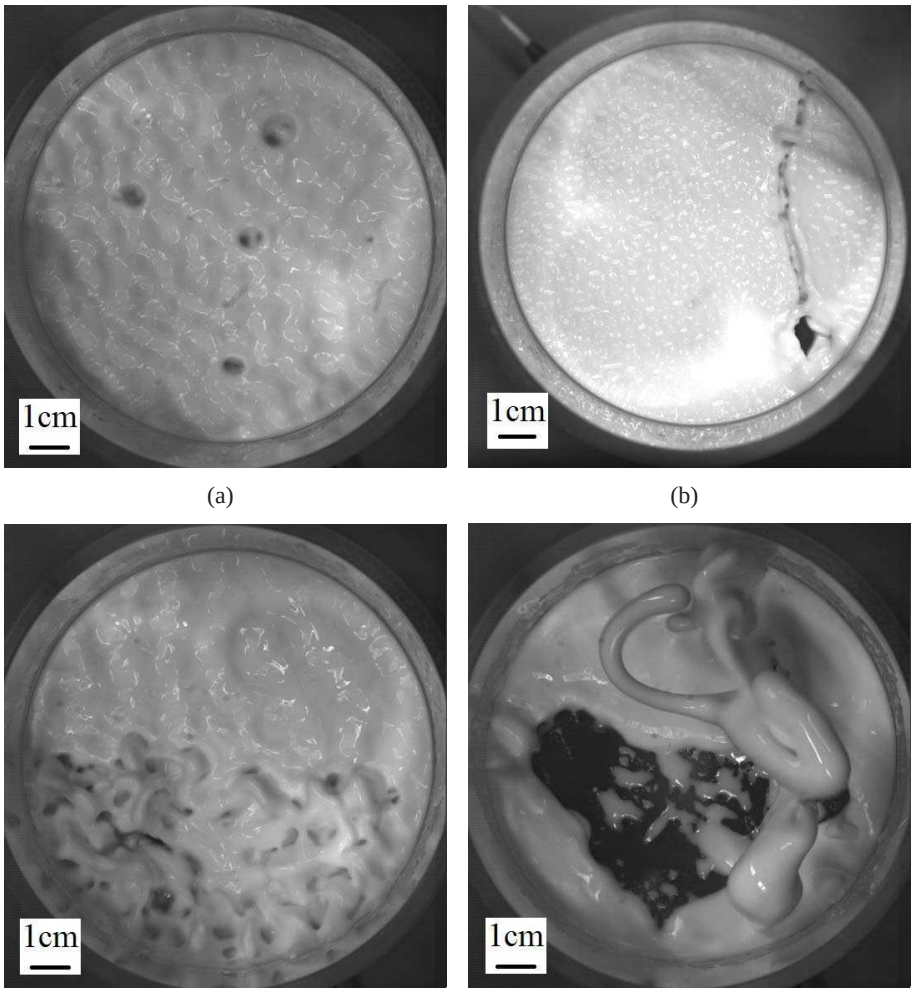


(a) (b)

(c) (d)

Figure 4.3: Snapshots of the four different phenomena that can be observed in a vertically vibrated layer of cornstarch suspension. From left to right: (a) Holes in a suspension layer of thickness $h = 6$ mm and with a concentration $\phi = 0.4$, shaken at $f = 80$ Hz and $\Gamma$=20. (b) River in a $\phi = 0.38$ suspension with $h = 6$ mm, shaken at $f = 140$ Hz, $\Gamma = 40$. (c) Fingers in a $\phi = 0.4$ suspension with $h = 6$ mm, shaken at $f = 80$ Hz with $\Gamma = 30$. (d) Jumping liquid, just after its release from the vibrated layer, in a $\phi = 0.4$ suspension with $h = 6$ mm, shaken at $f = 40$ Hz, $\Gamma = 40$.

Merkt *et al*. [14] attributed the stable holes in the cornstarch suspension to shear thickening. They found that typical shear rates in the shaking experiments were around the same value for which a sudden shear thickening was observed in rheometer experiments. Deegan [15] proposed a one-dimensional hysteretic model to explain why these holes do not collapse due to hydrostatic pressure. In this model he proposed a coexistence of two stable branches in the stress versus strain rate diagram. Based on this, it was argued that the edge of the hole will move inward only slightly during the first half of the cycle (large shear stress), but will then jump to the lower branch such that during the outward motion the suspension experiences a smaller shear stress, resulting in a larger outward displacement. In the one-dimensional model this actually lead to opening holes, but one could imagine that a stable equilibrium radius would be found for the two-dimensional, radially symmetric problem that corresponds to the experiment.

In more recent experiments by Falcón *et al*. [18] the stability of holes in a vibrated emulsions was connected to the normal stress caused by a convection roll in the rim that surrounds the hole. We verified that such a roll is also visible in the rim around the holes in our cornstarch suspensions by putting tracer particles in the hole, which came out along the rim of the hole.

**Rivers**

In cornstarch suspensions with lower concentrations $\phi$, we observe the formation of an elongated structure [Fig. 4.3(b)], which has not been reported before. Due to its shape we denote these from here on as rivers. Also the rivers start from a single perturbation in the suspension, but now the original hole tends to slowly stretch out or "walk" through the suspension. When the river reaches the container wall, it leaves an entire line-shaped structure (or even multiple lines) behind that penetrates the suspension layer all the way to the bottom of the container. The directionality appears to be random. As soon as this river touches the container edges it stabilizes and, just like the stable holes it has a very long lifetime: the structure easily outlives the duration of the experiment, which was typically in the order of $10^5 - 10^6$ cycles.

**Fingers**

Fingers [see Fig. 4.3(c)] are formed at higher shaking strengths. In this regime, the small rim on the edge of the hole increases in size and "lifts off" from the surface. Eventually, the fingers fall down and form new holes, which again grow new fingers. These fingerlike protrusions were also reported by Merkt *et al.* [14].

**Jumping liquid**

The fingers described in the previous paragraph grow larger when, at constant $\Gamma$, the amplitude is increased. For sufficiently large amplitude, while the finger is growing, the connection to the surface may break and a "blob" of suspension will start jumping around in the container [see Fig. 4.3(d)]. Eventually it will form into a spherical shape, and with every bounce on the suspension surface, it slowly shrinks in size over a timespan of minutes. Below a certain size this sphere will coalesce with the surface, a process which either causes a new hole-shaped disturbance to form –eventually leading to the growth of a new amount of jumping liquid– or the sphere is simply absorbed after which the process stops. In order to investigate the packing fraction of the detached balls, we have caught several of these blobs of suspension in flight. It was found that the concentration varied by a few percent, but with an average that was equal to the bulk packing fraction.

### 4.3.3 Other suspensions

Starting from the hypothesis that it is the geometrical shape of the cornstarch particles in the suspension that is responsible for the large variety of phenomena that can be observed in vertically vibrated cornstarch suspensions, we examined a variety of other dense particulate suspensions, with varying geometrical parameters. We however, did not succeed in creating a suspension that presented the similar phenomena as cornstarch. The other suspensions we studied have an interesting phenomenology as well, but it is markedly different from that of cornstarch: Steady states like the stable holes and rivers are absent; instead we find much more dynamic phenomena like the growing and splitting holes we will describe below.

**Splitting holes**

After creating an initial disturbance in a suspensions containing polydisperse particles, we observe a hole that immediately starts to grow and quickly departs from the circular shape: The hole tends to stretch out and eventually splits up into two circular holes. These in turn again grow and become non-circular, leading to another splitting up. This way new holes are formed very rapidly, and as soon as the system is full of holes they are also observed to collide and merge or to fully close. The timescale of the dynamics of splitting and colliding depends strongly on particle type and shaking parameters, and can range from a few seconds up to several minutes. This eventually leads to a very chaotic dynamics. A snapshot of a container with several of these holes can be found in Fig. 4.4.

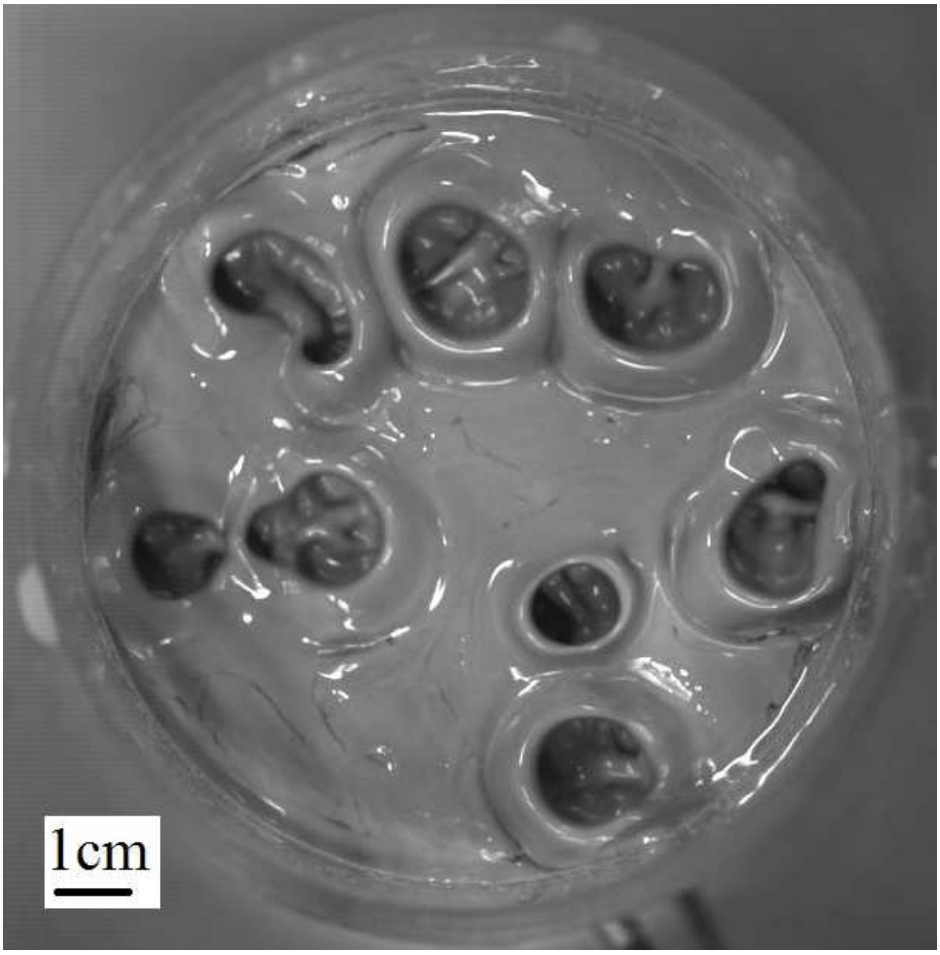


Figure 4.4: Splitting holes in a vibrated polydisperse glass bead suspension with an average diameter of 10 $\mu$m ($f = 100$ Hz, $\Gamma = 25$, and $h = 7$ mm.)

**Growing holes and kinks**

In monodisperse particle suspensions the phenomenology turned out to be very different again. After creating the initial disturbance, a circular hole is formed. Depending on the shaking strength and amplitude we find either of two phenomena: At the lower end we observe a hole that grows until a maximum size is reached. After this it rapidly collapses to a very small size and a growth phase sets in again. When shaking harder, the hole will grow until it hits the container wall. In this case the hole will open up and form a large dry area at the container bottom, thus creating a system that is partly covered with a thick layer of suspension, partly dry and an abrupt transition between them which is called a kink [18]. Snapshots of such a series of events can be found in Fig. 4.5. The distinction between the two states is not always very clear, since in some cases the hole size will saturate, the entire hole will keep on moving slowly inside the container, and eventually come in contact with an edge, which then leads to the formation of a kink. The time span for this to happen however, can be minutes whereas the kink formation described above may happen within seconds.

## 4.4 Quantitative results

Which of the above mentioned phenomena we observe depends on the composition of the suspension, its packing fraction $\phi$, the depth of the layer $h$, as well as the shaking parameters frequency $f$ and shaking strength $\Gamma$. In this Section, we present the results of the experiments done with the various suspensions, and discuss them for every suspension by means of phase diagrams of the shaking parameters $\Gamma$ and $f$.

### 4.4.1 Cornstarch

As cornstarch has proven to have the richest phenomenology, we will start with the discussion of our experiments in cornstarch suspensions. Previously, these type of shaken suspensions have been considered by Merkt *et al*. [14]. Their report, however, was limited to a single set of experiments with a fixed depth and packing fraction, in which only the shaking parameters were varied. Our objective is here is to map out a larger part of the parameter space by in addition varying the layer depth and concentration. More specifically, we want to determine how the phenomena described in [14] (holes and fingers) are influenced by these other parameters, and how the newly described rivers and jumping liquid fit into the phase diagrams.

We use either demineralized water or an aqueous solution of Cesium Chloride (CsCl) with a density of $\approx 1.7 \cdot 10^3$ kg/m$^3$, matching the cornstarch particle density (based on sedimentation experiments: At $\rho = 1.7 \cdot 10^3$ kg/m$^3$ cornstarch particles do not settle to the bottom for several days). Experiments actually showed negligible

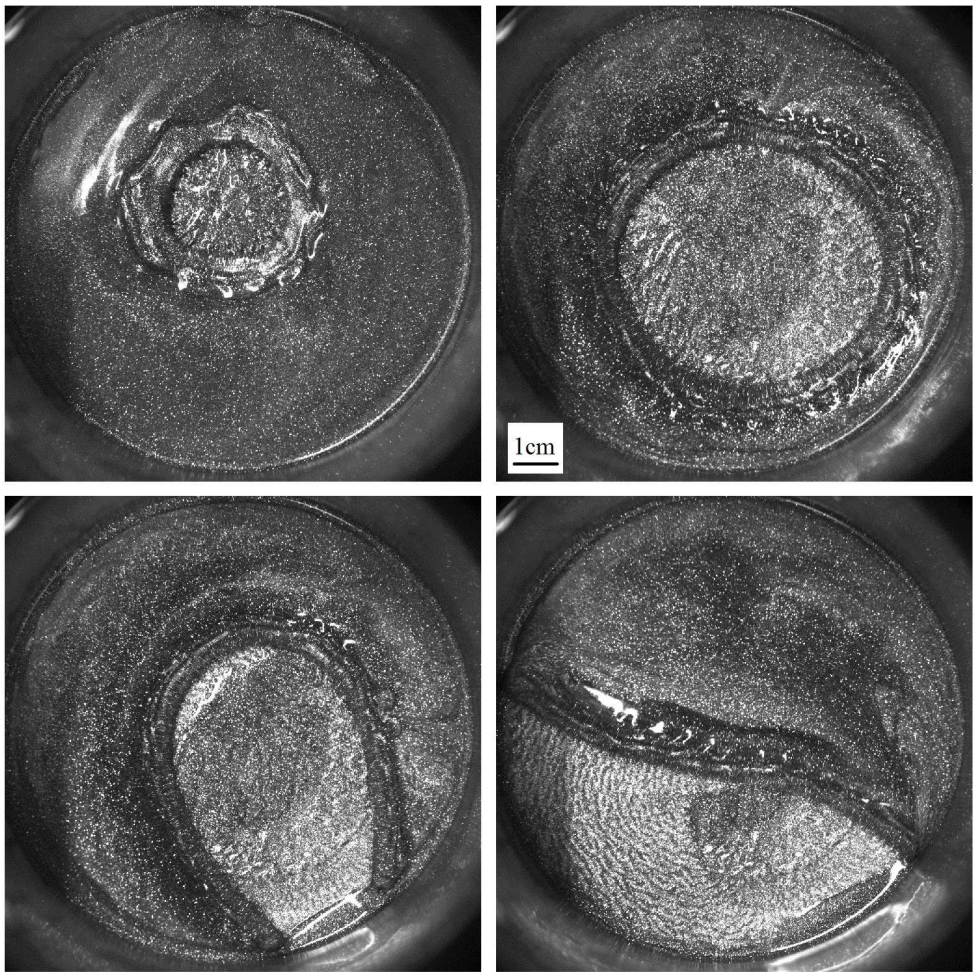


Figure 4.5: Four snapshots of the development of a hole towards a kink in a suspension of glitter particles. The frames go from top left to bottom right and are at $t = 1$, 60, 73 and 92 seconds after the creation of the initial hole ($f = 80$ Hz, $\Gamma = 30$, and $h = 7$ mm.)

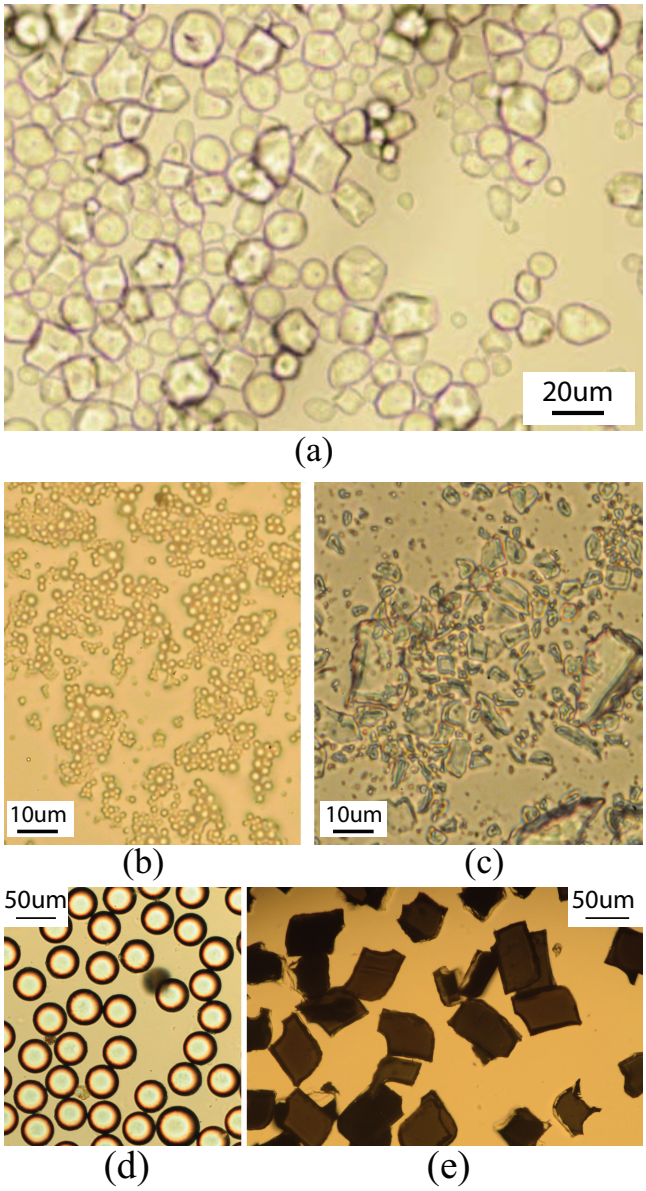


Figure 4.6: Microscopic pictures of the various particles that were used in this study: (a) cornstarch (particle diameter $\sigma = 5 - 20$ $\mu$m); (b) polydisperse glass beads ($\sigma = 0 - 20$ $\mu$m); (c) quartz flour $\sigma = 0 - 70$ $\mu$m; (d) monodisperse polystyrene beads ($\sigma \approx 40$ $\mu$m); (e) a mixture of glitter particles (dimensions $50 \times 50$ $\mu$m$^2$, $50 \times 75$ $\mu$m$^2$, and $50 \times 100$ $\mu$m$^2$ respectively, each with a thickness of 20 $\mu$m).

differences between results in the density-matched and the unmatched liquid, presumably due to the relative violent shaking. In the unmatched suspension only some stirring is required just before the start of a new experiment, to counteract sedimentation. Viewing the cornstarch particles under a microscope, see Fig. 4.6, reveals that they are irregularly shaped and have an approximately flat size distribution in the range of 5-20 $\mu$m.

The first parameter we studied is the packing fraction $\phi$ at a fixed layer depth of $h = 0.6$ cm. For packing fractions up to and including $\phi \approx 0.35$, we find that any perturbation closes due to hydrostatic pressure, as would happen in a Newtonian liquid. At the slightly higher value $\phi = 0.38$ we observe closing holes for low shaking strengths (up to $\Gamma = 25$), indicated by the plus symbols and the white background in the phase diagram of Fig. 4.7(a). At relatively high accelerations ($\Gamma = 40$) and low frequencies (80 Hz) we observe fingerlike shapes emerging from the rim of the disturbance, indicated by the dots and the light grey background. These fingerlike shapes were also reported by Merkt *et al.* [14] for high shaking strengths. At higher frequencies we observe that the created holes are not stable but tend to stretch out and form riverlike structures [the diamonds and dark grey background in Fig. 4.7(a)]. These rivers spread out over the entire width of the container and then become stable. When increasing $\Gamma$ at constant $f$, the edge of the rivers rise up and again form fingerlike structures.

In the phase diagram at intermediate volume fraction, $\phi = 0.40$, we find that the onset of the fingers and rivers regimes shifts to lower shaking strengths [Fig. 4.7(b)]. Below this onset, there now exists an additional narrow window in which stable holes form (represented by circles and medium grey background). That is, increasing the acceleration $\Gamma$ for frequencies around 80 Hz we first observe the formation of stable holes which then give way to fingerlike structures at higher $\Gamma$. When we increase $\Gamma$ at higher frequencies (around 130 Hz), stable holes first turn into rivers which subsequently will produce fingers that will eventually cover the entire surface for the highest values of $\Gamma$.

When increasing the packing fraction even further, to $\phi = 0.42$, the onset of the stable holes regime continues to shift to lower shaking strengths [Fig. 4.7(c)]. In addition, rivers are no longer encountered in the phase diagram: The stable holes always give rise to finger formation when $\Gamma$ is increased. Besides the holes and fingers, there is one additional phenomenon: In the finger regime, when we decrease the frequency at a fixed, high shaking acceleration –i.e., when the amplitude of the shaker is increased– the fingers tend to rise up higher and at a certain point they actually break loose of the surface and form jumping shapes that can live for several thousands of cycles of the driving. This jumping liquid regime is represented by triangles and a dark grey background in the phase diagram.

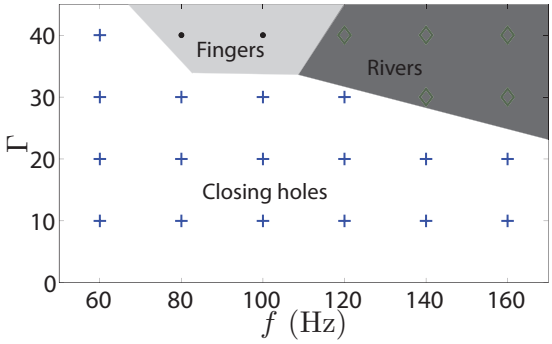


(a)

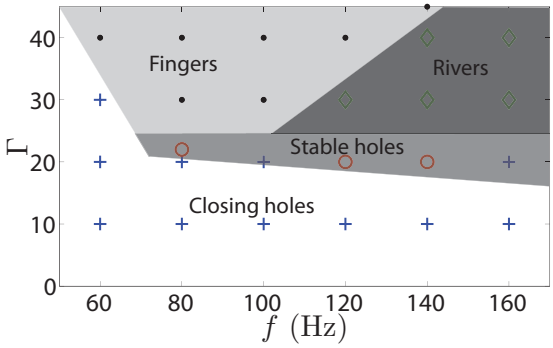


(b)

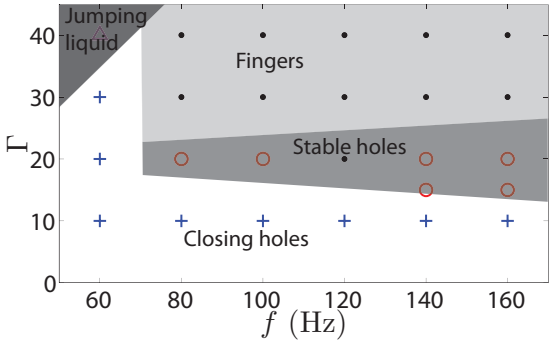


(c)

Figure 4.7: Phase diagrams in the plane spanned by the shaking parameters frequency $f$ and dimensionless acceleration $\Gamma$ for three different cornstarch suspension concentrations $\phi$. From left to right: (a) $\phi = 0.38$; (b) $\phi = 0.40$; and (c) $\phi = 0.42$. In all three diagrams we used a fixed layer depth of $h = 0.6$ cm. The colored areas are added as a guide to the eye and roughly indicate the various regimes in which the phenomena are visible.

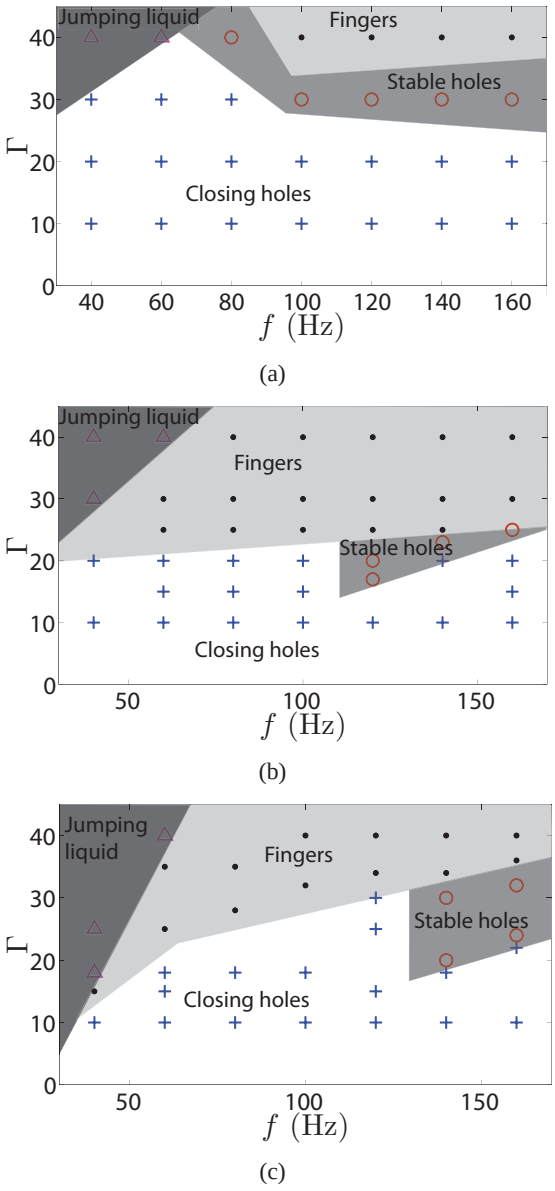


Figure 4.8: Phase diagrams for three different cornstarch layer thicknesses. From left to right: (a) $h = 0.4$ cm, (b) $h = 1.0$ cm, and (c) $h = 1.4$ cm, all at a concentration of $\phi = 0.41$. The colored areas are added as a guide to the eye and roughly indicate the various regimes in which the phenomena are visible.

The second parameter whose influence we will study in detail is the layer depth $h$. To this end we choose a fixed high packing fraction of $\phi = 0.41$, for which the phase diagrams are particularly rich. Since Merkt *et al.* [14] used a fixed layer depth of 0.5 cm, we start at the slightly lower value of $h = 0.4$ cm, and increase the depth to $h = 1.0$ and $h = 1.4$ cm (with the intermediate value of $h = 0.6$ cm covered in Fig. 4.7(b,c) for slightly different values of the concentration $\phi$). The resulting phase diagrams are presented in Fig. 4.8.

In this Figure we see that the types of observed phenomena do not vary with the layer depth, but that the regions in parameters space in which they occur do vary in size and position. First we find that the onset of the phenomena moves down in acceleration $\Gamma$ with increasing layer depth. Secondly we observe that the region in which stable holes are encountered both decreases in size and moves to higher shaking frequencies. In even deeper layers than the ones presented in Fig. 4.8 no stable holes are formed at all. This is most likely due to the fact that hydrostatic pressure becomes more important as the layer depth increases. A stable equilibrium between the effect of the shaking and hydrostatic pressure is then either not possible or happens at such high frequency/acceleration combinations that the regime is not attainable with our experimental setup. The regimes in which fingers and jumping liquid are found increase with layer depth, mainly due to a shift of the onset towards smaller $\Gamma$ for larger $h$. For very large layer depth sometimes it appears that fingers can form while the empty space between the fingers does not reach the bottom.

Finally, we will discuss how the size of the holes in the stable hole regime depends on the various parameters of the system. Note that this task is complicated by the fact that the shape and contours of the stable hole regime depend on these parameters in a rather non-trivial manner (cf. Figs. 4.7 and 4.8). Turning first to the dependence of the time-averaged diameter $\langle d \rangle$ of the hole on the frequency of the driving (Fig. 4.9), we observe a slight decrease in hole size with increasing $f$. This is actually in contradiction with the observations of Merkt *et al.*, who observed an increase in hole size with increasing frequency at a fixed shaking acceleration. The dependence on $f$ however is only small compared to other dependences: The average hole diameter strongly depends on the shaking acceleration (see Fig. 4.10), where a larger acceleration leads to larger holes, when all other parameters are held constant. The increase is such that with an increase of $10g$ the hole can almost double in diameter. In addition, the hole size also strongly depends on the layer depth. In Fig. 4.11 we see that the layer depth $h$ clearly sets the average hole diameter $\langle d \rangle$ as both quantities appear to be proportional to one another. This proportionality is however hard to establish experimentally as a single value for the parameter pair $f$ and $\Gamma$ for which stable holes develop could not be found. We therefore had to use slightly varying parameters ($f = 140$ Hz and $\Gamma = 30$ for the $h = 0.4$ cm experiment, $f = 120$ Hz and

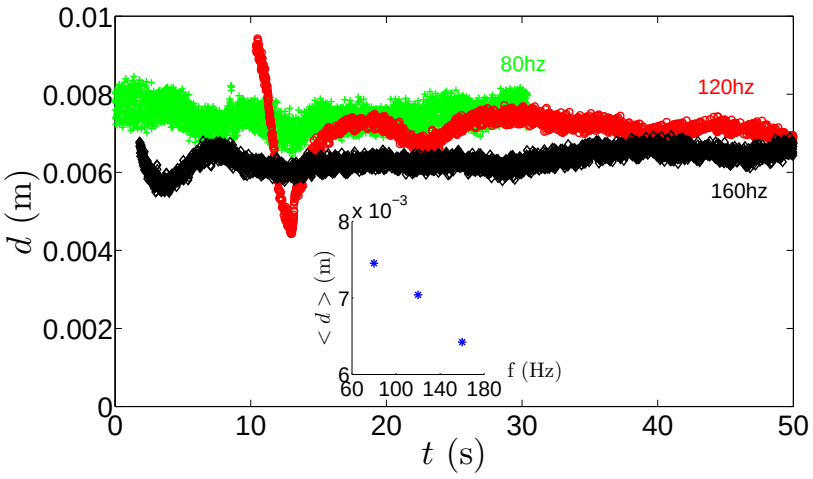


Figure 4.9: Time evolution of the hole diameter $d$ for three different values of the frequency ($f = 80$, 120, 160 Hz) for $\Gamma = 20$ and $h = 0.6$ cm. The inset shows the time-averaged diameter $\langle d \rangle$ as a function of the frequency $f$.

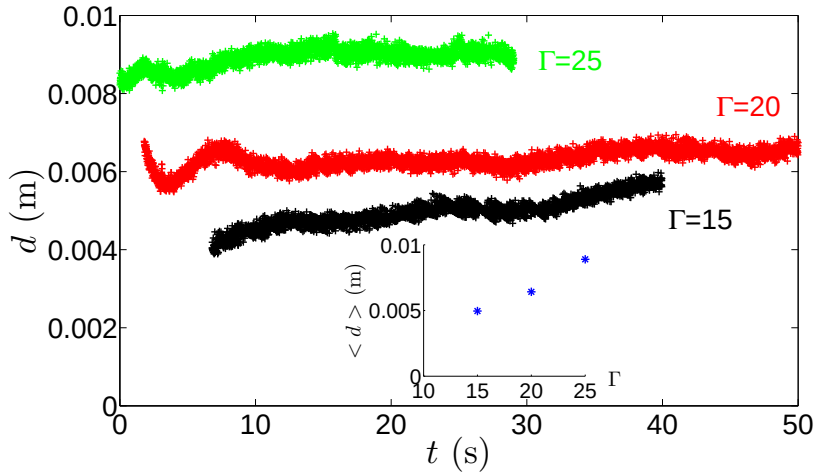


Figure 4.10: Time evolution of the hole diameter $d$ for three different values of the shaking acceleration $\Gamma = 15$, 20, 25, for $f = 160$ Hz and $h = 0.6$ cm. The inset shows $\langle d \rangle$ as a function of $\Gamma$.

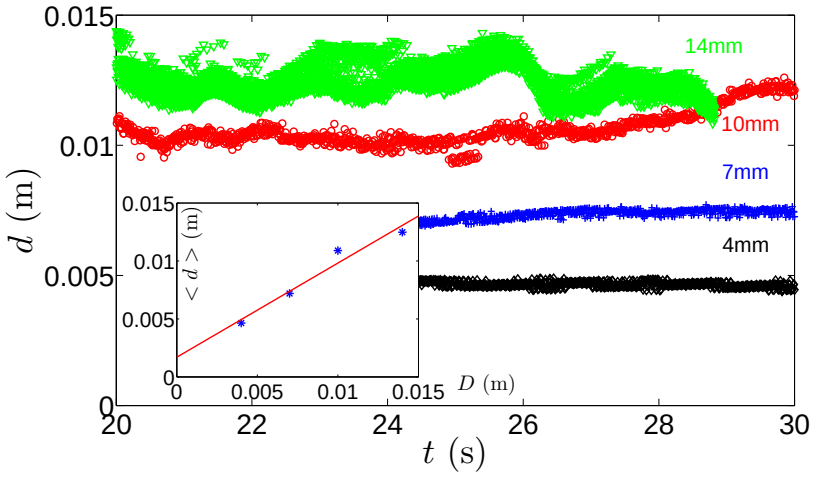


Figure 4.11: Time evolution of the hole diameter $d$ for four different values of the layer depth ($h = 4$, 7, 10, 14 mm). As there was no single choice of parameters $\Gamma$ and $f$ for which stable holes were found for all $h$, these values vary from experiment to experiment (see main text). The inset shows $\langle d \rangle$ as a function of $h$, together with a linear best fit.

$\Gamma = 20$ for both the $h = 0.7$ and the $h = 1.0$ cm experiments, and $f = 160$ Hz and $\Gamma = 24$ for the $h = 1.4$ cm experiment). This slight variation in shaking parameters might explain why the points do not fall onto a single line through the origin.

Finally, the concentration does not appear to influence the hole size. It should, however, be stated that the range in which we can vary the packing fraction $\phi$ and observe stable holes is not very large compared to the variation we can apply in the other parameters (cf. Fig. 4.7).

Cornstarch consist of edgy particles, i.e., they more resemble polygons than spheres, that have an aspect ratio close to one and a flat size distribution with diameters between 5 and 20 $\mu$m, with which we mean that particles of different sizes come in roughly equal numbers. Unfortunately, apart from cornstarch and other similar starches, it is hard to find particles made of a different material and roughly the same geometrical properties. In the remainder of this Section we therefore study the behavior of several other particle suspensions, the particles of which all differ in certain aspects from cornstarch, and compare it to the behavior of cornstarch suspensions.

### 4.4.2 Polydisperse glass beads

The first alternative suspension we turned to are polydisperse glass beads in various size distributions. The beads are spherical and have a density of $2.5 \cdot 10^3$ kg/m$^3$. Due to the large density contrast with water, density matching with sodiumpolytungstate is required. Initially, we used beads in the same size range as cornstarch, 0-20 $\mu$m, of which a microscopic picture can be found in Fig. 4.6(b). From this picture it becomes immediately clear that there are much more small particles than large ones, and therefore the distribution is not flat like that of cornstarch, but the smaller sizes heavily dominate in numbers.

When performing the shaking experiment we observe that after creating an initial disturbance, the hole immediately starts splitting up and colliding with other holes. This splitting and colliding cycle repeats itself every few seconds, leading to a very chaotic dynamics of which a snapshot was shown in the previous Section (Fig. 4.4). Next to the closing holes, this is found to be the only observable phenomenon in this type of suspension. The speed with which the holes split and collide depends on the shaking acceleration and the onset varies with the shaking frequency. A phase diagram of the behavior of the polydisperse glass beads suspension as a function of shaking acceleration $\Gamma$ and frequency $f$ is provided in Fig. 4.12.

Polydisperse glass beads of other size distributions, namely $0-50$ $\mu$m and $40-70$ $\mu$m qualitatively have the same behavior. Varying the layer depth and the packing fraction also do not lead to different behavior or different phenomena.

As an alternative to the overwhelmingly large number of small particles present in the above samples, we used a sample with a more moderate polydispersity consisting of spherical glass beads with sizes between $20-30$ $\mu$m and a more flat size distribution. Again, only splitting and closing holes are observed. The big difference with the previous samples is that it now takes up to a minute for a hole to start splitting. This is a lot longer than for the more polydisperse particles for which this only takes seconds.

### 4.4.3 Quartz flour

The second alternative to cornstarch is quartz flour, which consist of crushed quartz crystals and of which a microscopic picture can be found in Fig. 4.6(c) The size distribution, which ranges from $0-70$ $\mu$m, is similar to that of the polydisperse beads mentioned above, i.e., non-flat with a very large number fraction of small particles. However, the edgy particle shape is more comparable to that of the cornstarch particles. Its density is $\approx 2.5 \cdot 10^3$ kg/m$^3$ and the liquid used to create a suspension is again water, density matched with sodiumpolytungstate.

The phase diagram of a vertically vibrated quartz flower suspension (not shown)

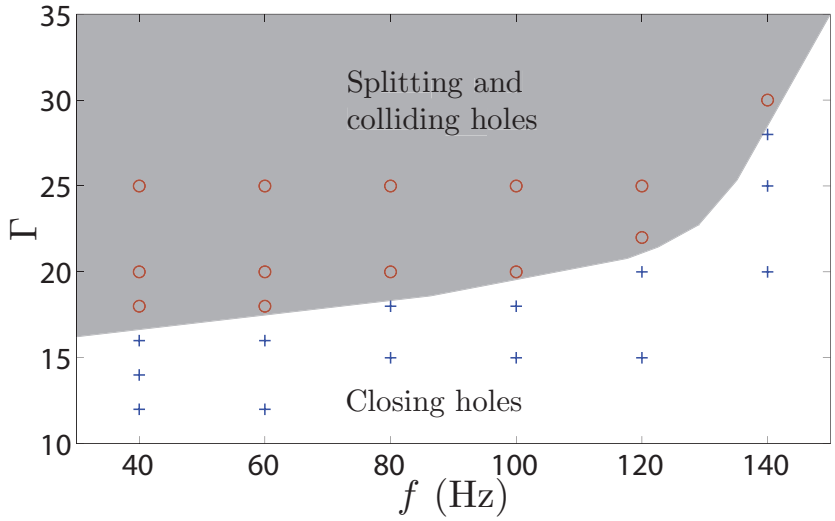


Figure 4.12: Phase diagram in the ($f$,Γ)-plane for polydisperse glass beads with a non-flat size distribution from 0 to 20 $\mu$m. The concentration was $\phi = 0.6$ and the layer depth was fixed to $h = 0.7$ cm. The grey area is added as a guide to the eye and indicates the region where holes grow and duplicate, moving to a disordered state.

is very similar to that of polydisperse glass beads: We find two possible states, namely closing holes for low shaking accelerations and splitting holes at high values of Γ.

For both polydisperse particles, quartz flower and glass beads, filtering was attempted to reduce the surplus of small particles. We attempted several rounds of filtering, either by sieving or selective sedimentation, but it was not possible to remove the small particles to a satisfying extent, and the experimental results did not qualitatively change.

### 4.4.4 Monodisperse beads

In the previous subsection it became clear that the chaotic behavior of the polydisperse glass beads in the splitting hole state could be tempered by reducing the polydispersity of the material. It is therefore interesting to study monodisperse glass beads, which unfortunately are hard to obtain in the necessary quantities. We therefore used polystyrene beads of 20, 40 or 80 $\pm$ 5 $\mu$m (MicroBeads, TS 20-40-80), of which a microscopic picture can be found in Fig. 4.6(d). The particles have a density of 1050 kg/m$^3$ and are mixed with water to create a suspension. Due to the small density difference density matching was not necessary.

Again, for low values of Γ we find closing holes for all examined values of $f$.

Beyond a frequency-dependent onset acceleration, we observe that the initial perturbation turns into a circular hole which grows in time without losing its circular shape. Subsequently, depending on the suspension details and the shaking parameters, the hole will either collapse due to the formation of a rising rim which grows in size while the hole is growing, or will continue to grow until it reaches the container wall and form a kink. The intricate dynamics of the hole growth will be treated in a separate chapter.

### 4.4.5 Glitter

To combine monodispersity with a certain edginess of the particles, we finally employ glitter particles (Sigmund-Lindner, SiliGlit, Polyester Glitter, GradeII). These particles predominantly consist of polyethylene, which are edgy, and have a density of $1.38 \cdot 10^3$ kg/m$^3$. These particles –which incidentally are obtained by cutting of sheet material and mainly intended for use in the cosmetic industry– are available in squares, rectangles, and octagons and are relatively thin (20 $\mu$m) compared to the other dimensions ($50 - 100$ $\mu$m) and quite monodisperse. The particles are hydrophobic, so an apolar liquid needs to be used to create a suspension for which we took sunflower oil. A microscopic picture of a mixture of some of the glitter particles can be found in Fig. 4.6(e).

We have produced various different suspensions, either with a single size of particles, or a mixture of particles and in different concentrations, and the results were found to be qualitatively the same: A disturbance grows and eventually form a large kink covering part of the container surface. Snapshots of such a series of events had been provided in Fig. 4.5 and a typical phase diagram with the crossover between closing and growing holes can be found in Fig. 4.13. A phase diagram for earlier mentioned monodisperse particles would qualitatively show the same results.

The edge of the kink clearly shows a convection roll, which can be observed without adding tracer particles. The size of the roll and the surface area covered by the kink respectively grow and shrink with increasing shaking acceleration. It appears that a higher kink is held in place by a larger convection roll, consistent with the findings of Falcón *et al*. [18].

Very similar phenomena to the ones described here for the monodisperse polystyrene and the glitter particles have been observed in other suspensions of monodisperse beads [16] and even in vibrated emulsions [18]. In the latter, also stable holes and a delocalized state were found, like in cornstarch suspensions.

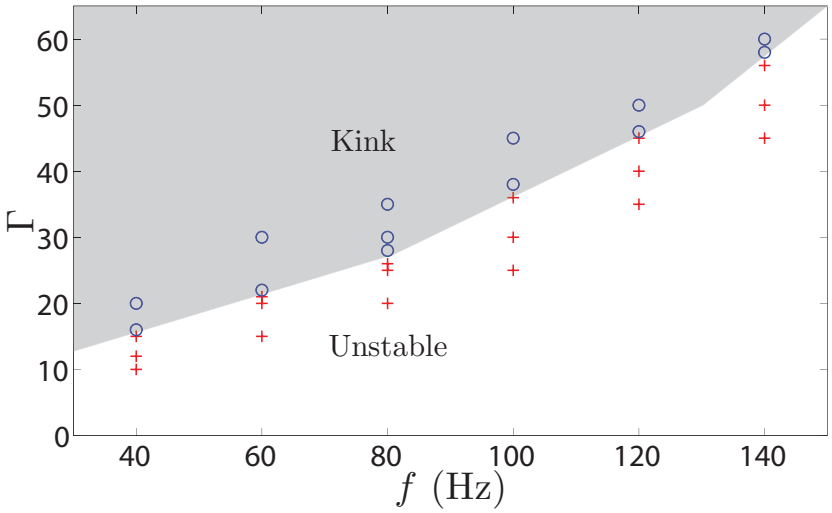


Figure 4.13: Phase diagram in the ($f$,$\Gamma$)-plane for a mixture of glitter particles of dimensions $50 \times 50 \times 20$, $50 \times 75 \times 20$, and $50 \times 100 \times 20$ $\mu$m$^3$. The concentration was $\phi = 0.6$ and the layer depth was fixed to $h = 0.6$ cm. The grey area is added as a guide to the eye and indicates the region where growing holes grow and kinks are found.

## 4.5 Discussion and conclusions

In the previous Sections we have mostly focused on the differences between the various particulate suspensions we have studied. We therefore want to start this concluding Section by recapitalizing the similarities of which there are quite a few:

- Like every other liquid, suspensions that are vertically vibrated in a container will develop a pattern of surface waves above a certain threshold, the famous Faraday waves [19]. The details of this pattern depend on the frequency and amplitude of the shaking. We have observed these patterns on all suspensions, with the expected period doubling corresponding to half the driving frequency. We also established that the presence of Faraday waves did not significantly interfere with the phenomena discussed in this article.

- Besides the Faraday waves, all presented phenomena require an initial perturbation to be 'initiated'.

- All presented phenomena overcome hydrostatic pressure: When a hole is created in a Newtonian liquid, gravity will push the liquid back and close the opening. Since in all presented experiments, the holes remain visible for very long times or even grow, the interplay of the suspension properties and the (symmetric) driving works against gravity.

- In all cases particularly dense suspensions are needed. Suspensions with lower particle concentrations behave similar to Newtonian liquids and only present closing holes.

- For all patterns that are described in this study, the edges in the suspension (e.g., the rim of the holes) oscillate with the same frequency as that of the driving, with a phase shift. The same is true for a Newtonian liquid, where the rim of the hole, while closing, is also oscillating.

- Many of the suspensions we used appear to be very viscous when at rest, and to flow more easily when shaken. This presumably is a signature of the shear thinning properties that many dense suspensions are reported to have at moderate shear rates [2–6].

In conclusion, in this chapter we have been extensively studying the behavior of various vertically vibrating dense suspensions with different particle sizes, shapes, compositions, and distributions. All of these suspensions have in common that there are Faraday waves above a certain threshold and that when a perturbation is created at low shaking strengths and/or low particle concentrations we observe the formation

of a closing hole with oscillating edges, just like what would happen in a viscous Newtonian liquid. However, after an initial perturbation is created in a dense suspension at high shaking strengths we observe a rich variety of phenomena that all overcome hydrostatic pressure. Of all suspensions examined, the cornstarch suspensions present the largest number of different phenomena, which include stable holes, rivers, fingers, and jumping liquid. Moreover, all of these turn out to be unique to cornstarch, since –at least in this study– they have not been observed in the other suspensions.

The other suspensions studied –polydisperse glass beads, polydisperse quartz flower, monodisperse spherical particles, and monodisperse glitter particles– presented two types of patterns, namely growing holes, which ultimately develop into kinks, and splitting holes, which split, collide, and merge in a chaotic dynamics. The pattern that is selected is found to be connected to the distribution of particle sizes: Suspensions of monodisperse particle lead to growing holes, whereas suspensions containing a polydisperse particle distribution lead to splitting holes.

It is particularly intriguing that cornstarch suspensions behave so differently compared to the other suspensions. This either suggests that this behavior is typical for monodisperse, edgy particles of the size of cornstarch ($\approx 20\ \mu$m) –for which no alternative made of a different, preferably inorganic, material had been found so far– or that some other undisclosed property of cornstarch is at play. Finally, all of the observed phenomena are worthy of a thorough theoretical investigation of their origin, but such an endeavor goes beyond the scope of the current work.

## References

[1] N. Wagner and J. Brady, “Shear thickening in colloidal dispersions”, Phys. Today **62**, 27 (2009).

[2] H. Barnes, “Shear-thickening (dilatancy) in suspensions of nonaggregating solid particles dispersed in newtonian liquids”, J. Rheol **33**, 329 (1989).

[3] A. Fall, N. Huang, F. Bertrand, G. Ovarlez, and D. Bonn, “Shear thickening of cornstarch suspensions as a reentrant jamming transition”, Phys. Rev. Lett. **100**, 018301 (2008).

[4] E. Brown and H. Jaeger, “Dynamic jamming point for shear thickening suspensions”, Phys. Rev. Lett. **103**, 086001 (2009).

[5] E. Brown, N. Forman, C. Orellana, H. Zhang, B. Maynor, D. Betts, J.M.DeSimone, and H. Jaeger, “Generality of shear thickening in suspensions”, Nat. Mater. **9**, 220 (2010).

[6] C. Bonnoit, T. Darnige, E. Clement, and A. Lindner, "Inclined plane rheometry of a dense granular suspension", J. Rheol. **54**, 65 (2010).

[7] M. van Hecke, "Running on cornflour", Nature **487**, 174 (2012).

[8] S. Waitukaitis and H. Jaeger, "Impact-activated solidification of dense suspensions via dynamic jamming fronts", Nature **487**, 205–209 (2012).

[9] A. Fall, F. Bertrand, G. Ovarlez, and D. Bonn, "Shear thickening of cornstarch suspensions", .

[10] C. Bonnoit, J. Lanuza, A. Lindner, and E. Clement, "Mesoscopic length scale controls the rheology of dense suspensions", Phys. Rev. Lett. **105**, 108302 (2010).

[11] E. B. White, M. Chellamuthu, and J. Rothstein, "Extensional rheology of a shear-thickening cornstarch and water suspension", Rheol. Acta **49**, 119–129 (2010).

[12] S. von Kann, J. Snoeijer, D. Lohse, and D. van der Meer, "Nonmonotonic settling of a sphere in a cornstarch suspension", Phys. Rev. E **84**, 060401 (2011), chapter 2 of this thesis.

[13] B. Liu, M. Shelley, and J. Zhang, "Focused force transmission through an aqueous suspension of granules", Phys. Rev. Lett. **105**, 188301 (2010).

[14] F. Merkt, R. Deegan, D. Goldman, E. Rericha, and H. Swinney, "Persistent holes in a fluid", Phys. Rev. Lett. **92**, 184501 (2004).

[15] R. Deegan, "Stress hysteresis as the cause of persistent holes in particulate suspensions", Phys. Rev. E **81**, 036319 (2010).

[16] H. Ebata, S. Tatsumi, and M. Sano, "Expanding holes driven by convectionlike flow in vibrated dense suspensions", Phys. Rev. E **79**, 066308 (2009).

[17] H. Ebata and M. Sano, "Self-replicating holes in a vertically vibrated dense suspension", Phys. Rev. Lett. **107**, 088301 (2011).

[18] C. Falcón, J. Bruggemann, M. Pasquali, and R. Deegan, "Localized structures in vibrated emulsions", Europhysics Lett. **98**.

[19] M. Faraday, "On a peculiar class of acoustical figures; and on certain forms assumed by groups of particles upon vibrating elastic surfaces", Philosophical Transactions of the Royal Society of London **121**, 299–340 (1831).

# 5

# Hole dynamics in vertically vibrated suspensions *

*We study the dynamics of holes, created in vertically vibrated dense suspensions and viscous Newtonian liquids. We find that all the holes oscillate with the driving frequency, with a phase shift of $\pi/2$. In Newtonian liquids holes always close, while in suspensions holes may grow in time. We present a lubrication model for the closure of holes which is in good agreement with the experiments in Newtonian liquids. The growth rate of growing holes in suspensions is found to scale with the particle diameter over the suspending liquid viscosity. Comparing closing holes in Newtonian liquids to growing holes in dense suspensions we find a sinusoidal, linear response in the first, and a highly non-linear one in the latter. Moreover, the symmetry of the oscillation is broken and is shown to provide an explanation for the observation that holes in dense suspensions can grow.*

*Stefan von Kann, Matthias van de Raa, and Devaraj van der Meer, Hole dynamics in vertically vibrated suspensions, preprint (2012).

## 5.1 Introduction

When a hole is created in a horizontal layer of a (viscous) liquid at rest, the hydrostatic pressure will cause the hole to close. In spite of its more complicated rheology, the same thing is expected to happen in a non-Newtonian liquid. Recently however, the reverse has been shown to occur in experiments where layers of various particulate suspensions and emulsions were subjected to vertical vibrations: Holes created in these vibrated liquids do not necessarily close, but may stabilize [1, 2], grow [3], or lead to chaotic dynamics [4, 5]. Although phenomenological models are suggested in the literature [3, 6] our understanding of this behavior is far from complete. In this chapter we will shed light onto this dynamics by investigating the analogies and differences between vertically vibrated viscous Newtonian fluids and a suspension of monodisperse particles in liquids with the viscosity of water and higher.

A concentrated particulate suspension consists of a mixture of a homogeneous liquid and particles that are large enough ($> 1\mu$m) such that their Brownian motion is negligible. They can be found in many places, ranging from quicksand, through freshly mixed cement and paints to the inside of flexible armor suits. Their flow is important in nature, industry and even health care [7]. In spite of their common presence and significance, many aspects of the flow of these dense suspensions remain poorly understood. In order to study these materials people have used methods inspired by classical rheology, and typically characterized them in terms of a constitutive relation of stress versus shear rate [8–13]. A general result is that, when increasing the shear rate, dense suspensions first tend to become less viscous (shear thinning) and subsequently shear thicken. In recent experiments people found mesoscopic length scales [12, 14], fracturing [15], and a dynamic jamming point [10] to be important in such suspensions. Connected to the above, normal stress divergence in the approach to a wall [16], and non-monotonic settling [17] have been reported for objects moving through dense cornstarch suspensions.

Turning to vertically vibrated suspensions, Merkt *et al.* [1] observed in a vertically shaken, thin layer of cornstarch suspension that –amongst other quite exotic phenomena– stable oscillating holes can be formed for certain values of the shaking parameters. These stable holes were subsequently described using a phenomenological model based on a hysteretic constitutive equation [6]. In other particulate suspensions, Ebata *et al.* found growing and splitting holes and a separated state [3, 4], where the latter is attributed to a convective flow in the rim and the first are still not understood. Stable holes and kinks (which appear to be similar to or even identical to the separated state mentioned above) have also been reported in emulsions [2]. At present we are still far from a detailed understanding of dense suspensions, and why different suspension behave differently.

Here, we will investigate the dynamics of opening holes in a layer of vibrated

suspension of monodisperse particles of various sizes suspended in a glycerol-water mixture. We will investigate how this dynamics depends on particle size and viscosity and compare it to the dynamics of closing holes in a layer of vertically shaken viscous liquids, for which we will present a model within the lubrication approximation. We will then shed light upon how the differences arise and in what manner these can explain the observation that the holes in the suspension do not close as a result of hydrostatic pressure.

The chapter is organized as follows: We will start with a short description of our setup in Section 5.2. After this we will present experiments for the dynamics of closing holes in a (vibrated) layer of a viscous Newtonian liquid (Section 5.3.1), followed by the introduction and discussion of a lubrication model for this system (Section 5.3.2). Subsequently, in Section 5.4 we turn to the dynamics of opening holes in vibrated particle suspensions and discuss the similarities and differences with the closing holes. The chapter will be concluded in Section 5.5.

## 5.2 Experimental setup

The experimental setup is shown in Fig. 5.1. Its core consists of a cylindrical container with a diameter $D = 11.0$ cm and a height $H$ of 8.0 cm. This container is vertically vibrated by a shaker (TiraVib 50301) with frequencies $f$ between 20 and 200 Hz and a dimensionless acceleration $\Gamma$ from 0 up to 60. Here, $\Gamma = a(2\pi f)^2/g$, where $a$ is the shaking amplitude and $g$ the gravitational acceleration. The container is filled up to a height $h_0 = 6 \pm 1$ mm with a viscous liquid or a suspension of varying composition. The dynamics of the fluid layer in the container is recorded with a high speed camera at various frame rates, given in frames per second (fps), and is imaged from the top. The bottom of the container was covered with tape for improved contrast between liquid and container bottom. When using transparent liquids, a small amount of powdered milk was added to whiten the liquid. Of course it was checked that adding tape or milk powder did not influence the dynamics of the system.

## 5.3 Viscous Newtonian liquids

Before turning to the –anomalous– opening holes in dense suspensions consisting of monodisperse particles in a mixture of glycerine and water, we will first study the regular case of holes closing in a viscous Newtonian liquid. We will both discuss the case where the holes close purely due to the hydrostatic pressure in the liquid and the case in which a periodic forcing is added by vibrating the system vertically. In the second subsection we will subsequently present a model to describe both cases.

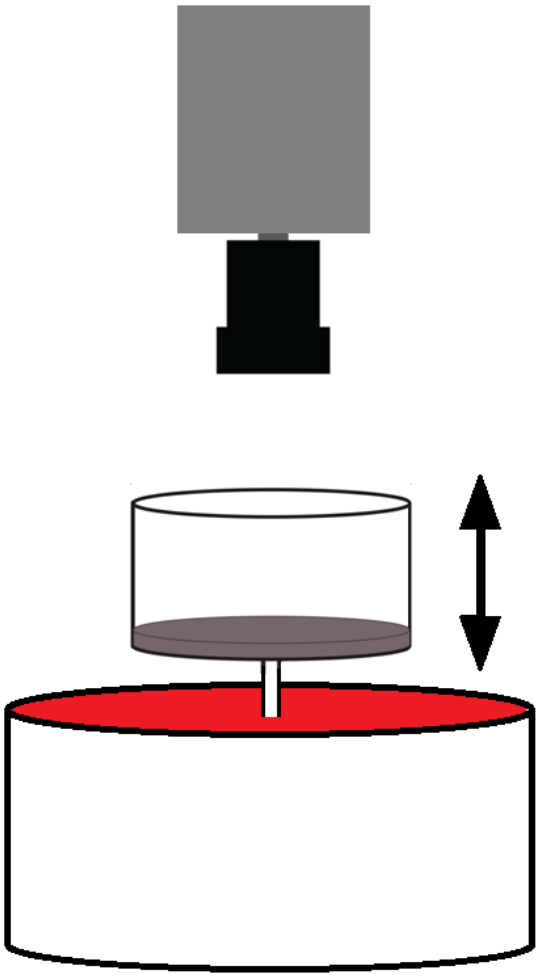

Figure 5.1: A schematic view of the used setup. At the lower end we have the shaker, on top of which the container with the suspension is mounted, which is subsequently vibrated vertically. Above that is the high speed camera, recording the suspension from above.

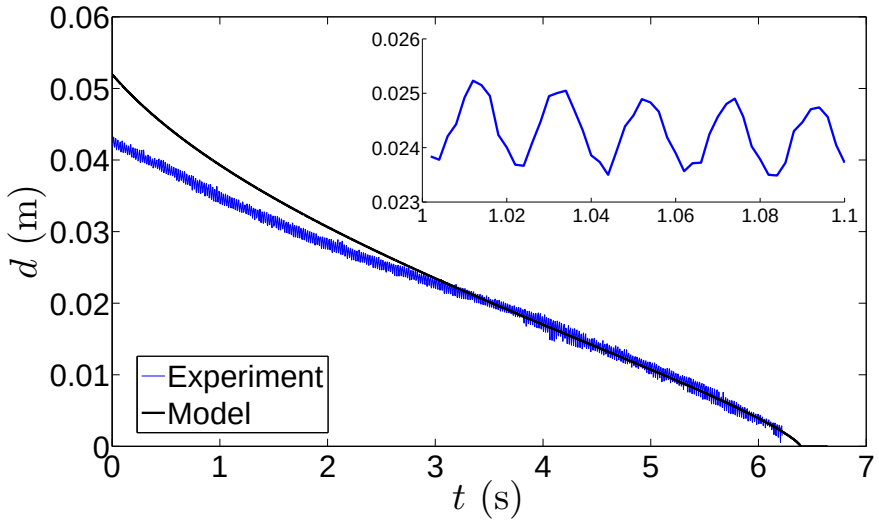


Figure 5.2: The diameter of a closing hole in a layer of honey ($\mu = 6.4$ Pa·s) with a thickness of $h_0 = 6 \pm 1$ mm as a function of time, while the layer is vertically vibrated at $f = 50$ Hz, $\Gamma = 30$ and recorded at a framerate of 250 fps (blue line). The black line is the result of a calculation using the lubrication model. The inset is from an experiment using the same shaking parameters, but twice the recording speed (500 fps).

### 5.3.1 Experiment

We prepare a layer with a thickness of $h_0 = 6 \pm 1$ mm of a viscous liquid in the container as described in the previous Section. Subsequently, a disturbance is created into the layer by blowing air from the top until a more or less circular hole with a diameter of a few centimeters is formed. To vary the viscosity of the liquid we choose honey, with a dynamic viscosity of $\mu = 6.4$ Pa·s, and several glycerine-water mixtures with viscosities of $\mu = 1.3$, 1.1, 0.45, and 0.15 Pa·s. Viscosities below the last value lead to holes that close extremely fast; in particular they were found to close within a single cycle of the lowest driving frequency we have used in our study ($f = 20$ Hz). Moreover, for these low viscosities inertial effects will start to become important and therefore such fluids were not considered here.

Fig. 5.2 provides a typical experimental result for a $h_0 = 6$ mm thick layer of honey, vibrated at $f = 50$ Hz, $\Gamma = 30$. After creating a circular hole in the layer, we follow the dynamics of its closing and plot the hole diameter as a function of time. Over the course of several seconds the hole closes almost linearly. At the same time the hole oscillates at the same frequency as the driving, which is shown in the inset

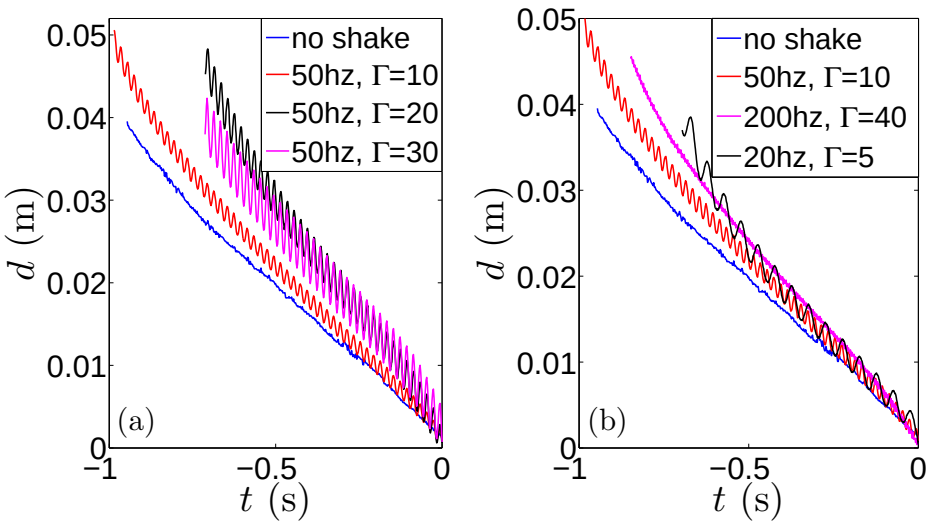


Figure 5.3: Time evolution of the hole diameter in a vertically vibrated layer of glycerine ($\mu = 1.3$ Pa·s and $h_0 = 6$ mm): (a) For a constant shaking frequency $f = 50$ Hz and different values of the shaking acceleration $\Gamma = 0$ (no shaking, blue line), $\Gamma = 10$ (red line), $\Gamma = 20$ (magenta line), and $\Gamma = 30$ (black line). (b) The same, but now for varying frequencies: $f = 0$ Hz, $\Gamma = 0$ [no shaking, blue line, as in (a)]; $f = 20$ Hz, $\Gamma = 5$ (black line); $f = 50$ Hz, $\Gamma = 10$ [red line, as in (a)]; and $f = 200$ Hz, $\Gamma = 40$ (magenta line).

where part of the signal has been magnified in time.

When changing the shaking parameters $f$ and $\Gamma$, it becomes clear that the closing time is to a large extent independent of $f$ and $\Gamma$, as is shown in Fig. 5.3 where we show results obtained in glycerine. In particular, when we do not shake at all and just create a hole in the container at rest and observe its closing due to gravity, we find that its time evolution follows the very same trend. The amplitude of the oscillation increases more or less linearly with the shaking acceleration $\Gamma$ and is in fact of the same order as the shaking amplitude $a = \Gamma g/(2\pi f)^2$. The latter observation also explains why the amplitude of the oscillation decreases so much when the frequency is raised to $f = 200$ Hz, which causes the shaking amplitude to go down by a factor 16. Moreover, the amplitude of the oscillations of the edge of the hole appear to be independent of the hole size, i.e., the amplitude remains largely constant while the hole diameter shrinks down to zero.

In Fig. 5.4 we compare results for the different liquid viscosities, shaken at $f = 50$ Hz and $\Gamma = 10$. For the lowest viscosity ($\mu = 0.15$ Pa·s) we observe that the

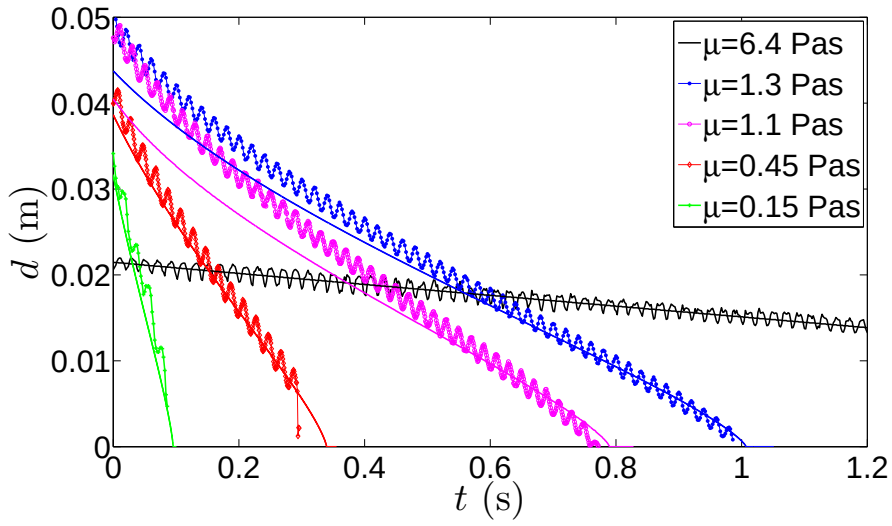


Figure 5.4: Time evolution of the hole diameter in a $h_0 = 6$ mm thick layer of liquid of varying viscosity $\mu$, vibrated at $f = 50$ Hz and $\Gamma = 10$. The solid (not oscillating) lines denote the time evolution according to the model discussed in Section 5.3.2.

holes closes in less than a tenth of a second, i.e., within a few cycles of the driving. When we increase the viscosity the closing time increases rapidly, and for the highest viscosity (that of honey, $\mu = 6.4$ Pa·s) the closing time is over six seconds.

In the same Figure we observe that there is a significant span of time in which the average closure velocity appears to be linear. This allows us to correct the signal by subtracting this linear behavior and afterwards compare it to the vertical position of the container. This is done in Fig. 5.5, where we zoom in on a few cycles only. There is a clear phase shift between the driving and the hole, which is measured to be approximately a quarter of a period, as shown in the inset of Fig. 5.5. The fact that the horizontal oscillation of the hole lags behind $\Delta\psi = \pi/2$ with the vertical container position implies that the oscillating velocity of the hole is in phase with the latter. This in turn implies that the velocity with which the hole oscillates is in antiphase with the shaking acceleration. Note that this implies that the acceleration of the liquid layer is in phase with the velocity of the hole, i.e., the hole closes for downward and opens for upward acceleration of the layer.

To quantitatively compute the average velocity profile in a cycle we start from the corrected signal and shift all cycles on top of each other, as seen in Fig. 5.6(a). We then compute the average diameter and the average velocity [Fig. 5.6(b)]. We conclude that both are nicely sinusoidal. Most importantly the positive and negative

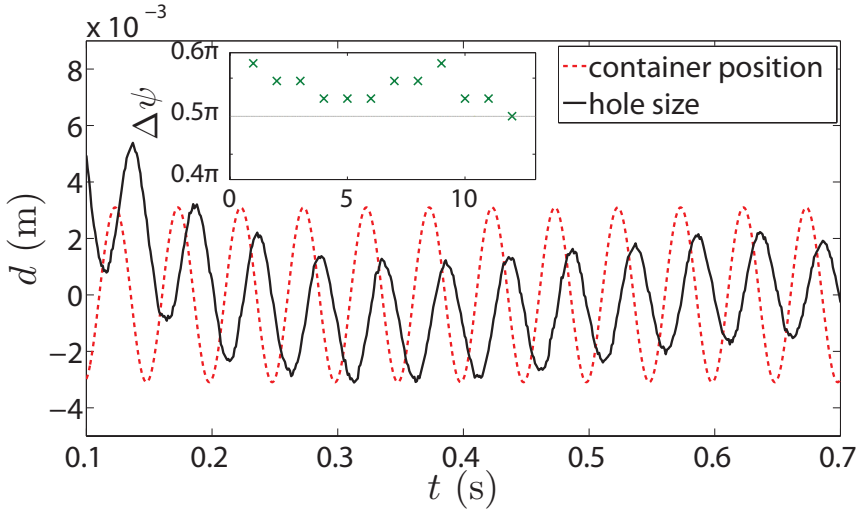


Figure 5.5: Comparison of a sine fit of the trajectory of the vertical position of the container (vibrated at $f = 20$ Hz and $\Gamma = 5$; dotted line), and the trajectory of the diameter of a closing hole in a $h_0 = 6$ mm layer of glycerine ($\mu = 1.3$ Pa·s), corrected for the (linear) closing velocity (see text; solid line). The inset shows the phase difference $\Delta\psi$ for every period shown in the main Figure.

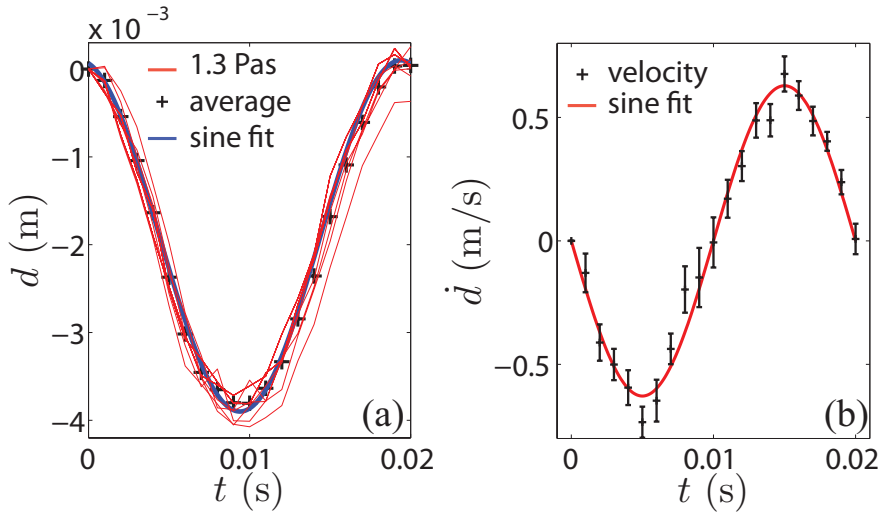


Figure 5.6: (a) Superposition of several cycles of the corrected trajectory of the diameter of a closing hole shifted over an integer number of periods of the driving. The black plus symbols indicate the average position and the blue line is a sinusoidal fit to the average. (b) The instantaneous velocity of the closing hole averaged over all cycles. The solid line shows the derivative of the sine fit of (a). Taken from an experiment with glycerine ($\mu = 1.3$ Pa·s, $h_0 = 6$ mm, $f = 50$ Hz, $\Gamma = 20$).

half of each cycle are close to each others mirror images and follow the shape of the driving signal very well.

Now what is happening physically? First one should realize that the magnitude of the shaking acceleration that we subject our liquid layers to is many times that of gravity. This means that the liquid layer is alternately subjected to a large downwards acceleration, that is forcing the hole to close –as gravity does– in one half of the driving period, and an almost equally large upwards acceleration in the other half. Clearly, in this stage the liquid strives to move upward with respect to the container, and therewith opens the hole again. It is the small unbalance between the upward and the downward acceleration caused by gravity that makes the hole close in the long run[†].

[†]Of course, when the direction of the acceleration is upward, the fluid surface becomes potentially unstable, which one could call a Rayleigh-Taylor, Richtmyer-Meshkov, or Faraday instability, depending on the perspective and the specific timescale one is looking at. This instability is counteracted by surface tension (which stabilizes the smaller wavelengths) and liquid viscosity. From the experiment we infer that for the liquids in this study this leads to stable standing wave patterns (the Faraday waves) in the worst case.

### 5.3.2 Modeling

To model the dynamics of closing holes in a viscous Newtonian liquid we use axisymmetric lubrication theory. In absence of the driving, the equation of motion for the liquid profile $h(r,t)$ can be derived from continuity and a lubrication ansatz for the velocity profile within the layer (See Section 5.6 [‡]).

$$\frac{\partial h}{\partial t} = \frac{\rho g}{3\mu r}\frac{\partial}{\partial r}\left[rh^3\frac{\partial h}{\partial r}\right], \tag{5.1}$$

where $r$ is the radial coordinate, $g$ the acceleration of gravity, $\rho$ the density, and $\mu$ the dynamic viscosity of the liquid. Using lubrication theory implies neglecting inertial effects. In particular this means that the scaling behavior of the closing velocity can be derived from an (instantaneous) balance of the gravitational force which drives the closing and the viscous forces that counteract it, i.e.

$$\rho g \sim \mu\frac{\dot{d}}{h_0^2} \quad \Rightarrow \quad \dot{d} \sim \frac{\rho g h_0^2}{\mu}, \tag{5.2}$$

in which $\dot{d}$ denotes the time derivative of the hole diameter and we have estimated the viscous forces in the layer, $\mu\,(\partial^2 u/\partial z^2)$ as the velocity of the rim $\dot{d}/2$ divided by the squared initial layer thickness $h_0$. From this simple balance it follows that the closing velocity should scale as $1/\mu$. If we check this for our experimental results by plotting the closing velocity $\dot{d}$ (determined from the linear regime of plots as in Fig. 5.4) as a function of viscosity $\mu$ Fig. 5.7 we find a very good agreement. Remarkable is that the plot does not only contain data without driving, but also with various driving strengths.

When we assume an infinite layer of liquid, we can derive a semi-analytical self-similar solution to the closing hole problem which leads to a hole diameter of the form

$$d(t) = 2\eta_0\sqrt{\frac{\rho g h_0^3}{3\mu}(t_c - t)}\ , \tag{5.3}$$

where $\eta_0$ is a numerical constant and $t_c$ is the time the hole needs to close. In our case these can be thought of as fixed by the initial hole size together with the boundary conditions at the sidewalls of our container. This self-similar solution goes to zero with a square-root dependence on time which is however –maybe with the exception of the very end– not observable in our experiments (Figs. 5.2, 5.3 and 5.4). This is presumably connected to the proximity of the side walls. We therefore decided

[‡]Some technical details in the derivation of several results presented in this Section can be found in Section 5.6.

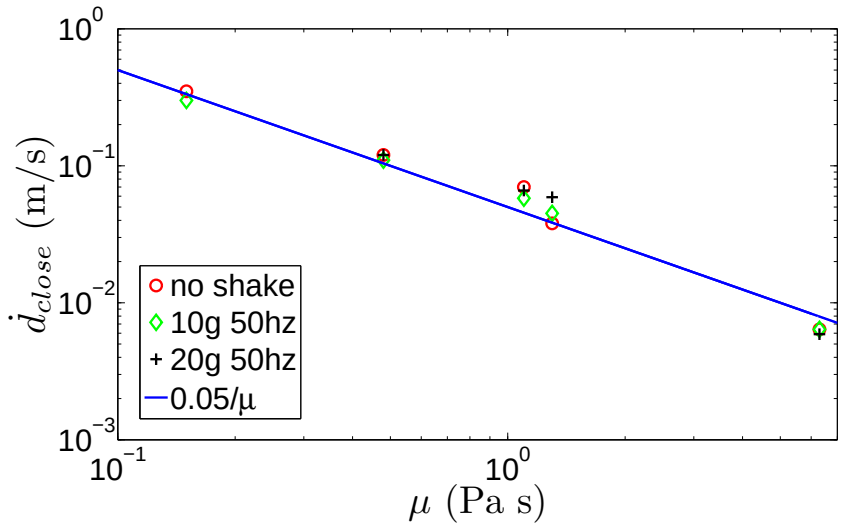


Figure 5.7: Average closing velocity as a function of viscosity in a double logarithmic plot, for three different values for the driving (no shaking; $f = 50$ Hz and $\Gamma = 10$; and $f = 50$ Hz and $\Gamma = 20$. The blue solid line is $\dot{d}_{close} = 0.05/\mu$, making the proportionality constant in Eq. (5.2) equal to 0.12.

to numerically solve Eq. (5.1), supplemented with $\int_0^{D/2} h(r,t)rdr = \text{constant}$, which expresses the conservation of liquid in our system.

In Figs. 5.2 and 5.4 we compare our model results to the experiments and find that behavior is well captured by the model.

We can use Eq. (5.1) to model the modulation due to the acceleration of the shaker as well, by simply substituting $g(1+\Gamma\sin\omega t)$ for $g$, leading to

$$\frac{\partial h}{\partial t} = (1+\Gamma\sin\omega t)\,\frac{\rho g}{3\mu r}\frac{\partial}{\partial r}\left[rh^3\frac{\partial h}{\partial r}\right] \tag{5.4}$$

The result is (at least in first order) the same as for the purely gravitational case, with a continuous oscillation on top of the gravitational result, just like we see in our experiments. More details can be found in Section 5.6.

## 5.4 Non-Newtonian liquids

Whereas disturbances created in a layer of a Newtonian liquid always close, independent of whether the layer is being vibrated or not, for non-Newtonian liquids things are observed to be different. More specifically, for the particulate suspensions studied here [§], holes close when the suspensions are at rest, but may either open or close when vertically vibrated.

### 5.4.1 Experiment

As discussed in Section 5.1, several types of non-closing holes were found in various vibrated suspensions and emulsions, including stable holes, splitting holes, and growing holes [1–6]. It is this last type, the growing holes, which will be the focus of this Section. Growing holes are typically found in suspensions containing monodisperse particles [¶] [1, 2], and splitting holes occur in suspensions of particles with a substantial poydispersity [5]. We therefore use monodisperse, spherical polystyrene particles with a diameter ($\sigma$) of 20, 40, and 80 $\pm$ 5 $\mu$m, and a density of 1050 kg/m$^3$ (MicroBeads, TS 20-40-80). As the suspending liquid we used various glycerine-water mixtures, with varying viscosities and densities. Because the suspending liquid may be either denser or less dense than the particles, we do not attempt to density match the liquid. In all cases the time scale at which the suspension separates is much larger than the time scales of the experiment. In some cases we have checked that our results did not depend on whether the liquid density would be larger or smaller than that of the particles by adding Cesium Chloride to the suspending liquid. Much care has been taken to ensure that the packing fraction $\phi$ –the volume occupied by the solid phase in the suspension divided by the total volume– was kept at a constant value of 0.52.

In Fig. 5.8 we show the typical time evolution of the hole diameter for a growing hole, here in a suspension consisting of the $\sigma = 40$ $\mu$m particles and glycerol-water mixtures of three different viscosities. We observe that a lower viscosity causes holes to open faster. This appears to be comparable to the Newtonian liquids, where holes also close faster for lower viscosity, but one needs to be careful in making this comparison: First of all, the viscosity of the suspending liquid is generally not comparable to the (non-constant) viscosity of the suspension as a whole, since there is a usually non-negligible or even dominant contribution from the particle phase. Secondly, we are now looking at the rate at which the hole grows *against both* gravity and the sus-

[§] As a yield stress has been reported in some very dense suspensions, it is conceivable that gravity is not capable of overcoming this yield strength when such a material is at rest. In the suspensions studied here, this is not the case.

[¶] Stable holes have been observed in cornstarch suspensions and some emulsions

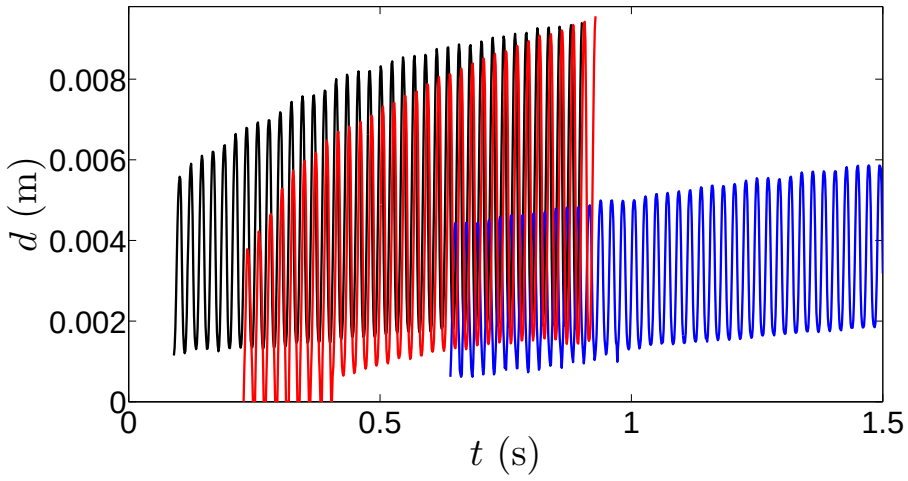


Figure 5.8: Time evolution of the diameter $d$ of a growing hole in a suspension of 40 $\mu$m polystyrene particles in glycerine-water mixtures of three different viscosities, namely $\mu = 0.14$ Pa·s (red line), $\mu = 0.22$ Pa·s (black line), and $\mu = 0.52$ Pa·s (blue line) versus time for three opening holes in a 52% volume fraction suspensions, shaken at $\Gamma = 28$ and $f = 45$Hz.

pension viscosity, whereas for the closing holes in a Newtonian liquid gravity was the driving force of the closure.

The trend mentioned above holds for all experiments we performed. Noteworthy is that for the higher suspending liquid viscosities and larger particles we typically observe growth of the hole until it develops a kink (where part of the system, including part of the wall, falls dry separated by a kink from the suspension) whereas for small values of the suspending liquid viscosity and large particles we also observed holes that would go through many consecutive cycles of growth followed by a rapid collapse to an almost zero radius.

To further quantify the dependence of the growth rate on the suspending liquid viscosity, we determined the average growth $\Delta d$ of the hole diameter per cycle and plotted it against the suspending liquid viscosity $\mu$ in Fig. 5.9(a) for all three bead sizes. We observe that all three data sets show a clear decrease of $\Delta d$ with increasing $\mu$, confirming our observation that the growth rate decreases with increasing suspending liquid viscosity. The data however does not collapse onto a single curve. Therefore, in Fig. 5.9(b) we plot the same data as a function of $\mu/\sigma$ which leads to a reasonable collapse of the data for the two larger sizes, the significance of which will

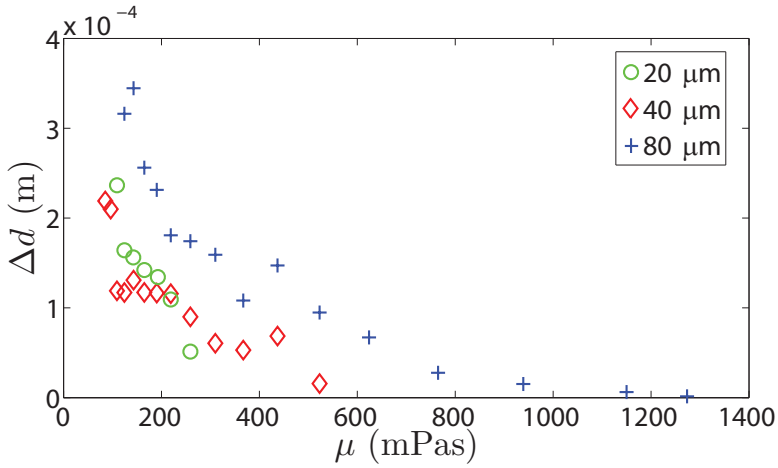


(a)

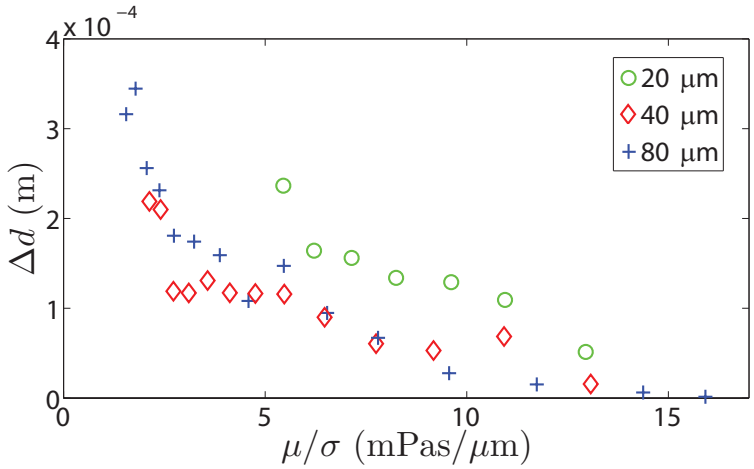


(b)

Figure 5.9: (a) The average growth $\Delta d$ per cycle of a growing hole as a function of the suspending liquid viscosity $\mu$. The experiments were done for suspensions of all three bead diameters, $\sigma = 20$ $\mu$m (green circles), $\sigma = 40$ $\mu$m (red diamonds), and $\sigma = 80$ $\mu$m (blue pluses) and a packing fraction of $\phi = 0.52$. The driving parameters are $f = 45$ Hz and $\Gamma = 28$. (b) The same data as in (a) but now plotted as a function of $\mu/\sigma$, the suspending liquid viscosity over the particle diameter.

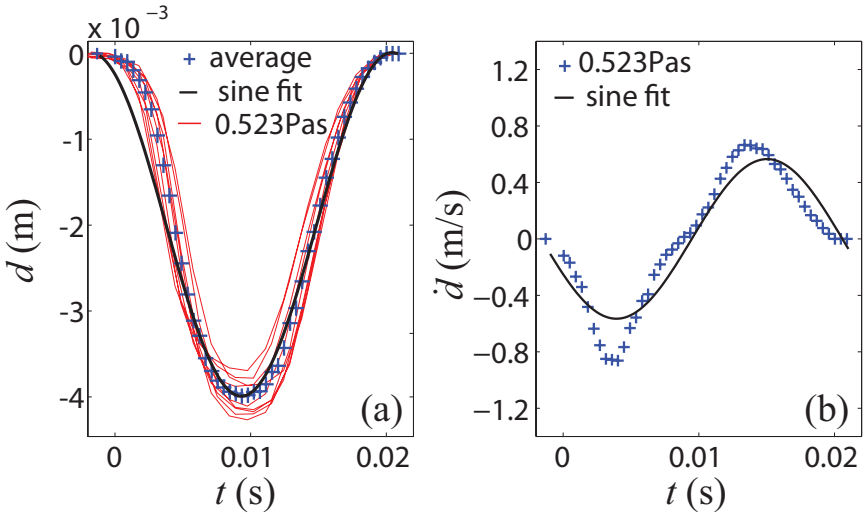


Figure 5.10: (a) Overlay of many cycles of a growing hole experiment with 40 $\mu$m beads suspended in a glycerine-water mixture of viscosity $\mu = 0.52$ Pa·s, all shifted to start at $t = 0$ and the initial diameter shifted to $d = 0$. The plus symbols indicate the cycle-averaged hole diameter.The black line is a sine fit through the average (thus neglecting the actual growth of the hole). (b) The instantaneous velocity of the growing hole averaged over all cycles. The solid line is the derivative of the sine fit of (a). The experimental parameters are, $h_0 = 6$ mm, $f = 45$ Hz, $\Gamma = 28$, and $\phi = 0.52$.

be discussed further down.

Just like we have done for the Newtonian liquids (cf. Fig. 5.6), we can overlay many single cycles and compute the cycle-averaged diameter and velocity, the result of which is plotted in Fig. 5.10. This reveals several prominent features: The first is that –quite unlike for the closing holes in the Newtonian liquids– the signal deviates significantly from a sinusoidal shape. This is especially clear when comparing the cycle-averaged velocity to the derivative of the sine fit [Fig. 5.10(b)]. In this plot we find a second remarkable feature: The magnitude of the most negative velocity ($\dot{d} \approx -0.9$ m/s) is larger than that of the most positive velocity ($\approx 0.7$ m/s), which is surprising since the hole on average must be growing, i.e., the time average $\langle \dot{d} \rangle > 0$. When determining the duration of the opening and closing parts of the cycle, we find that they are very close to one another, implying that large closing velocities occur in a narrow time interval, whereas large opening velocities are found in a broader period of time. In Fig. 5.10(b) we observe that the closing half of the cycle is sharply peaked, compared to a wider, more sinusoidal, shape during the opening half.

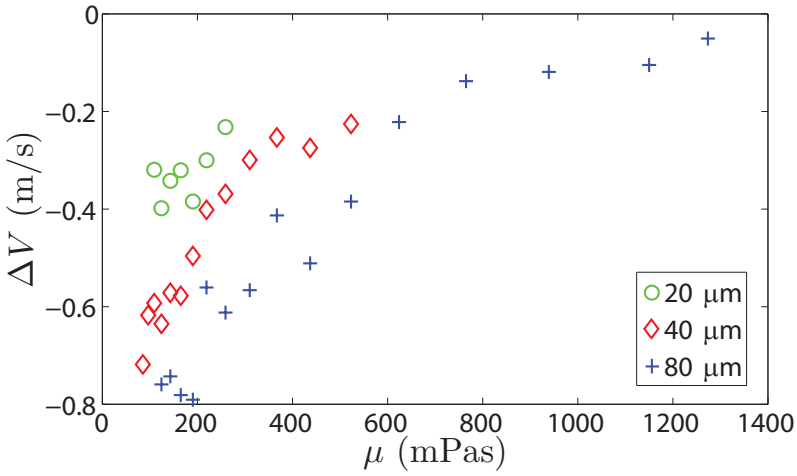


(a)

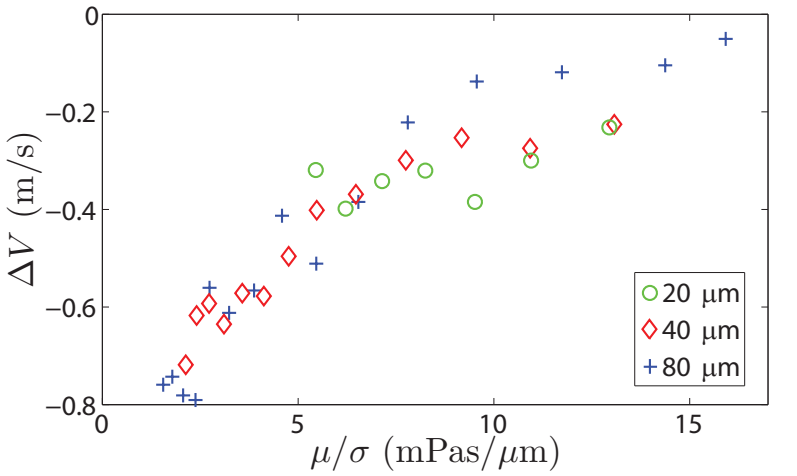


(b)

Figure 5.11: (a) The difference $\Delta V \equiv \max(\dot{d}) + \min(\dot{d})$ in the maximum opening and closing velocities in the growing hole state, averaged over all cycles as a function of the suspending liquid viscosity $\mu$, again for suspensions of all three bead diameters, $\sigma = 20$ $\mu$m (green circles), $\sigma = 40$ $\mu$m (red diamonds), and $\sigma = 80$ $\mu$m (blue pluses) and a packing fraction of $\phi = 0.52$. As before, the driving parameters are $f = 45$ Hz and $\Gamma = 28$. (b) The same data as in (a) but now plotted as a function of $\mu/\sigma$.

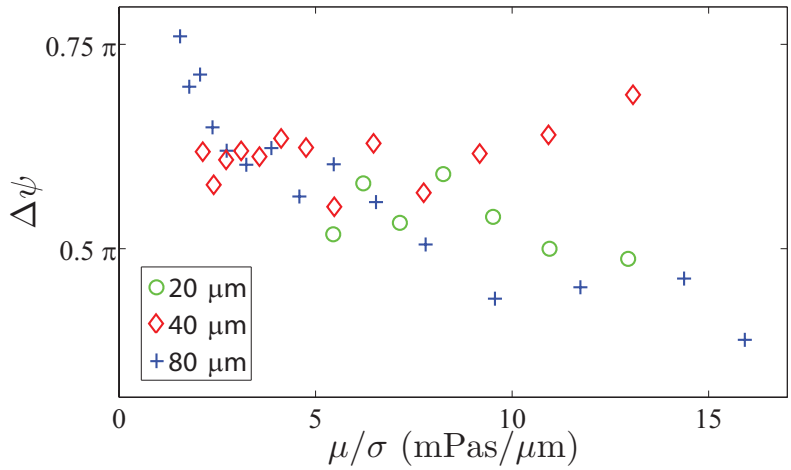


Figure 5.12: The phase difference $\Delta\psi$ between the vertical position of the container (vibrated at $f = 45$ Hz and $\Gamma = 28$) and the diameter of a growing hole, averaged over all cycles. This quantity is plotted as a function of the suspending liquid viscosity over the particle diameter $\mu/\sigma$, again for suspensions of all three bead diameters, $\sigma = 20$ $\mu$m (green circles), $\sigma = 40$ $\mu$m (red diamonds), and $\sigma = 80$ $\mu$m (blue pluses) and a packing fraction of $\phi = 0.52$.

This asymmetry is visible in all of our experiments, as can be seen in Fig. 5.11, where we plot the difference between the magnitudes of the largest opening and closing velocities $\Delta V \equiv \max(\dot{d}) + \min(\dot{d})$. The fact that $\Delta V$ is always negative expresses that the magnitude of the most negative velocity is larger than that of the most positive. Just like the average growth $\Delta d$ per cycle increased with decreasing viscosity, so does the magnitude of the velocity difference $\Delta V$, which becomes more negative as $\mu$ becomes smaller. In addition we find that the data for the different hole sizes are rather scattered in the $\Delta V$ versus $\mu$ plot, but appear to collapse when plotted against $\mu/\sigma$.

Finally, we can determine the phase shift $\Delta\psi$ between the driving and the hole although this is slightly more difficult than in the Newtonian liquid case because of the deviations from the sinusoidal shape. The results are plotted as a function of $\mu/\sigma$ in Fig. 5.12: Again the horizontal oscillation of the hole lags behind the vertical container position but now by a phase shift that is slightly larger than $\pi/2$ and that increases somewhat when the viscosity of the suspending liquid becomes smaller or the particle size becomes larger. So again the velocity with which the hole oscillates is in antiphase with the container acceleration, and as a consequence the hole velocity is in phase with the acceleration of the suspension layer.

### 5.4.2 Interpretation

It is now time to make an inventory of what we believe happens when we create a hole-shaped disturbance in a liquid layer in a container which is oscillated vertically:

- For "highly viscous" fluids (even if not Newtonian), the velocity of the hole walls is in phase with the acceleration the liquid layer experiences.
- A viscous Newtonian liquid follows the acceleration perfectly, i.e., for a sinusoidal acceleration also the velocity is sinusoidal. This stands to reason since for a viscous fluid forcing (acceleration) and the response of the liquid (the velocity profile in the layer) are proportional at all times, with viscosity $\mu$ as the proportionality constant.
- Consequently, if the liquid is non-Newtonian the proportionality factor itself depends on the forcing and therefore the response of the liquid to a sinusoidal acceleration is a deformed signal. However, if stress depends monotonously on strain rate (like, e.g., in a power-law fluid) the deformation will be symmetric, i.e., sinusoidal with a superposition of only odd higher harmonics.
- For our vertically vibrated suspension layers we find a non-symmetric velocity cycle. The negative velocity part is strongly deformed, whereas the positive velocity half is close to sinusoidal [Fig. 5.10(b)]. It appears that during the closing half of the cycle the suspension behaves strongly non-Newtonian[‖] whereas during the opening half it responds more or less like a Newtonian fluid.

The behavior in this last point can be summarized by saying that the behavior of the liquid is highly hysteretic. This is in agreement with the phenomenological model proposed by Deegan [6], who argued that a hysteretic rheology would be necessary to explain the existence of stable or growing holes in a vertically vibrated liquid layer.

Now, let us speculate about what could cause the suspension to respond in this manner. In the first half of the driving the suspension layer experiences a downward acceleration and, consequently, the suspension layer will be pushed against the bottom of the container and when set in motion by the presence of the hole it will do so with the typical non-Newtonian (shear-thinning) behavior that characterizes suspensions. In the second half of the driving, inertia actually creates a low pressure between the layer and the container bottom. Now suppose that this pressure gradient would be able to displace the liquid slightly with respect to the particle phase such that a thin layer of liquid –with a thickness comparable to the particle diameter $\sigma$– forms between the bottom and the suspension. Such a layer could act as a lubrication

[‖] In fact, from the shape of the curve in Fig. 5.10(b) one can deduce that it behaves like a shear-thinning fluid

layer, i.e., during the second half the layer would move on top of this layer and the entire velocity gradient would be in this thin layer of Newtonian liquid, i.e., it would be a shear band.

This in turn would explain why the suspension layer in the second half behaves like a Newtonian fluid, namely because this thin liquid layer is a Newtonian fluid. More specifically, if we balance the gravitational energy of the suspension layer and the dissipation in the lubrication layer we obtain

$$\rho_s g h \sim \mu \frac{\dot{d}}{\sigma} \quad \Rightarrow \quad \dot{d} \sim \rho g h \frac{\sigma}{\mu}, \tag{5.5}$$

i.e., the velocity $\dot{d}$ in the second half of the driving would scale as $(\mu/\sigma)^{-1}$. This is consistent with the fact that many of the observables ($\Delta V$ and $\Delta d$) that characterize the growth of the hole, show a better collapse when plotted against $\mu/\sigma$ rather than $\mu$ itself. Conversely, one could state that dependence on $\mu/\sigma$ indicates the existence of a shear layer of suspending liquid (with viscosity $\mu$) and thickness $\sim \sigma$.

Incidentally, the presence of such a thin shear layer can also account for the convection rolls that have been observed in the rim of these structures [2, 3]: In the first half of the driving the suspension responds with a flow profile in the layer in with the largest velocity on top and zero velocity at the bottom. In the second half, the layer slides back as a whole, on top of the thin shear layer. Consequently, the displacement per cycle of a fluid particle near the bottom is different from that near the top, giving rise to a convection roll.

## 5.5 Conclusions

We have comparatively studied the dynamics of holes in a vertically vibrated layer of viscous Newtonian liquids on the one hand and of dense particle suspensions on the other. We find that all the holes oscillate with a phase shift of $\Delta\psi = \pi/2$ with respect to the driving signal, such that the velocity of the hole is in phase with the vertical acceleration experienced by the fluid layer in the frame of reference of the container. In the Newtonian liquids we observe that holes always close, while in the suspensions holes may grow in time, depending on the driving parameters.

For the Newtonian liquids we find that the closing velocity is inversely proportional to the liquid viscosity, which is explained from a simple balance of gravitational and viscous forces. The presence of the driving is seen to hardly influence the closing: Independent of frequency and acceleration of the driving we find that the cycle-averaged closing rate of the holes is the same as for a closure that is driven by gravity only. We present a lubrication model for the closure of holes which is in good agreement with the experiments.

For the suspensions we focus on the growing holes regime and find that the growth rate of these growing holes is proportional to the ratio of the particle diameter and the suspending liquid viscosity. Comparing the growing holes to the closing ones in Newtonian liquids, we observe that in suspensions the response is highly non-linear. In addition, the symmetry of the oscillation is broken, with larger inward velocities than outward ones, which is surprising since the hole is growing. The reason is that large outward velocities only occur in a small time interval, whereas the inward ones are spread over the whole half-period. We tentatively explain this asymmetry from the formation of a thin lubricating layer of suspending liquid between the suspension and the bottom in the half-period in which the hole is opening.

## 5.6 Appendix: Modeling of hole closure in a viscous layer

A lubrication model of a horizontal axisymmetric viscous layer $h(r,t)$ starts with the axisymmetric Stokes' equation in the thin layer limit, with pressure given by the hydrostatic pressure in the layer $p = \rho g[h(r,t) - z]$. Neglecting gradients in the radial direction in comparison to those in the vertical direction, we then integrate

$$\frac{\partial^2 u_r}{\partial z^2} = \frac{\partial p}{\partial r} \quad \Rightarrow \quad u_r = \frac{\rho g}{2\mu}\frac{\partial h}{\partial r} z(z-2h)\,, \tag{5.6}$$

where we have used the no-slip boundary condition at the bottom ($u_r(0) = 0$) and the free-slip condition at the free surface ($\partial u_r/\partial z(h) = 0$). Continuity, integrated over the layer height gives

$$\frac{\partial h}{\partial t} = -\frac{1}{r}\frac{\partial}{\partial r}\left[r\int_0^h u_r(z,t)dz\right]\,, \tag{5.7}$$

which with Eq. (5.6) immediately leads to Eq. (5.1)

$$\frac{\partial h}{\partial t} = \frac{\rho g}{3\mu r}\frac{\partial}{\partial r}\left[rh^3\frac{\partial h}{\partial r}\right]\,. \tag{5.8}$$

If we look to compute the closure of a hole of initial diameter $d_0$ (at $t = 0$ s) in an infinite horizontal layer of liquid of thickness $h_0$, we can find a similarity solution to Eq. (5.8). To do so, we first nondimensionalize $h$, $r$, and $t$ with the length and time scale in the problem, namely $h_0$ and $t_0 \equiv 3\mu/(\rho g h_0)$ respectively. If we now use a selfsimilar ansatz $\widetilde{h} = \widetilde{t}^{\alpha} H(\widetilde{r}/\widetilde{t}^{\beta})$ in Eq. (5.8), we find a solution provided that $\alpha = 0$, $\beta = 1/2$

$$h(r,t) = h_0\, H\left(\sqrt{\frac{3\mu r^2}{\rho g h_0^3 (t_c - t)}}\right)\,, \tag{5.9}$$

where $t_c$ is the time at which the hole closes and $H(\eta)$ is a solution of

$$\frac{d^2H^4}{d\eta^2} + \frac{1}{\eta}\frac{dH^4}{d\eta} = -2\eta\frac{dH^4}{d\eta}$$
$$H(\infty) = 1\,; \quad H(\eta_0) = 0\,. \tag{5.10}$$

The fact that $\eta_0$ needs to be a constant implies that the rim diameter $d(t)$ should scale as

$$d(t) = d_0\sqrt{\frac{(t_c-t)}{t_c}} = 2\eta_0\sqrt{\frac{\rho g h_0^3(t_c-t)}{3\mu}}\,. \tag{5.11}$$

Note that the problem is not uniquely determined by providing $d_0$, and that in addition the closure time $t_c$ needs to be supplied to obtain a full solution to the problem. Then, $\eta_0$ can be determined as $\eta_0 = [3\mu d_0^2/(4\rho g h_0^3 t_c)]^{1/2}$ and Eq. (5.10) has a unique solution. Note, that in this case the initial profile is also fixed by the self-similar solution. Alternatively, one could therefore also start from the initial profile, match it to the solution of Eq. (5.10) for a certain $\eta_0$ which then fixes $t_c$. (This can be done provided that the initial profile is compatible with the equations.)

To obtain solutions of Eq. (5.8) that are more realistic given the experimental setup that we use, we turn to numerical simulations. Here, we replace the actual boundary conditions at the side wall (zero radial velocity and no-slip) –which are impossible to incorporate into the lubrication model– with the following integral statement of mass conservation in the system

$$\int_{r=0}^{D/2} h(r,t)rdr = \text{constant}\,, \tag{5.12}$$

where $D$ is the diameter of the container, or equivalently, taking the time derivative of Eq. (5.12) and using Eq. (5.8)

$$\tfrac{1}{2}D\left[h^3\frac{\partial h}{\partial r}\right]_{r=D/2} = 0 \quad \Rightarrow \quad \left.\frac{\partial h}{\partial r}\right|_{r=D/2} = 0\,, \tag{5.13}$$

where it was used that $h(D/2,t) > 0$. Eq. (5.8) is of a type that is known as a nonlinear diffusion equation, which is of a very stable type that renders them easy to solve numerically. The equations are therefore solved with a simple forward integration scheme which lead to results that compare well to the experiments (see Section 5.3.2).

Actually it is conceptually straightforward to incorporate the driving into the equations, as the only thing one needs to do is to substitute the gravitational acceleration $g$ with $g + a(t)$ where $a(t)$ is the instantaneous acceleration of the liquid

layer, $a(t) = a\omega^2 \sin\omega t = \Gamma g \sin\omega t$ (with $\omega = 2\pi f$). This however has enormous implications for the numerical solvability of the equations, since for $\Gamma > 1$ there exists a time interval in each cycle for which $g + a(t) < 0$. In this interval Eq. (5.8) becomes a non-linear diffusion equation with a negative diffusion coefficient, which is terribly unstable and consequently extremely difficult to solve numerically. For the current problem there exists a workaround however, for which we need some additional understanding of the equations first.

To this end let us first examine a modified Eq. (5.8) without gravity

$$\frac{\partial h}{\partial t} = \Gamma \sin(\omega t)\, \frac{\rho g}{3\mu r} \frac{\partial}{\partial r}\left[ r h^3 \frac{\partial h}{\partial r} \right] . \tag{5.14}$$

Clearly, a solution to Eq. (5.14) must have the same periodicity as the driving, i.e., $h(r,t+T) = h(r,t)$. Now, the simplest form that such a solution could have is $h(r,t) = h_s(r) + A(r)\exp[i\omega t + \varphi(r)]$, which corresponds to neglecting non-linear effects (i.e., higher harmonics) in Eq. (5.14). Now $h_s(r)$ can be any profile that satisfies the non-driven Eq. (5.14), i.e., $\partial h_s/\partial t = 0$, which is satisfied by any well-behaved function of $r$. Inserting this form into Eq. (5.14) and linearizing leads to

$$\omega A(r) e^{i(\omega t + \varphi(r) + \pi/2)} = \Gamma \frac{\rho g}{3\mu r} \frac{\partial}{\partial r}\left[ r h_s^3 \frac{\partial h_s}{\partial r} \right] e^{i\omega t} ,$$

which needs to hold for any $t$, leading to

$$\begin{aligned} A(r) &= \frac{\Gamma}{\omega} \frac{\rho g}{3\mu r} \frac{\partial}{\partial r}\left[ r h_s^3 \frac{\partial h_s}{\partial r} \right] , \\ \varphi(r) &= -\frac{\pi}{2} . \end{aligned} \tag{5.15}$$

with which

$$h(r,t) = h_s(r) + \frac{\Gamma}{\omega} \frac{\rho g}{3\mu r} \frac{\partial}{\partial r}\left[ r h_s^3 \frac{\partial h_s}{\partial r} \right] \exp[i(\omega t - \pi/2)] . \tag{5.16}$$

The full equation, including both the driving and gravity, is equal to

$$\frac{\partial h}{\partial t} = (\Gamma \sin(\omega t) + 1)\, \frac{\rho g}{3\mu r} \frac{\partial}{\partial r}\left[ r h^3 \frac{\partial h}{\partial r} \right] . \tag{5.17}$$

Note that, since we are dealing with $\Gamma \gg 1$, gravity is only a small perturbation to Eq. (5.14). This implies that the gravitational timescale at which the profile decays ($t_g \sim 3\mu/(\rho g h_0)$) is typically much larger than that of the driving. I.e., if $h_g(r,t)$ is a solution to Eq. (5.8), on the timescale of a single period it does not significantly

change and may hardly interfere with the oscillation. In analogy to Eq. (5.16), this suggests a solution to the full problem of the form

$$h(r,t) = h_g(r,t) + \frac{\Gamma}{\omega}\frac{\partial h_g}{\partial t}\exp[i(\omega t - \pi/2)], \tag{5.18}$$

where we have used that $h_g(r,t)$ is a solution to Eq. (5.8) to simplify the expression for the amplitude of the oscillation.

This line of reasoning comes to the rescue when numerically solving Eqs. (5.14) and (5.17). A first useful trick is to realize that we can numerically integrate Eq. (5.14) from $t = 0$ to $T/2$ since in this interval the coefficient of the right hand side is always positive. By going to a new time variable $\tau = -t$ we obtain a minus sign on the left hand side which exactly compensates for the minus sign of the coefficient in the interval $[-T/2, 0]$. Consequently we can integrate Eq. (5.14) backwards in time from $t = 0$ to $-T/2$, such that we obtain the solution on $[-T/2, T/2]$, i.e., a full cycle. Since the sought-for solution is periodic in time, this concludes our calculation.

For Eq. (5.17) we can proceed in a similar way and, by integrating both backwards and forwards from $t = -(T/2\pi)\arcsin(1/\Gamma) \equiv -t_c$ (where the coefficient changes sign), obtain a numerical solution on $[-T/2 + t_c, T/2 + t_c]$, i.e., also on a full period of the driving. And, of course, it is impossible to extend this interval because it is bounded by an interval where the coefficient is positive on the negative side –such that backwards integration is not possible– and similarly by an interval where the coefficient is negative on the positive side. We can however, take the solution (cq. initial condition) $h(r, -t_c)$ and integrate it using Eq. (5.8), i.e., the equation that only contains gravity, from $-t_c$ to $T - t_c$. The solution $h_g(r, T - t_c)$ is now subsequently used as an initial condition for the full problem Eq. (5.17) which we then integrate on the interval $[T/2 + t_c, 3T/2 + t_c]$. If there is any truth in the analytical approximation Eq. (5.18) the two solutions should match at the point where the two intervals meet, i.e., in $t = T/2 + t_c$. This procedure can be iterated until the solution is obtained on the full time interval [see the inset of Fig. 5.13(a)].

In Fig. 5.13(a) we plot the result of this procedure for a layer of liquid with viscosity $\mu = 1.23$ Pa·s and a thickness of $h_0 = 6$ mm, which is vibrated at a frequency of 50 Hz and a dimensionless acceleration $\Gamma = 20$. The solid line is the solution of Eq. (5.8) starting from the same initial solution and the dotted line is the solution of that same equation that is used in the integration procedure. Clearly the integration procedure appears to work well. To quantify how good it actually works, in Fig. 5.13(b) we plot the difference between directly integrating from $t = -t_c$ to $t = T/2 + t_c$ and indirectly by using the gravitational solution to reach $t = T - t_c$ and integrating Eq. (5.17) backwards in time to $t = T/2 + t_c$. The difference, normalized

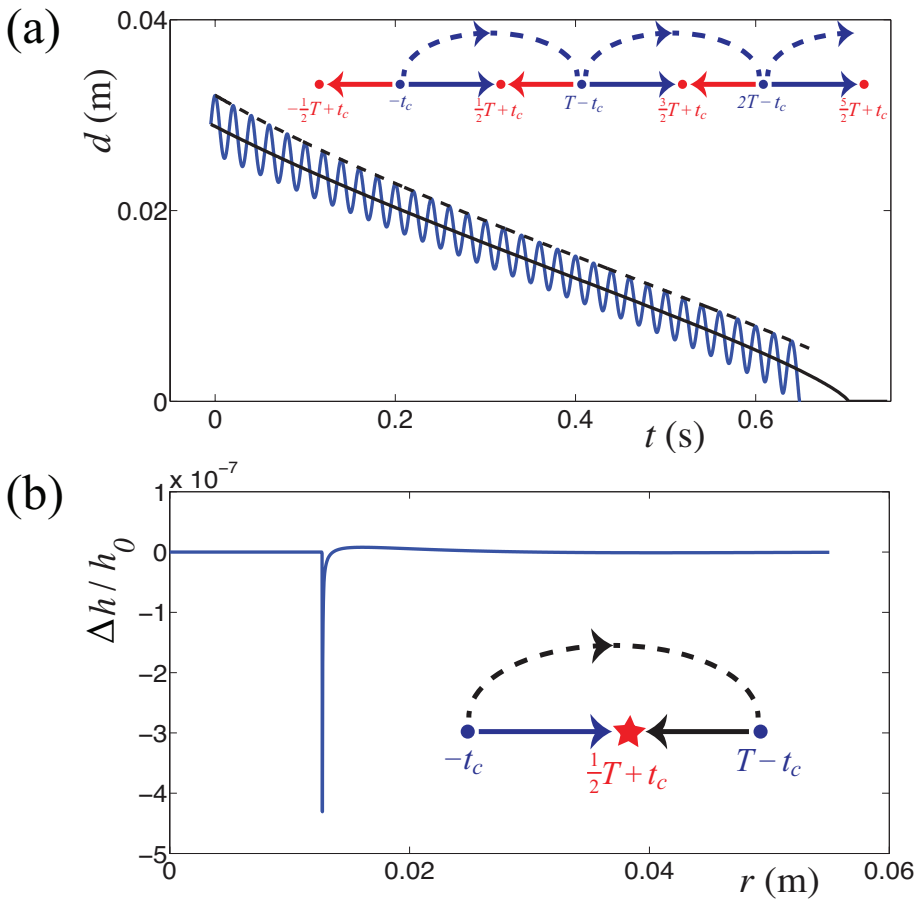


Figure 5.13: (a) Time evolution of the hole diameter in a layer of a liquid of viscosity $\mu = 1.23$ Pa·s, density $\rho = 1.26 \cdot 10^3$ kg/m$^3$ and thickness $h_0 = 6$ mm, driven at $f = 50$ Hz and $\Gamma = 20$, obtained by numerically integrating Eq. (5.17) using the procedure described in the text (blue solid line). The black lines are solutions of the corresponding gravitational closure problem Eq. (5.8), one starting from the same initial condition as the blue line (solid) and the other is the one that is used in the integration procedure of the blue curve. The inset illustrates the integration procedure. (b) Difference between the profile at $t = T/2 + t_c$ obtained starting from $t = -t_c$ by direct integration of Eq. (5.17) and by integrating Eq. (5.8) to $t = T - t_c$ and integrating Eq. (5.17) backwards in time to $t = T/2 + t_c$. The inset illustrates this procedure.

by the initial layer thickness is never larger than $10^{-6}$, illustrating the accuracy of the procedure.

## References

[1] F. Merkt, R. Deegan, D. Goldman, E. Rericha, and H. Swinney, "Persistent holes in a fluid", Phys. Rev. Lett. **92**, 184501 (2004).

[2] C. Falcón, J. Bruggemann, M. Pasquali, and R. Deegan, "Localized structures in vibrated emulsions", Europhysics Lett. **98**.

[3] H. Ebata, S. Tatsumi, and M. Sano, "Expanding holes driven by convectionlike flow in vibrated dense suspensions", Phys. Rev. E **79**, 066308 (2009).

[4] H. Ebata and M. Sano, "Self-replicating holes in a vertically vibrated dense suspension", Phys. Rev. Lett. **107**, 088301 (2011).

[5] S. von Kann, J. Snoeijer, and D. van der Meer, "Phase diagram of vertically vibrated dense suspensions", Chapter 4 of this thesis.

[6] R. Deegan, "Stress hysteresis as the cause of persistent holes in particulate suspensions", Phys. Rev. E **81**, 036319 (2010).

[7] N. Wagner and J. Brady, "Shear thickening in colloidal dispersions", Phys. Today **62**, 27 (2009).

[8] H. Barnes, "Shear-thickening (dilatancy) in suspensions of nonaggregating solid particles dispersed in newtonian liquids", J. Rheol **33**, 329 (1989).

[9] A. Fall, N. Huang, F. Bertrand, G. Ovarlez, and D. Bonn, "Shear thickening of cornstarch suspensions as a reentrant jamming transition", Phys. Rev. Lett. **100**, 018301 (2008).

[10] E. Brown and H. Jaeger, "Dynamic jamming point for shear thickening suspensions", Phys. Rev. Lett. **103**, 086001 (2009).

[11] E. Brown, N. Forman, C. Orellana, H. Zhang, B. Maynor, D. Betts, J.M.DeSimone, and H. Jaeger, "Generality of shear thickening in suspensions", Nat. Mater. **9**, 220 (2010).

[12] C. Bonnoit, T. Darnige, E. Clement, and A. Lindner, "Inclined plane rheometry of a dense granular suspension", J. Rheol. **54**, 65 (2010).

[13] E. Brown and H. Jaeger, “Generality of shear thickening in dense suspensions”, J. Rheol. **56**, 875–923 (2012).

[14] C. Bonnoit, J. Lanuza, A. Lindner, and E. Clement, “Mesoscopic length scale controls the rheology of dense suspensions”, Phys. Rev. Lett. **105**, 108302 (2010).

[15] E. B. White, M. Chellamuthu, and J. Rothstein, “Extensional rheology of a shear-thickening cornstarch and water suspension”, Rheol. Acta **49**, 119–129 (2010).

[16] B. Liu, M. Shelley, and J. Zhang, “Focused force transmission through an aqueous suspension of granules”, Phys. Rev. Lett. **105**, 188301 (2010).

[17] S. von Kann, J. Snoeijer, D. Lohse, and D. van der Meer, “Nonmonotonic settling of a sphere in a cornstarch suspension”, Phys. Rev. E **84**, 060401 (2011), chapter 2 of this thesis.

# 6

# The effect of finite container size on granular jet formation *

*When an object is dropped into a bed of fine, loosely packed sand, a surprisingly energetic jet shoots out of the bed. In this chapter we study the effect that boundaries have on the granular jet formation. We did this by (i) decreasing the depth of the sand bed and (ii) reducing the container diameter to only a few ball diameters. These confinements change the behavior of the ball inside the bed, the void collapse, and the resulting jet height and shape. We map the parameter space of impact with Froude number, ambient pressure, and container dimensions as parameters. From these results we propose a new explanation for the thick-thin structure of the jet reported by several groups.*

*Published as: Stefan von Kann, Sylvain Joubaud, Gabriel A. Caballero-Robledo, Detlef Lohse, and Devaraj van der Meer, The effect of finite container size on granular jet formation, Phys. Rev. E. **81**, 041306 (2010).

## 6.1 Introduction

Granular materials consist of discrete particles which interact mainly through contact forces. In large quantities they can behave like a solid, a liquid, or a gas but often behave differently from what would be expected of these phases [1]. A marked example is the impact of an object on a bed of sand. When dry air is blown through such a bed all contact forces between the individual particles are broken and after slowly turning off the air flow, the bed settles into an extremely loosely packed solid-like state. When a ball is dropped in such a bed, one observes a splash and a jet, strikingly similar to the ones that are seen when the same object is dropped into a liquid.

Research interest in this granular jet started when S.T. Thoroddsen and A.Q. Shen first reported this phenomenon in 2001 [2], in a study with the objective to gain insight into the importance of surface tension on jetting in general and the properties of flowing granular materials. Since these results, several aspects of the formation of the granular jet have been studied. The influence of the impact velocity onto the jet height for impacts on a bed of very loose sand was investigated in [3]. Using a pseudo two-dimensional setup, numerical simulations and comparisons to water impact experiments, a model for the jet formation was proposed that is based on cavity collapse: The impacting ball creates a cavity in the sand bed which collapses due to the hydrostatic pressure in the sand and leads to two vertical jets. One jet is observable above the bed and the other one is going down into the bed [3]. The series of events is concluded by a "granular eruption" at the surface of the sand which was attributed to the surfacing of an air bubble that is entrapped during the collapse.

The influence of the ambient pressure on the formation of a granular jet was first studied by Royer *et al.* [4]. They observed that at lower ambient pressures the jet reaches less high and also reported a puzzling thick-thin structure at lower pressures. Using X-ray radiographic measurements, they were able to look inside the bed and then proposed the following mechanism to explain this structure: the thick jet is caused by the compressed air in the cavity pushing up bed material, forming the thick part of the jet [4–6]. The thin jet was attributed to the hydrostatic collapse as formulated in [3]. Subsequently, the thick-thin structure was also observed by increasing the ball size in the same container, which suggests –in contrast to the earlier explanation– that the structure may be a boundary effect [7]. Marston *et al.* also found a thick-thin structure by decreasing the packing fraction, and they too found that this effect is more pronounced for a larger ball [8]. It is the exploration of the formation of this thick-thin structure that constitutes the main motivation for the work described in this chapter.

In parallel to the research concerning the formation of the granular jet, quite some effort was made to understand the motion of an object moving through a granular

medium. Different drag force laws were proposed [9–15], culminating in a model containing a hydrostatic term that linearly depends on the depth inside the bed and a dynamic term which is proportional to the square of the velocity of the object [14, 15]. The influence of the ambient air pressure on this trajectory was investigated in [5, 7] where it was shown that the drag force reduces at high ambient pressure. Another important issue is the interaction between the impacting ball and the container boundaries. Nelson *et al.* found that "the presence of sidewall causes less penetration and an effective repulsion" [16, 17].

In this chapter, we present experiments in which the size of the container has been systematically reduced. We did this by (i) decreasing the depth of the sand bed (section 6.4) and (ii) reducing the container diameter to only a few ball diameters (section 6.5). We explore how these confinements change the behavior of the ball inside the bed, the void collapse, the resulting jet height and shape, and the presence of a granular eruption, which was only observed in part of the parameter space covered in this study. All of the observed phenomena are explained within the context of a simple hydrostatic collapse model [3] together with a drag law for the trajectory of the ball inside the sand [15]. Finally, we propose an explanation for the presence of an eruption and a new mechanism for the thick-thin structure reported by several groups mentioned above.

The chapter is organized as follows: In Section 6.2 we start with the introduction of the drag law and the hydrostatic collapse model that lie at the heart of the analysis of this work. Subsequently we discuss our experimental setup in Section 6.3 after which we present our results for impacts in confined settings. In Section 6.4 we discuss the influence of the proximity of the bottom, after which we turn to the influence of the side walls in Section 6.5. Finally, in Section 6.6 we discuss the thick-thin structure and end with conclusions in Section 6.7.

## 6.2 Drag law and hydrostatic collapse model

In this Section we review the drag law and the Rayleigh-type collapse model that constitute the ingredients of the hydrostatic collapse model first introduced in [3] and form the theoretical backbone against which the experiments will be analyzed.

Before doing so let us briefly recall the succession of events observable after an impact of a sphere on a bed of fine, loose grains. These events are schematically represented in Fig. 6.1 and involve the introduction of several time and length scales that are crucial to the analysis in the following Sections. At a time $t = 0$, the sphere impacts on the granular medium with a velocity $v_0$. A splash is created and the ball penetrates into the sand bed. The void created by the ball collapses in a time $t_c$ (closure time) and a jet shoots out of the sand at the position of the impact. The

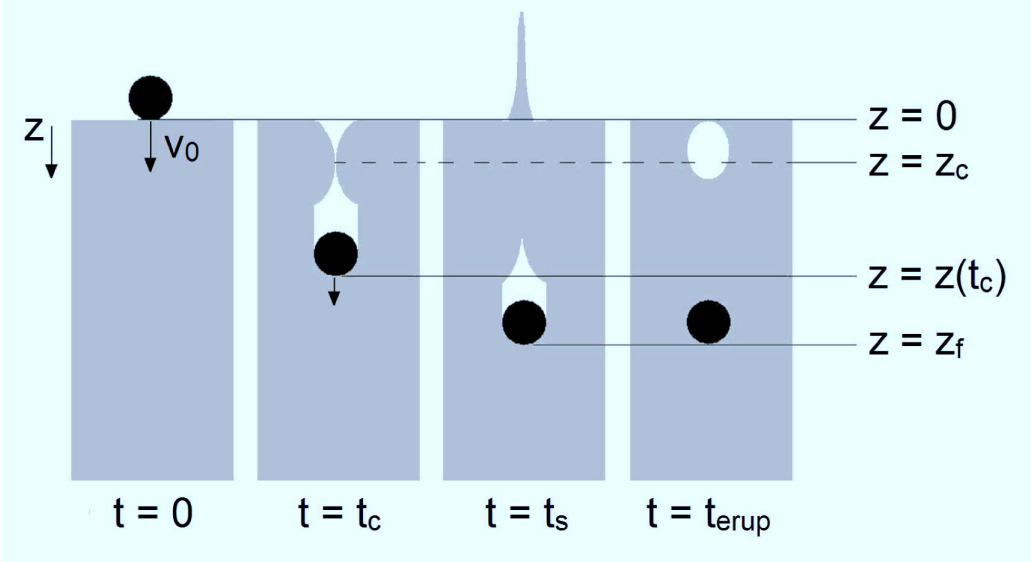


Figure 6.1: Schematic representation of the impact of a ball into a sand bed, indicating the time and length scales that play an important role in the analysis of the experimental work in this chapter, as described in the main text.

closure depth –also known as the pinch-off point– is denoted as $z_c$ and the position of the ball inside the sand at that time as $z(t_c)$. Meanwhile, the ball moves downward inside the sand bed. After a time $t_s$, the ball reaches its final depth $z_f$ and stops. Finally, a granular eruption is seen at the surface at $t = t_{\text{erup}}$, which, after comparison to 2D experiments, has been attributed to an entrapped air bubble which slowly rises inside the sand bed and reaches the surface [18].

We now turn to the hydrostatic collapse model we use to explain the observed phenomena. Its first ingredient concerns the motion of the ball with diameter $d$ through the sand bed. To describe the trajectory of the ball ($z(t)$ is the depth of the ball at a time $t$), we use the law introduced by Tsimring [14] and Katsuragi [15]. The drag force is decomposed into two terms: The first one, the hydrostatic term, involves Coulomb friction as well as the force needed to displace material against the hydrostatic pressure and is proportional to the depth and was introduced in this context in [11]. We here write $F_{\text{hydrostatic}} = \kappa z$ where $\kappa$ is a constant. The second term is an quadratic drag independent of the depth, $F_{\text{dynamic}} = \alpha v^2$, interpreted as the quadratic force required for the projectile to mobilize a volume of granular media with density $\rho_g$ proportional to the volume of the ball [†]. Adding gravity, this leads to

[†]Note that the quadratic drag is called "inertial drag" and $\alpha \equiv m/d_0$ where $m$ is the mass of the sphere and $d_0$ is the constant introduced in [15].

the equation of motion:

$$m\ddot{z} = mg - \kappa z - \alpha v^2 \,, \tag{6.1}$$

with initial conditions $z(0) = 0$ and $\dot{z}(0) = v_0$.

The second ingredient regards the dynamics of the hydrostatic collapse of the void that is formed by the ball. The radius of the void at a time $t$ and a depth $z$, $R(z,t)$, evolves from the two-dimensional Rayleigh-type equation, in which, for each depth $z$, the collapse is driven by the hydrostatic pressure $\rho_g g z$ at that depth [3]

$$(R\ddot{R} + \dot{R}^2)\log\frac{R}{R_\infty} + \frac{1}{2}\dot{R}^2 = gz \,, \tag{6.2}$$

where $\dot{R}$ denotes the time derivative and $R_\infty$ is a constant of the order of the system size. Under the assumption that the cavity that is created is approximately cylindrical, i.e., with the same diameter ($d$) as the impacting ball, the initial conditions are $R(0) = d/2$ and $\dot{R}(0) = 0$. By rescaling lengths with the ball radius $d/2$ and time with $d/(2\sqrt{gz})$ (i.e., $\widetilde{R} \equiv 2R/d$, $\dot{\widetilde{R}} \equiv \dot{R}/\sqrt{gz}$, etc., where the dot on a dimensionless variable denotes a derivative with respect to dimensionless time), Eq. (6.2) can be written in dimensionless form

$$(\widetilde{R}\ddot{\widetilde{R}} + \dot{\widetilde{R}}^2)\log\frac{\widetilde{R}}{\widetilde{R}_\infty} + \frac{1}{2}\dot{\widetilde{R}}^2 = 1 \,, \tag{6.3}$$

together with initial conditions $\widetilde{R}(0) = 1$ and $\dot{\widetilde{R}}(0) = 0$. With these initial conditions this equation has a unique solution $\widetilde{R}(\widetilde{t})$, from which we obtain a constant dimensionless collapse time $\widetilde{t}_{\rm coll}$. It now follows immediately that the (dimensional) collapse time $t_{\rm coll}$ [$= \widetilde{t}_{\rm coll} d/(2\sqrt{gz})$] scales as $\sim d/(2\sqrt{gz})$.

We can combine the above two ingredients to determine the position and the time of closure. The total time that elapses from the impact to the collapse of the cavity at any depth $z$ is given by:

$$t_{\rm tot}(z) = t_{\rm pass}(z) + t_{\rm coll}(z) \,. \tag{6.4}$$

where $t_{\rm pass}$ is the amount of time the ball takes to reach depth $z$ (obtained from solving the drag law) and $t_{\rm coll}$ is the time needed for the collapse at a depth $z$. The closure depth $z_c$ is the depth which minimizes equation 6.4. The closure time corresponds to the total time at the closure depth ($t_c \equiv t_{\rm tot}(z_c)$).

Finally, as argued in [7] within the context of the hydrostatic collapse model, the jet height $h_{jet}$ is expected to be proportional the closure depth $z_c$. This is because the pressure that drives the collapse must be proportional to the pressure that builds up after collapse along the vertical axis, which pushes out the jet. Consequently, the initial jet velocity $v_{jet}$ is expected to scale as the square root of the closure depth $v_{jet} = C\sqrt{gz_c}$.

## 6.3 Experimental setup

In the previous section, we have introduced the theoretical framework for the analysis of the phenomenon. We now turn to the description of the experimental setup, which is sketched in Fig. 6.2. It consists of a container with a height of 1 m and a square cross section of $14 \times 14$ cm$^2$, which is filled with sand grains, nonspherical and slightly polydisperse in size (between 20 and 60 $\mu$m); the density of the granular medium is 2.21 g/cm$^3$ and its angle of repose 26°. As described in [7], before each experiment, the sand is fluidized by blowing pressurized dry air through a sintered plate at the container bottom. After slowly turning off the air flow, the bed reproducibly settles into a static, loose, weakened state (volume fraction 41 %). The airtight system can be slowly evacuated to perform experiments at lower ambient pressures $p$ (the pump speed is low enough not to irreversibly alter the packing fraction). Then a steel ball of diameter $d = 1.6$ cm and mass $m = 16.5$ g is dropped into the sand from different heights $H$ which controls the impact velocity $v_0 = \sqrt{2gH}$, where $g$ is the acceleration of gravity. Thus, the impactor is characterized by a single dimensionless number, the Froude number (Fr), defined as $\mathrm{Fr} = 2v_0^2/(gd) = 4H/d$.

The impact is recorded with a high-speed camera (Photron Ultima APX-RS) at 1500 frames per second. For the measurements a uniform lighting from behind is needed to obtain better movies with higher contrast between the objects and the background. This is realized by positioning two light sources and a diffusing plate behind the container.

In order to obtain the trajectory of the sphere inside the sand, we attach a wire with markers which remain above the sand during impact and are imaged with the high-speed camera. This procedure is explained in greater detail in Section 6.5-A.

We use two ways to confine the impact and jet formation experiment. First of all, we study the influence of the bottom of the container by reducing the height at which the container is filled with sand down to a few ball diameters (Section 6.4). Second, to investigate the influence of the closeness of the side walls, we insert PVC cylinders of varying diameters into the sand, such that the cylinder axis coincides with the trajectory of the ball inside the sand. In this procedure sufficient care was taken that the presence of the cylinder did not disturb the fluidization and settling process of the sand bed (Section 6.5).

### Time and position of collapse

When traveling through the sand bed, the ball creates a cavity. The shape of the cavity is obtained using a profilometer similar to the one described in [19] (see Fig. 6.3). A diode laser sheet with wavelength of 680 nm strikes the granular media at an angle $\theta$, fixed arbitrarily at 55°. Using a mirror and a high-speed camera, we can measure the

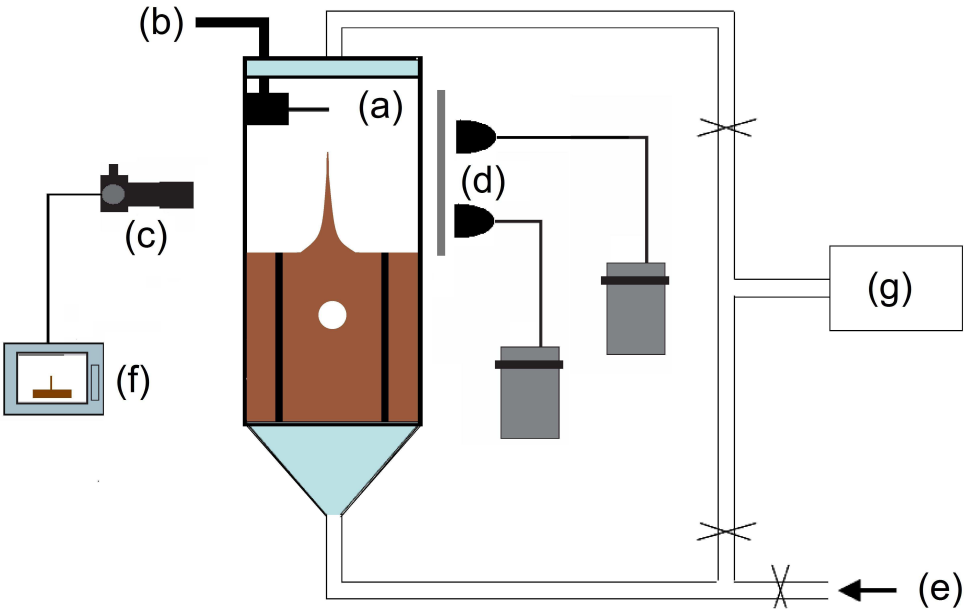


Figure 6.2: Setup: (a) perspex container, $14 \times 14 \times 100$ cm$^3$, (b) pneumatic release mechanism, (c) Photron Ultima APX-RS, (d) two light sources with diffusing plate, (e) pressurized, dry air source, (f) computer and (g) vacuum pump with pressure gauges.

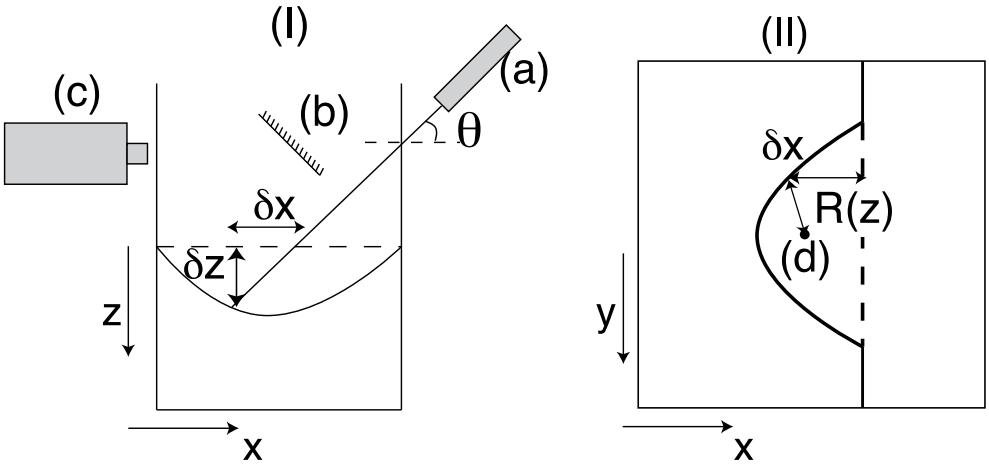


Figure 6.3: (I) Laser profilometer. A diode laser sheet (a) is directed onto the surface at an angle $\theta$. Using a mirror (b) and a high-speed camera (c), images of the surface are recorded. (II) Schematic view of the resulting surface. The dashed line represents the laser sheet when the surface is flat and the continuous line the laser sheet when the surface is perturbed. The local deviation $\delta x = x(y) - x_l$ of the laser sheet is related to the vertical coordinate $\delta z = z(y)$ of the surface. (d) is the center of the cavity, from which the cavity radius $R(z)$ can be deduced.

horizontal projection of the points where the laser sheet touches the sand from above. When the surface is flat, this projection is a straight line parallel to the $y$-direction; the coordinate of a point on this straight line is ($x_l$, $y$). When the surface is perturbed, the projection appears to be a curved line. For any point on this line with coordinate ($x(y)$, $y$)) the depth of the surface can be deducted –as a function of y– from $x_l$ and $x(y)$

$$z(y) = (x(y) - x_l)\tan(\theta)\,. \tag{6.5}$$

If we assume rotational symmetry of the cavity around the center of the ball [denoted as ($x_c$,$y_c$)] we can in addition deduce the radius of the cavity at all these depths $z(y)$

$$R(z(y)) = \sqrt{(x(y) - x_c)^2 + (y - y_c)^2}\,. \tag{6.6}$$

By analyzing each of the high speed imaging recordings in this way, we can obtain the cavity profile $R(z,t)$ as a function of both depth $z$ and time $t$ (up to a certain maximum depth that is set by the laser sheet angle $\theta$).

## 6.4 Influence of the bottom: A shallow bed

Now that we have introduced the experimental setup, we will continue with the discussion of our results: In this Section we start with what is observed in a less-filled container (i.e., a shallow sand bed) and in the next Section proceed with the discussion of what happens when the diameter of the system is decreased.

Before turning to the case in which the proximity of the container bottom becomes important, let us first recall in table 6.1 the results obtained in the usual unconfined case, here at Fr $= 70$ and ambient pressure: the container is large enough ($D = 14$ cm $\gg d$) to avoid any effect of the surrounding walls and deep enough (the height of the sand bed, $h_{\text{bed}}$ is around 30 cm, that is $18.75\,d$) such that the bottom has no influence.

| Final depth $z_{\text{f}}$ | Stopping time $t_{\text{stop}}$ | collapse time $t_c$ |
|---|---|---|
| $11\,d$ | 110 ms | 51 ms |
| closure depth $z_c$ | jet height $h_{\text{jet}}$ | eruption time $t_{\text{erup}}$ |
| $2\,d$ | $18.5\,d$ | 510 ms |

Table 6.1: Results obtained at Fr $= 70$ and $p = 1$ bar in the usual unconfined case, i.e., in a deep bed with $h_{\text{bed}} = 18.8\,d$. These values will be used as reference values in the discussion of the experimental results.

We modified the height of the sand bed, $h_{\text{bed}}$ by simply adjusting the amount of sand in the container. The first and most conspicuous effect is that below a certain depth of the sand bed the impacting sphere is stopped abruptly by its collision with the container bottom, rather than slowly being stopped by drag as happens in the unconfined case. In this way, decreasing the depth of the sand bed allows us to look at the influence of the final depth of the ball, $z_{\text{f}}$, and the cavity size on the jet and the eruption.

### 6.4.1 Influence on the jet

In Fig. 6.4, we show four images from the jet formed when the ball is dropped into the sand bed for Fr $= 70$ and ambient pressure. While reducing $h_{\text{bed}}$, there is no change in the jet shape or height down to a certain threshold. Below this threshold, the jet reaches less high and becomes broader, most notably at the top. The maximum height of the jet, $h_{\text{jet}}$, is obtained by measuring the initial jet velocity $v_{\text{jet}}$ as soon as it appears above the surface of the sand (using energetic arguments, $h_{\text{jet}} \propto v_{\text{jet}}^2$). The initial jet velocity $v_{\text{jet}}$ is plotted as a function of $h_{\text{bed}}$ in Fig. 6.5: For $h_{\text{bed}}$ higher than $3\,d$, $v_{\text{jet}}$

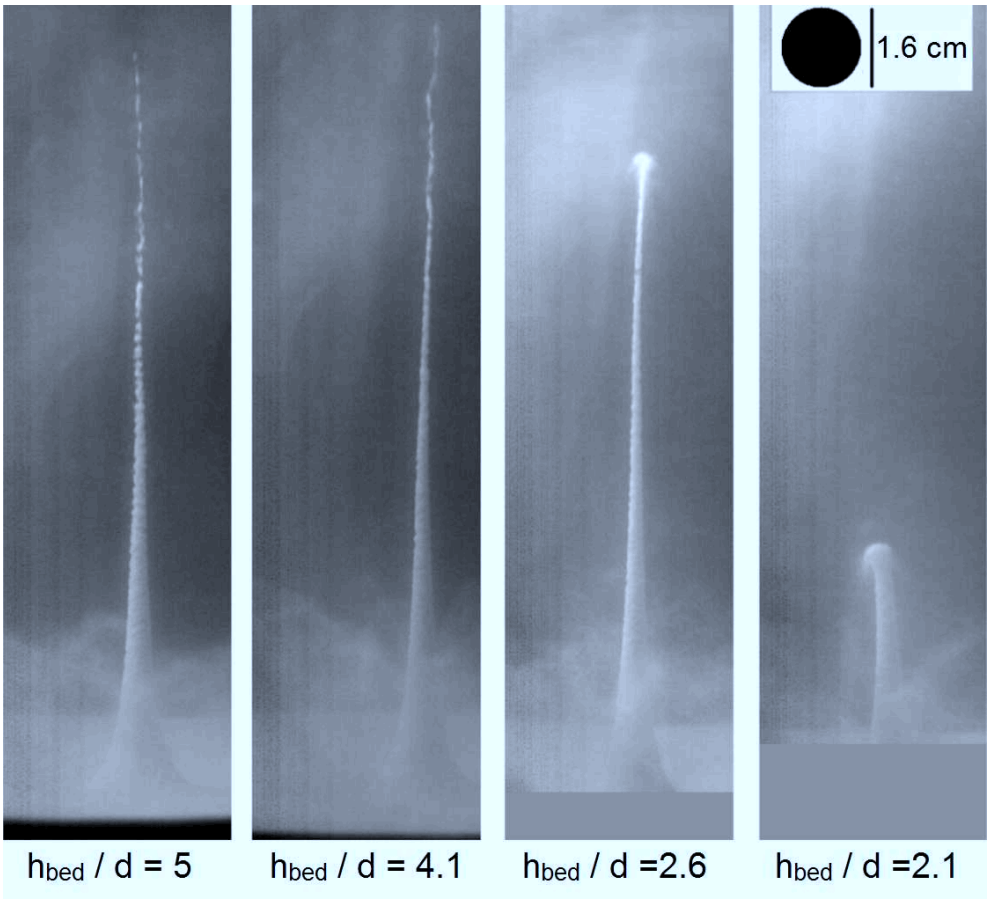


Figure 6.4: Influence of the height of the sand bed $h_{\text{bed}}$ on the shape and height of the jet for Fr $= 70$ and $p = 1$ bar: Images of the jet, taken at 0.12 s after the ball impact for four different bed heights, decreasing from left to right. Below a threshold there is a clear change in height and width of the jet.

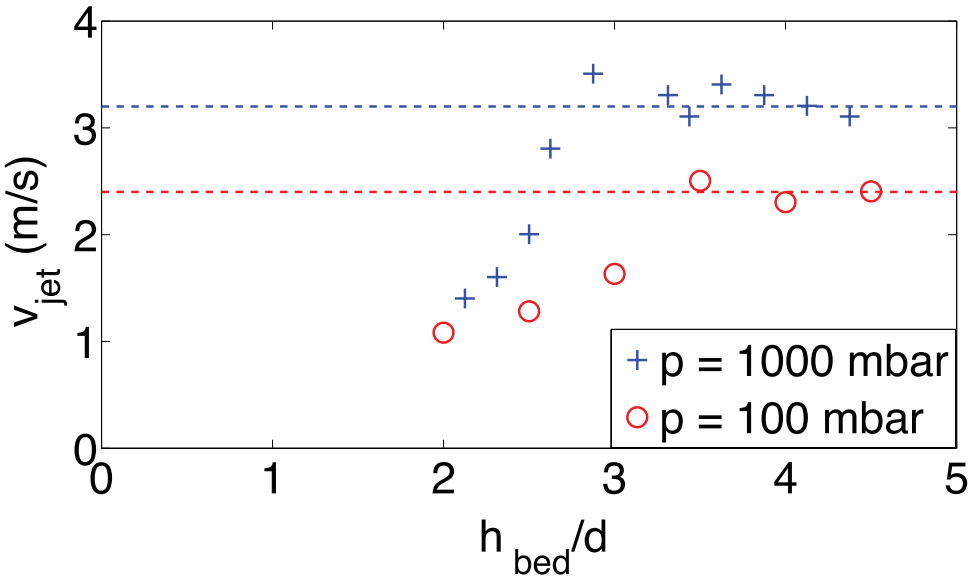


Figure 6.5: Initial velocity of the jet, $v_{\text{jet}}$ as a function of the height of the sand bed, $h_{\text{bed}}$ for Fr $\sim 70$ and $p = 1000$ mbar (+) and $p = 100$ mbar (○). There is a sharp threshold below which the initial jet velocity rapidly decreases. The dashed lines represent the undisturbed values of $v_{\text{jet}}$, measured in a deep bed ($h_{\text{bed}} = 18.8\,d$).

saturates to its undisturbed value of approximately 3.2 m/s. Reducing $h_{\text{bed}}$ below $3\,d$, $v_{\text{jet}}$ decreases rapidly. When we reduce the ambient pressure to $p = 100$ mbar, we find the same behavior (see Fig. 6.5) although the crossover takes place at a slightly higher value of $h_{\text{bed}}$. Remarkably, in both cases this decrease does not happen at the depth at which the ball is stopped by the bottom (which would be around $h_{\text{bed}} = 11\,d$ and $h_{\text{bed}} = 6\,d$ for $p = 1000$ mbar and $p = 100$ mbar respectively) but at a much lower depth of $h_{\text{bed}} \approx 3\,d$.

This can be explained as follows: The closure depth, $z_c$, remains unaltered by the presence of the bottom (which below $h_{\text{bed}} = 11\,d$ only makes the ball stop earlier and less deep) until the bed depth becomes less than the sum between the position of the unconfined collapse ($2\,d$, see table 6.1) and the diameter of the ball. Below this value, the collapse happens on top of the ball leading to a less directional top of the jet which has a more or less spherical shape; moreover the closure depth decreases when the bed becomes smaller and so does the initial jet velocity.

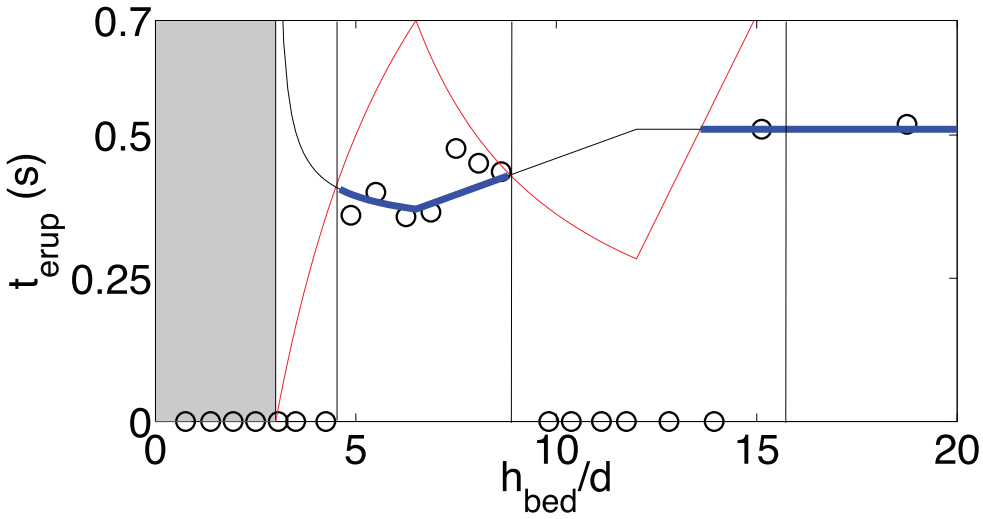


Figure 6.6: The time $t_{erup}$ when the granular eruption at the surface starts is plotted as a function of the height of the sand bed $h_{bed}$, for Fr $= 70$ and $p = 1$ bar (black open circles). Measurement points with $t_{erup} = 0$ correspond to those cases where no eruption was observed. The experimental regimes with and without eruption are separated by the vertical black lines. The grey region represents the region where no air bubble is entrapped. The thin black and red lines represent the different time scales that are involved in the problem $t_1$ is the time the air bubble needs to reach the surface (black thin line) and $t_2$ is the time the air bubble needs to diffuse within the sand bed (red thin line). When $t_1$ is smaller than $t_2$, an eruption is expected; this is depicted by the continuous thick blue line. The different regions obtained from the timescale argument qualitatively correspond to the experimental results. More details about the way in which $t_1$ and $t_2$ are estimated are provided in the main text.

### 6.4.2 Influence on the eruption

Providing that the void collapse does not happen directly at the ball, an air bubble is entrapped. The volume of this bubble can be estimated as:

$$V_{\text{bubble}} \propto h_{\text{rad}}^2 (z(t_c) - z_c) \sim d^2 (z(t_c) - z_c), \tag{6.7}$$

where $z(t_c)$ is the position of the ball at closure and $h_{\text{rad}}$ is the radial length scale of the bubble, which can be approximated by the diameter of the ball. The bubble slowly rises through the sand and can lead to a violent granular eruption. However, this eruption is not always observed. To study when and why this is the case, in Fig. 6.6 we plot the time between impact and eruption, $t_{\text{erup}}$, as function of the height of the sand bed, $h_{\text{bed}}$. (Note that measurement points with $t_{\text{erup}} = 0$ correspond to those cases where no eruption was observed.) Up to a certain threshold, which is around $4.8d$, no eruptions can be observed. This can be attributed to the fact that, while rising, small air bubbles just dissolve into the sand bed before reaching the surface. When the bed gets deeper, the air bubble reaches a certain critical volume $V^*$, above which a granular eruption can be seen. From the experimental results, this size found to be around $V^* \sim d^2(z(t_c) - z_c) \sim 3.8d^3$. Then remarkably, above $9d$ the eruptions disappear again and reappears only when $h_{\text{bed}} > 14d$.

This peculiar behavior can be understood, at least qualitatively, from the competition of the two time scales corresponding to the two mechanisms the air in the bubble has to escape from the bed:

- The bubble needs a time $t_1$ to reach the surface. First of all, for $h_{\text{bed}} < 3d$, the collapse happens on top of the ball, and no air bubble is entrapped. Between $3d$ and $5.5d$, the position of the ball at closure, $z(t_c)$, increases and so does the volume of the air bubble; in this region, $t_1$ decreases. While increasing the sand depth even further, the volume of the air bubble remains constant, but the initial position of the bubble is deeper since the entrapped bubble will follow the ball until it stops. Therefore $t_1$ will increase until $h_{\text{bed}}$ is equal to $11d$ which is the final depth of the ball in the unconfined case. Above this value, there is no change on the final depth and $t_1$ becomes independent of the depth of the sand bed. This is depicted by the thin black line in Fig. 6.6.

- The air in the bubble trapped by the collapse escapes –in the dissolution time $t_2$– through pressure driven flow through the porous bed. Factors that affect this process are the size of the bubble (which determines the amount of air that needs to escape), the pressure of the air (which approximately equals the hydrostatic pressure in the surrounding sand), and the length of the path the air needs to travel. For this last quantity we need to consider that air can both

escape through the top and through the bottom of the bed, the latter due to the presence of the sintered plate. These factors combine into Darcy's law: $Q \propto \Delta P/H$, where the flow rate $Q$ depends on the pressure difference $\Delta P$ driving the flow and the path length $H$. Turning to Fig. 6.6 again, for $h_{\text{bed}} < 3d$, no air bubble is entrapped. Between $3d$ and $5.5d$, $z(t_c)$ –and therefore the bubble size– increases, leading to a steep increase of the dissolution time $t_2$. Upon increasing the sand depth beyond $5.5d$ the bubble size remains constant but the pressure inside the bubble increases. From Darcy's law we thus find that $t_2$ decreases. This continues until $h_{\text{bed}}$ is equal to $11d$ beyond which the ball does not reach the bottom of the plate anymore. Note that until this point the shortest (and therefore chosen) path for the bubble to dissolve is towards the bottom of the container. If we now increase $h_{\text{bed}}$ beyond $11d$ this shortest path starts to grow, and with the path, using Darcy's law, also the dissolution time. This is captured by the thin red line in Fig. 6.6.

As a result, an eruption can be only seen if the time $t_2$ becomes larger than $t_1$ [‡]. This is expressed by the continuous thick blue line, in qualitative agreement with the experimental behavior.

[‡]Starting from the collapse time $t_c$, the rise time of the bubble has been estimated as that of similarly sized bubble in a liquid experiencing Stokes drag, assuming that it rises in a straight path with its terminal velocity immediately, i.e., from the balance $\phi\rho_g V_{\text{bubble}} g \propto \eta V_{\text{bubble}}^{1/3} v_{\text{rise}}$ (with the packing fraction $\phi$ and the dynamic viscosity $\eta$ assumed to be constant) we have $v_{\text{rise}} \propto V_{\text{bubble}}^{2/3} g$ with $V_{\text{bubble}} \propto (z(t_c) - z_c)d^2$. Now, we estimating the initial position of the top of the bubble as $z_{\text{f}} - (z(t_c) - z_c)$. This leads to $t_1 = (z_{\text{f}} + z_c - z(t_c))/v_{\text{rise}} \propto (z_{\text{f}} + z_c - z(t_c))(z(t_c) - z_c)^{-2/3} d^{-4/3} g^{-1}$. The proportionality constant was fitted to give the correct large depth behavior.

Regarding the dissolution time up to $h_{\text{bed}} \approx 11d$ we can estimate the pressure difference by the hydrostatic pressure in the center of the bubble at the moment the ball has stopped, *i.e.* $\Delta P \approx \phi\rho_g g(z_{\text{f}} - (1/2)(z(t_c) - z_c))$ (where $z(t_c)$ equals $h_{\text{bed}} - d$ for $h_{\text{bed}} \leq 5.5d$), the volume of entrapped air again as $V_{\text{bubble}} \propto (z(t_c) - z_c)d^2$, and, since ball reaches the bottom, the shortest path is around the ball through the sintered plate, i.e., $H \approx d$. Using Darcy's law we have $t_2 \approx V_{\text{bubble}}/Q \propto V_{\text{bubble}} H/\Delta P$. Inserting the above quantities we obtain $t_2 \propto (z(t_c) - z_c)d^3/(\phi\rho_g g(z_{\text{f}} - (1/2)(z(t_c) - z_c))$. Above $h_{\text{bed}} = 11d$ only the path length changes to $H \propto h_{\text{bed}} - z_f$ such that $t_2 \propto (z(t_c) - z_c)(h_{\text{bed}} - z_f)d^2/(\phi\rho_g g(z_{\text{f}} - (1/2)(z(t_c) - z_c))$. Again, the proportionality constant was used as a fitting parameter.

## 6.5 Influence of the side walls

In the previous section, we discussed the influence of the bottom of the cavity on the process of object penetration and jet formation and found that, if the sand depth is fixed at 30 cm, there is no effect of the bottom on the jet formation process. Fixing this bed depth, we now turn to study the effects of the side walls of the container on the complete series of events leading to the jet. For this, some cylinders of different diameters $D$ are placed inside the sand during the fluidization process: we choose $D = 4.2$ cm, 6 cm, 8.5 cm, 10 cm and 12.5 cm. In this way we change the aspect ratio $D/d$ from 2.6 to 7.8.

### 6.5.1 Ball trajectory

The first thing that happens upon impact of the ball onto the surface is that it penetrates and creates a void inside the sand bed. The question we ask in the next subsection concerns the influence of the container diameter on the drag force experienced by the ball during its motion through the bed. To monitor the trajectory of the ball, a wire with a tracer is attached to the ball. Using a high-speed camera (1500 frames per second) and image analysis, we obtain the trajectory of the tracer and therefore the trajectory of the ball $z(t)$. To keep the wire tense an extra friction device and a light counterweight are used, which have the effect that the ball experiences a downward acceleration due to gravity which is approximately 10 % smaller than $g$. The actual acceleration is measured during the "free fall" part of the trajectory, and the results presented here have been corrected for this effect.

In the top two plots of Fig. 6.7, we compare the trajectories of the ball at ambient pressure for an impact with $\mathrm{Fr} = 25$ and for two diameters of the confining cylinder ($D = 6.0$ and 10.0 cm). We can fit the experimental trajectories using the model introduced in Section 6.2 (Eq. 6.1) using $\alpha$ and $\kappa$ as fitting parameters. The agreement between the model and the experiments is very good (see Fig. 6.7).

Decreasing the diameter of the container surprisingly increases both the final depth of the ball, $z_\mathrm{f}$ and the time to reach the final depth, $t_\mathrm{s}$. In Fig. 6.8a, we report the final depth $z_\mathrm{f}$ as a function of the container diameter at different pressures for $\mathrm{Fr} = 25$. There is a clear dependence: The final position of the ball is deeper for a smaller container. Also, the influence of the boundaries for this Froude number is less pronounced at small pressures. We conclude that for $\mathrm{Fr} = 25$ the drag force the ball experiences becomes smaller for small containers.

But what happens at higher Froude numbers? In Fig. 6.8b, we report the final depth, $z_\mathrm{f}$ as a function of the container diameter for $\mathrm{Fr} = 75$. At first glance the behavior now seems completely opposite to what we observe at small Froude number, as the final depth now decreases with decreasing container diameter: To be more

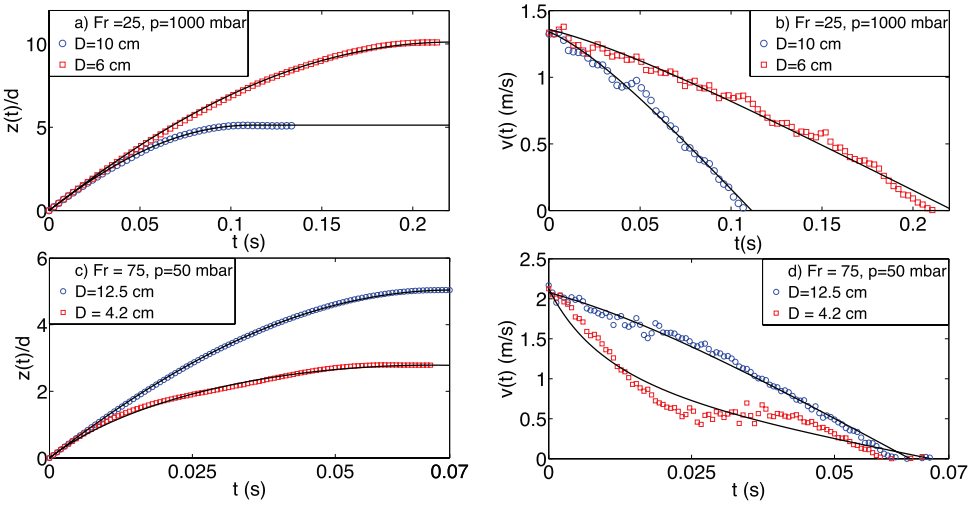


Figure 6.7: *(top)* Depth of the ball $z(t)$ (a) and its velocity $v(t)$ (b) as a function of time after impact for Fr $= 25$, $p = 1000$ mbar, $D = 10$ cm ($\circ$) and $D = 6$ cm ($\square$). The lines correspond to a fit using equation 6.1 with $\kappa = 4.525$ N/m and $\alpha = 0.132$ kg/m for $D = 10$ cm and $\kappa = 1.695$ N/m and $\alpha = 0.118$ kg/m for $D = 6$ cm. *(bottom)* Depth of the ball $z(t)$ (c) and its velocity $v(t)$ (d) as a function of time after impact $t$ for Fr $= 75$, $p = 50$ mbar $D = 4.2$ cm ($\circ$) and $D = 12.5$ cm ($\square$). Again, the lines correspond to a fit using equation 6.1 with $\kappa = 14$ N/m and $\alpha = 0.281$ kg/m for $D = 4.2$ cm and with $\kappa = 13.5$ N/m and $\alpha = 0.111$ kg/m for $D = 12.5$ cm. Within the smallest container, and only at low pressure, we observe anomalous behavior: The ball reaches a plateau in which the velocity remains constant before going to zero again at larger times. Clearly, the model fails to describe the data in this case.

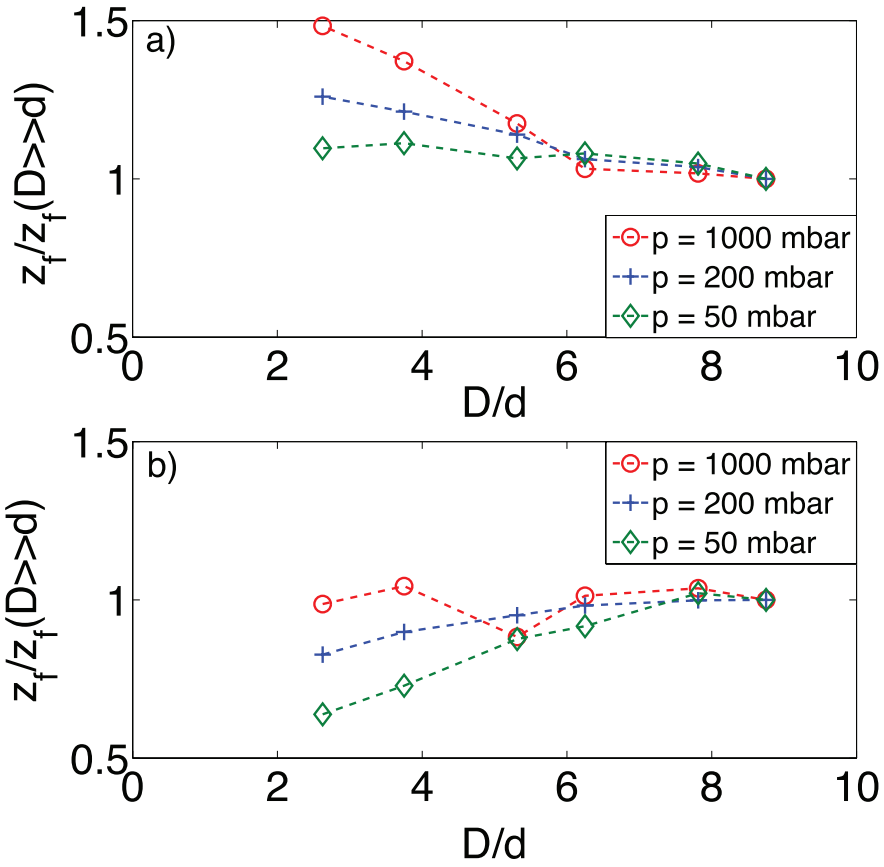


Figure 6.8: Final depth $z_f$ as a function of the container diameter $D$, at different pressures, for a) Fr = 25 and b) Fr = 75. The final depth is divided by the final depth for the unconfined case in order to emphasize the deviations due to the proximity of the boundaries. The dashed lines are a guide to the eye to separate the different pressures.

precise, at atmospheric pressure the final depth stays more or less constant and at lower pressures there is a decrease in $z_f$ with decreasing container diameter. So now the drag force seems to be larger for small container diameters.

To understand this difference, we have to separately look at the behavior of the hydrostatic and quadratic drag force: After all, for small Froude numbers we expect that the hydrostatic drag $-\kappa z$ will dominate the behavior of the ball, whereas for higher impact velocities it is expected that the quadratic drag $\alpha v^2$ will start to become increasingly more important during the motion of the ball. To this end, in Fig. 6.9 we plot $\kappa$ and $\alpha$ as a function of container diameter for three different pressures. Each value represents the average parameters obtained from fits to the trajectory data analogous to the ones of Fig. 6.7 over a range of Froude numbers from 25 to 100 [§]. As shown by Caballero [7], the hydrostatic force depends on the ambient air pressure: $\kappa$ decreases with $p$ roughly as $p^{-1/2}$. Our findings are consistent with this observation, also for smaller container diameters (not shown). Next to this we find that $\kappa$ increases quite steeply with $D$, which is consistent with the lower drag experienced by the impacting ball at smaller container diameters at low Froude numbers. Physically, the behavior of the hydrostatic drag force can be understood using a similar argument as [7]: When the ball passes through the sand, an air flow is created around it which fluidizes the sand bed and reduces the drag force. This effect is expected not only to be more important at higher pressure but also when the container diameter becomes smaller: Near the wall, the velocity of the interstitial air is required to be zero and, since the same amount of air needs to be displaced, the flow will be more important if the aspect ratio $D/d$ is small. Consequently, the hydrostatic drag force will be lower.

Figure 6.9b contains the coefficient $\alpha$ of the quadratic drag term $\alpha v^2$. Clearly, $\alpha$ becomes larger for smaller container diameters but the difference is hardly as pronounced as was the case for $\kappa$. This accounts for the observation that at some point, for larger Froude number, the drag does become larger when the container diameter is decreased.

Finally, in Figs. 6.9a and b there is one exceptional value: For the smallest container diameter ($D/d = 2.6$) and the lowest pressure (50 mbar) the fitted values of $\kappa$ and $\alpha$ turn out to strongly depend on the Froude number. The bottom two plots in Fig. 6.7, which contain two trajectories at 50 mbar for the largest and the smallest container diameter, reveal the reason why: Whereas for the biggest container ($D = 12.5$ cm), the behavior is similar to the behavior described for $\mathrm{Fr} = 25$, for the smallest one ($D = 4.2$ cm) it is qualitatively different. Whereas the agreement between the experimental and the computed trajectory sill seems to be reasonable

[§]The (small) differences in the fitting parameters $\kappa$ and $\alpha$ found for the various Froude numbers were consistent with the measurement error, except for the smallest container diameter at the smallest pressure, as explained in the text.

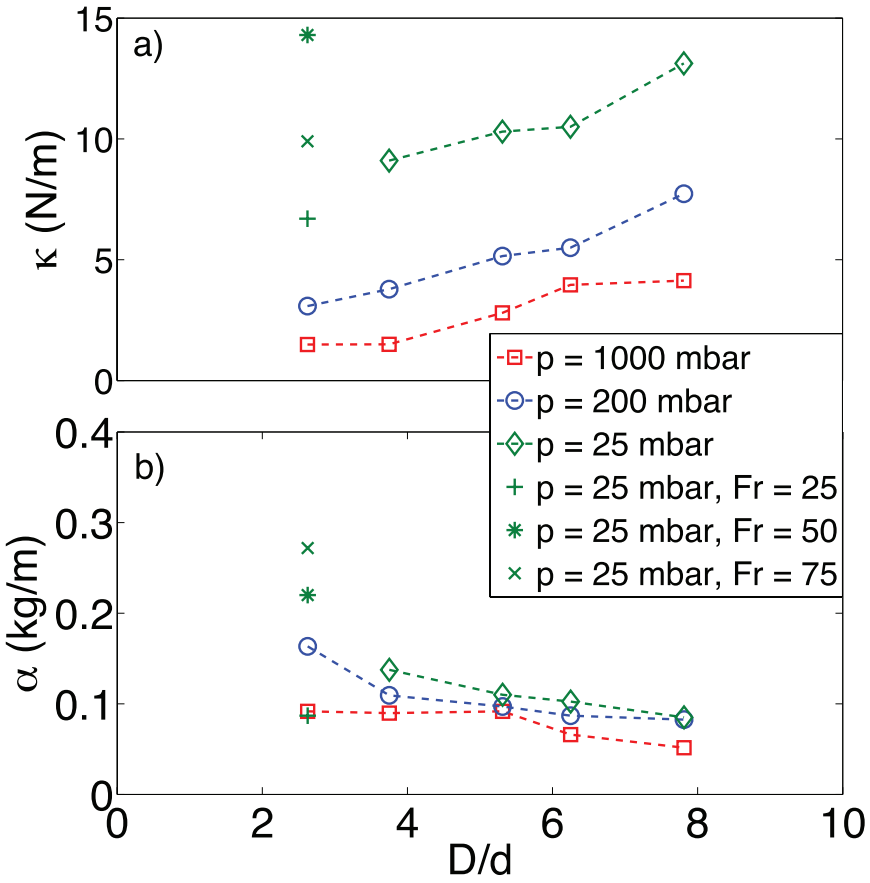


Figure 6.9: a) $\kappa$ and b) $\alpha$ as a function of cylinder diameter $D$ for different pressures $p$. For almost all values of $D$ and $p$ variations of both $\kappa$ and $\alpha$ are within the measurement error and each point is obtained from an average over a range of Froude numbers from 25 to 100. Only for the smallest container ($D/d = 2.6$) and the lowest pressure (50 mbar), there is a strong dependence of $\kappa$ and $\alpha$ on the Froude number; the model is not valid in this situation. Plot b) reveals that for large Fr the quadratic drag takes over for small cylinder diameters leading to less intrusion of the ball (Fig. 6.8b).

(Fig. 6.7c), the velocity of the ball (Fig. 6.7d) presents large discrepancies: The measured ball velocity doesn't decrease to zero gradually, but first slows down until it reaches a plateau at constant velocity where it stays for a while before slowing down until it stops. This behavior is identical to the one observed in the X-ray experiments of Royer *et al.* [6], in which the container needed to be kept small. The fact that the velocity plateau is only present for small container diameters, clearly indicates that it is a boundary effect.

We believe that the origin of the plateau lies in an additional force acting on the sphere that originates from the side walls and is mediated by the sand grains [¶]. In order to produce a constant velocity during some time interval, this force must be depth-independent, dominant over the hydrostatic drag force and must, together with the quadratic drag force, balance gravity at the plateau velocity. The constant velocity regime ends when, at a certain depth, the Coulomb drag force takes over again, slowing the ball down to zero. The verification of this assertion goes beyond the technical possibilities of our set-up and asks for further study.

### 6.5.2 Collapse of the cavity

The second issue that we want to address in this Section is the influence of the container diameter on the collapse of the cavity. We study the dynamics of the collapse of the cavity at closure depth using the profilometric method described in detail in Section 6.3. In Fig. 6.10, the radius of the cavity is plotted as a function of time $t - t_{\text{pass}}$ for two different diameters at atmospheric pressure where $t_{\text{pass}}$ is the time needed for the ball to reach the closure depth $z_c$. We can clearly distinguish a slight expansion of the cavity followed by a strong contraction. The collapse accelerates towards the pinch-off. Due to experimental limitations we do not have enough spatial resolution to obtain data points close to the pinch-off. The void dynamics is in qualitative agreement with the behavior predicted by the 2D Rayleigh-Plesset equation described in section 6.2 (Eq. 6.2). Whereas the expansion turns out to be weak and more or less independent of the container diameter, the contraction and the closure strongly depend on it. A plausible explanation would be that, for small containers, less sand is involved in the collapse. Therefore, the hydrostatic pressure which drives the collapse is not as sustained as for a larger container, explaining why the collapse takes longer for a smaller container (Fig. 6.10).

In Fig. 6.11 we plot the closure depth $z_c$ and the closure time $t_c$. We find that $t_c$ increases and $z_c$ decreases when decreasing the container diameter. This decrease of the closure depth is generic: Also for small Fr, where $z_f$ actually increases, we find a decrease of $z_c$. The fact that a decrease of the closure depth $z_c$ implies an increase of

[¶]In our view, as the ball penetrates into the bed it pushes sand against the side walls such that a jammed region (or force network) is formed between the sphere and the walls that mediates this force.

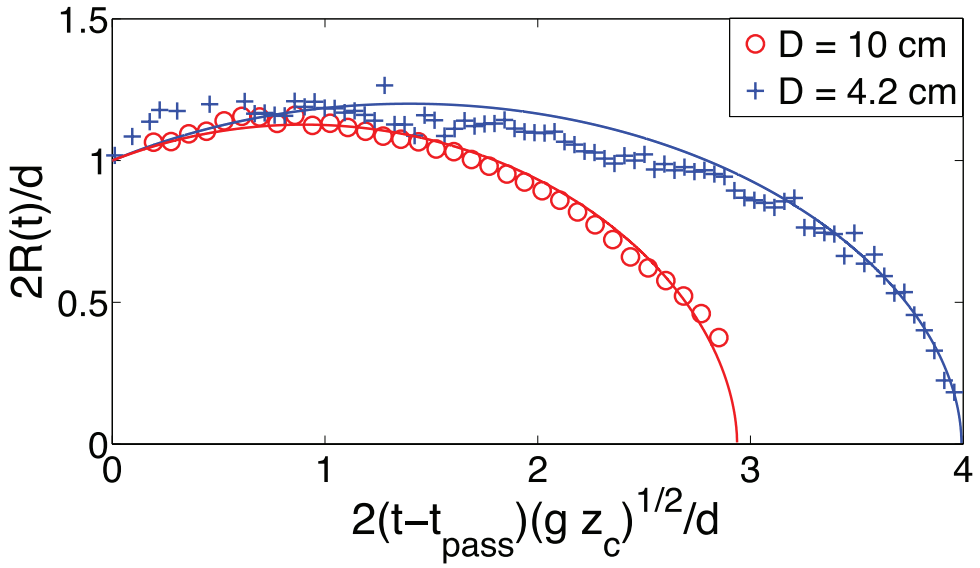


Figure 6.10: Dynamics of the cavity collapse at closure depth for two container diameters $D = 4.2$ cm (□) and $D = 10$ cm (○). Here, Fr $= 70$ and $p = 1$ bar. The time has been rescaled by multiplying with a factor $2\sqrt{gz_c}/d$ in order to show the results in a single plot. The continuous line correspond to a fit using the 2D Rayleigh-Plesset equation (Eq. 6.2).

the collapse time $t_{\text{coll}}$ can be understood from a reduction of driving pressure ($\propto gz_c$) and the availability of less sand for smaller container diameters (as explained above).

### 6.5.3 Jet Height

Now that we studied how the process of the formation and subsequent collapse of the cavity are influenced by the proximity of the side walls, we continue with the influence of the diameter of the container $D$ on the jet and, in particular, on the maximum height reached by the jet. In Fig. 6.12, the jet height $h_{\text{jet}}$ is plotted as a function of the diameter for two Froude numbers (Fr $= 25$ and Fr $= 50$) at different values of the ambient pressure. Since it was already discussed extensively in [7] that the jet becomes smaller at reduced ambient pressure, we now divide $h_{\text{jet}}$ by the jet height in the unconfined situation. We observe that, while decreasing the container diameter, the jet reaches less high. This behavior is the combined result of the reduction of the closure depth and the increase of the closure time with decreasing container diameter as was described in the previous subsection: The reduction of $z_c$ reduces the hydrostatic pressure that drives the collapse and the increase of the closure time is connected to the fact that –because of the reduced container diameter– there is less sand available during the collapse, making the driving pressure less sustained. Both factors contribute to a decrease of the jet height. The rescaling by the unconfined jet height also reveals that the influence of the boundaries is similar for all pressures and even for these two different Froude numbers. The unconfined behavior is obtained when the diameter of the container is seven times higher than the diameter of the ball.

At high Froude number (Fr = 100), the results can only be obtained for small containers, because, when the diameter is large, the jet collides with the splash which is being sucked into the cavity behind the ball at high ambient pressures. This is similar to the surface seal that has been observed for impacts on a liquid [20, 21]. For this high Froude number the results are less conclusive, as can be seen in Fig. 6.13. This is possibly due to the increased importance of the air flow caused by the ball when it is restricted to a smaller container diameter at these high impact velocities.

### 6.5.4 Granular eruption

Finally, we turn to the granular eruption that terminates the series of events. Since the container diameter has an influence on both the final depth and the closure depth, it is expected that the granular eruption will depend on the container diameter $D$. In Fig. 6.14a we report, for Fr $= 100$, the phase diagram indicating the presence of an eruption in $(p, D)$-space.[‖] There is a marked dependence on the container diameter

[‖] To obtain Fig. 6.14 the closure depths $z_c$ for the diameter of $D = 8.5$ cm (which were not measured directly) are obtained by interpolation from Fig. 6.11a.

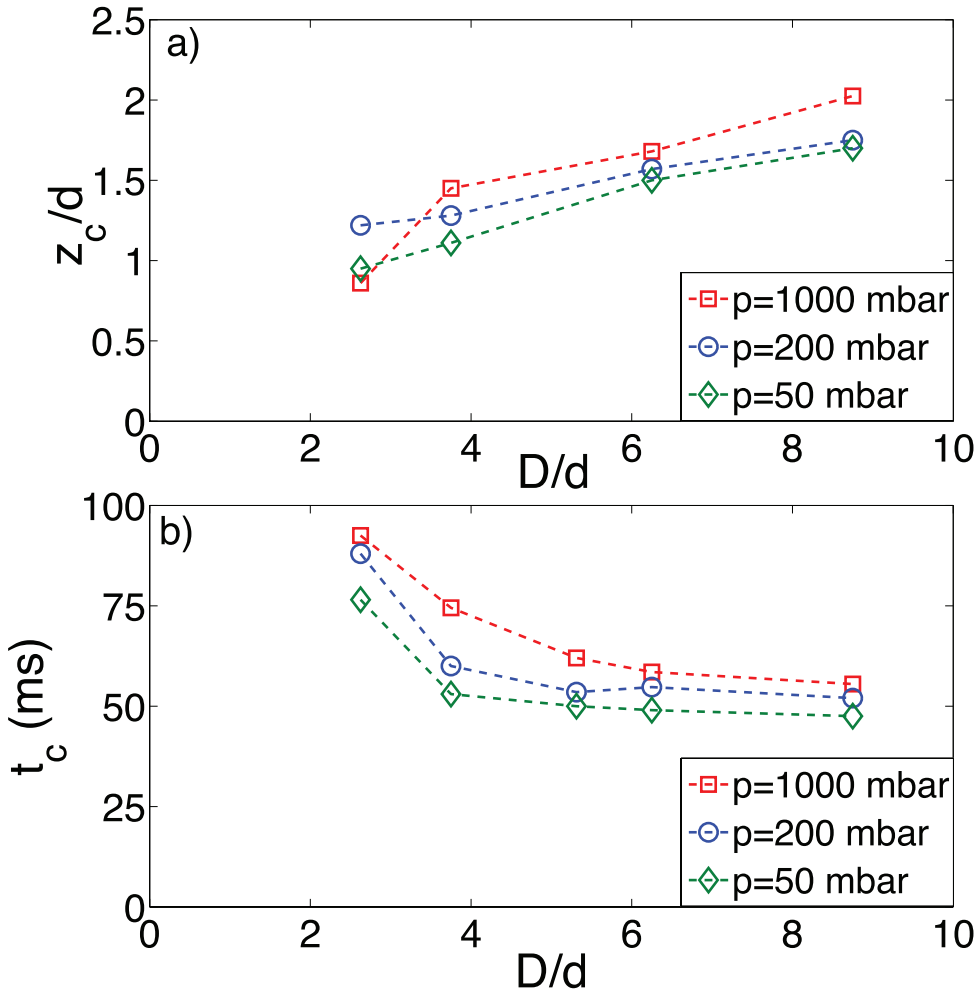


Figure 6.11: (a) Closure depth $z_c$ as a function of the container diameter $D$ for different pressures. (b) Closure time $t_c$ as a function of the container diameter $D$ for different pressures. For all measurements Fr = 70.

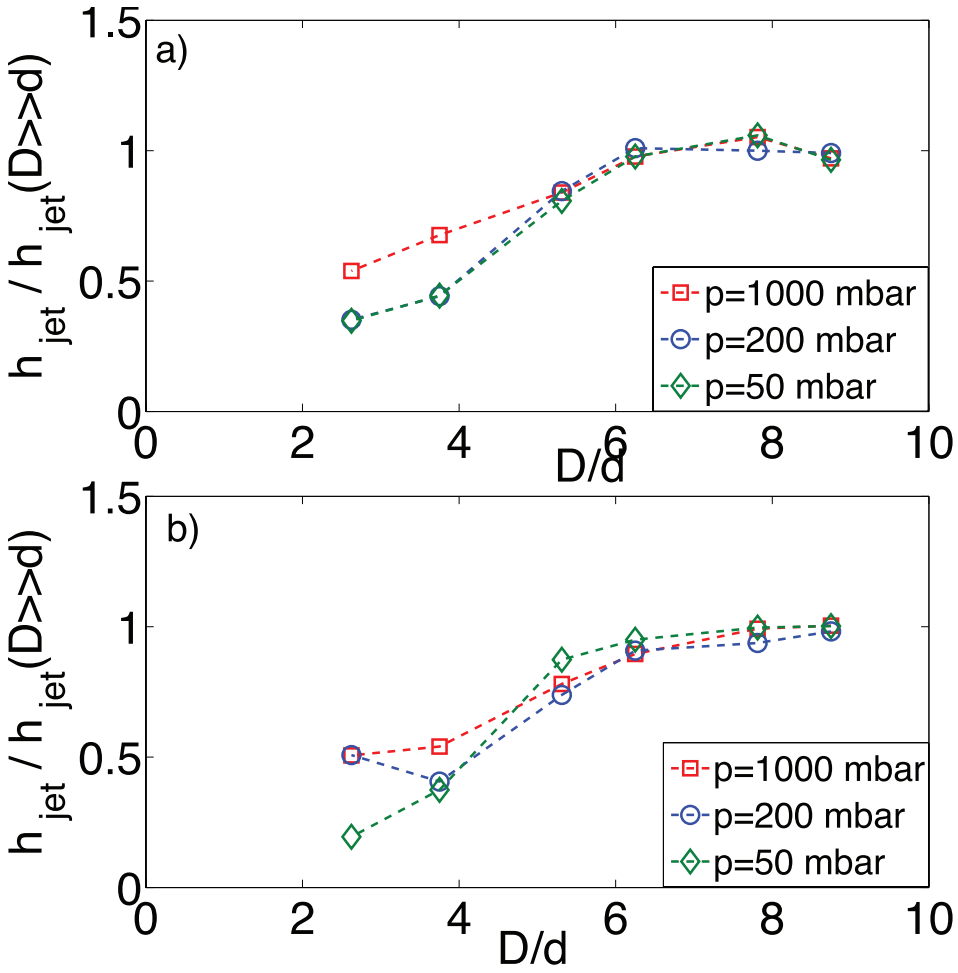


Figure 6.12: The jet height, $h_{\text{jet}}$ as a function of the container diameter $D$ for $\text{Fr} = 25$ (a) and $\text{Fr} = 50$ (b) at different ambient pressures. The jet height is divided by the jet height in the unconfined case in order to see the deviations due to the proximity of the boundaries. For all pressures and Froude numbers the jet height increases with increasing container diameter. The dashed lines are a guide to the eye to separate the measurement series at different pressures.

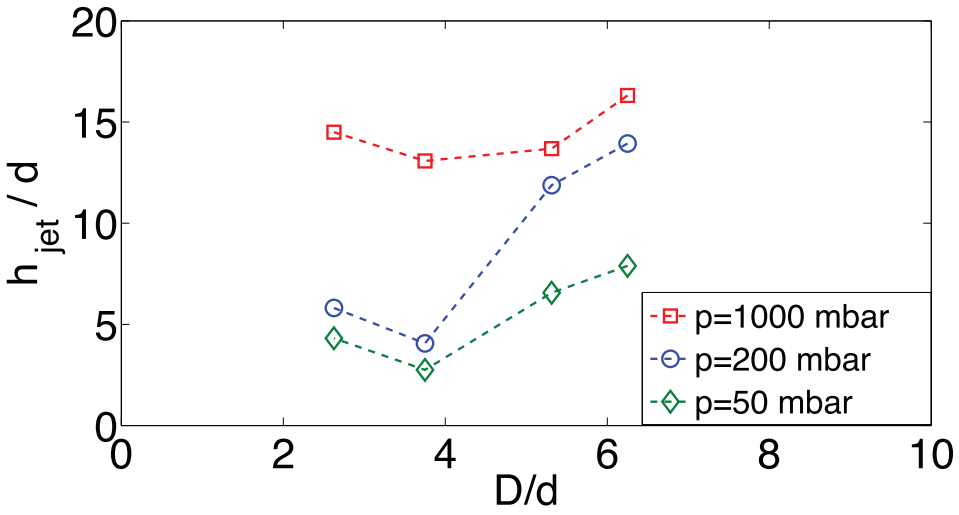


Figure 6.13: The jet height $h_{\text{jet}}$ as a function of the container diameter $D$ for Froude = 100 and different ambient pressures. Again, there is a clear change in jet height as function of container diameter. Measurements at the highest Froude numbers are not possible due to the surface seal (see text). The dashed lines are a guide to the eye to separate the measurement series at different pressures.

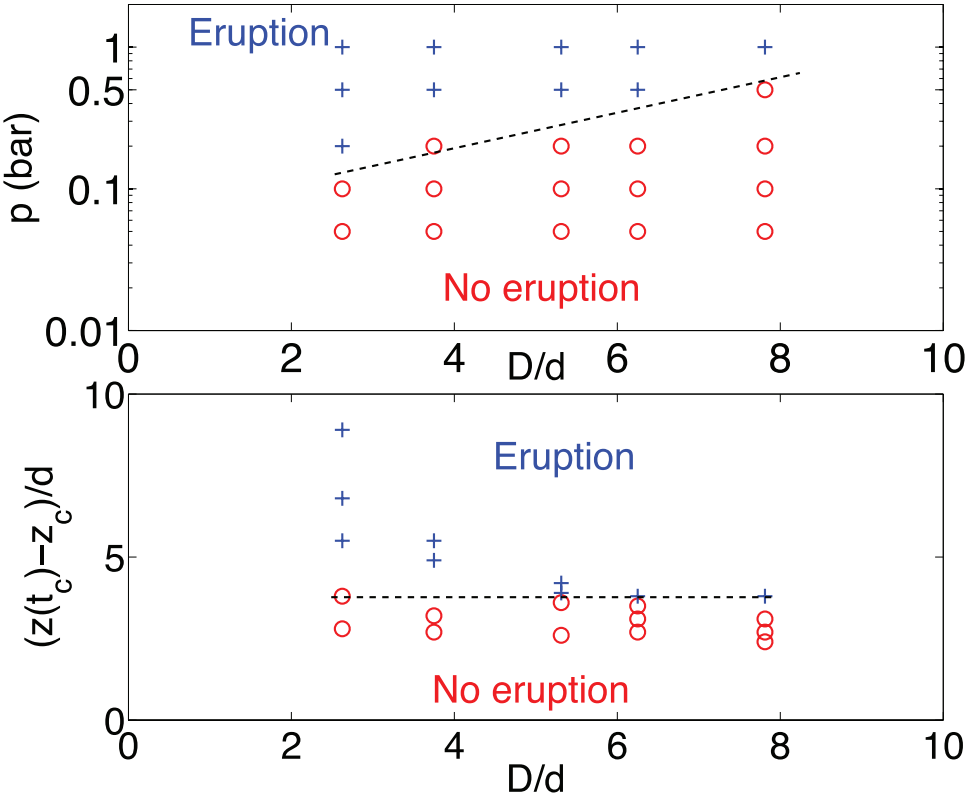


Figure 6.14: (a) Phase diagram for the granular eruption at Fr $= 100$ as a function of the pressure $p$ and the container diameter $D$. In both plots red open circles indicate parameter values where an eruption was absent, whereas blue plus signs stand for parameter values with an eruption. (b) The same phase diagram, now as a function of the volume of the entrapped air bubble ($(z(t_c) - z_c)/d$) and the container diameter $D$. The latter plot clearly indicates that the presence of the eruption is a function of the entrapped air bubble size only.

*D*: More eruptions are observed in a small container than in a large container.

This behavior can be explained using the influence of the side walls on the trajectory of the ball and on the collapse time together with the closure depth: For the same pressure, the closure time is larger, which leads to a deeper position of the ball at closure $z(t_c)$, and at the same time the closure depth is smaller, increasing the size of the entrapped air bubble for small container diameters. If we replace the pressure in Fig. 6.14a by the quantity $(z(t_c)-z_c)/d$ which is proportional to the volume of the entrapped air bubble [remember that it was argued that $V_{\text{bubble}} \sim d^2(z(t_c)-z_c)$, see Eq. (6.7), which is subsequently divided by $d^3$], we remove the dependence on *D*: In Fig. 6.14b the phase diagram is separated into two parts using a horizontal line representing a critical volume $V^* \sim 3.8d^3$. This means that, independently of the diameter of the container, the bubble volume upon its formation has to be big enough to lead to an eruption. As was explained in Section 6.4 this is because the air bubble must have sufficient time to reach the surface before it has completely dissolved into the sand bed. Incidentally, the value for the critical volume determined from the phase diagram corresponds well to the value found in Section 6.4.

## 6.6 Jet shape and thick-thin structure

The proximity of the side walls and the bottom does not only affect the height of the jet but also its shape. One of the most prominent features is the thick-thin structure first described by Royer *et al.* [4, 6] who studied the dependence of this structure on ambient pressure and Froude number. In the same work Royer *et al.* proposed a formation mechanism for the thick part of the jet based on the pressurized air bubble pushing sand into the thin jet originating from the pinch-off at the closure depth.

In this Section we report, in addition to the Froude and pressure dependence, a pronounced dependence of the thick-thin structure on the proximity of the container boundaries. We propose an alternative model for the formation of the structure which semi-quantitatively accounts for the observed behavior of the phenomenon for the entire parameter space.

### 6.6.1 Observations

In our experiments we can distinguish three different jet shapes, two of which exhibit a thick-thin structure:

(1) a ‘normal’ jet, in which the width of the jet gradually decreases from bottom to top,

(2) a thick-thin structure with a sharp shoulder, where the thick lower part abruptly changes into a thin upper part,

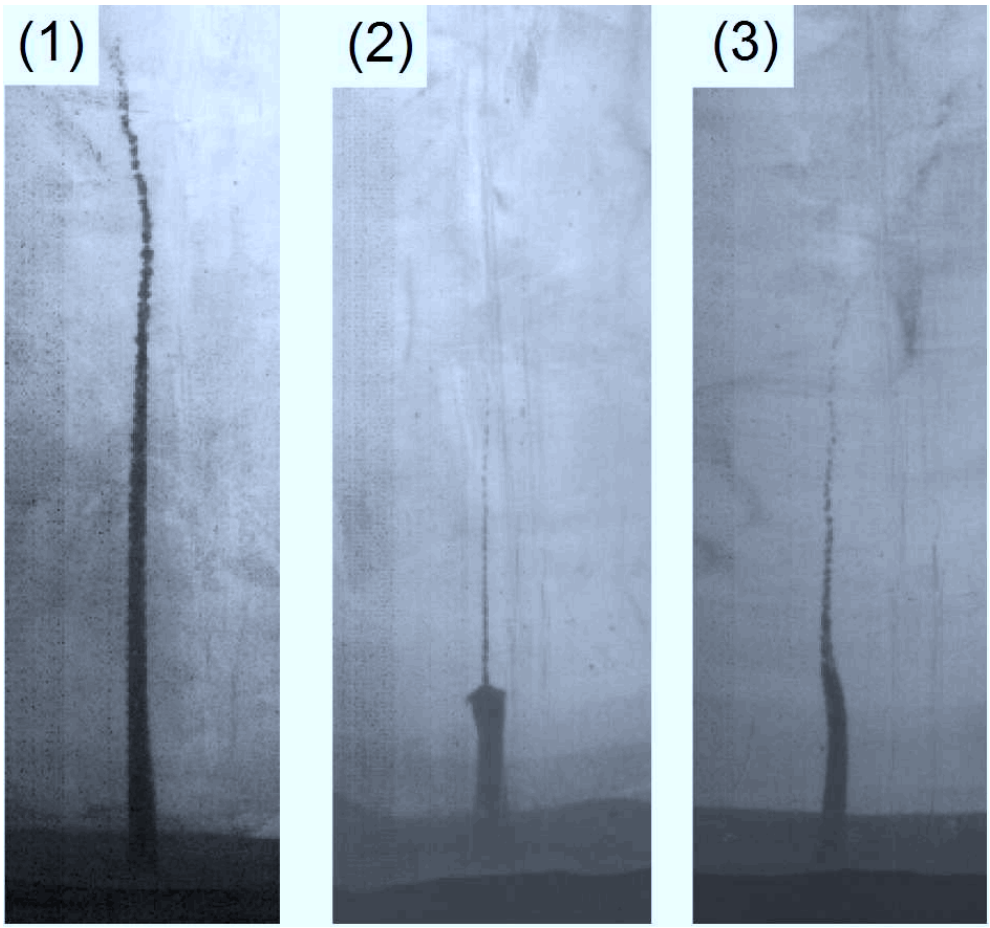


Figure 6.15: Typical snapshots of the three distinct jet shapes observed in experiment: 1) Normal jet (for $D = 10$ cm, Fr $= 100$ and $p = 1000$ mbar); 2) Thick-thin structure with sharp shoulder (for $D = 8.5$ cm, Fr $= 100$ and $p = 100$ mbar); 3) Thick-thin structure with a transition (for $D = 10$ cm, Fr $= 50$ and $p = 50$ mbar). All snapshots show the fully developed shape of the jet at its maximum height. The snapshots are not on the same scale.

(3) a thick-thin structure with a transition, characterized by a transient region in which the thick lower part gradually passes into the thin upper part.

An example of each of the three jet shapes is shown in Fig. 6.15.

First, we briefly look at the influence of the bed depth on these structures for a moderate Froude number (Fr = 70). At atmospheric pressure we observe a 'normal' jet for all values of the bed depth $h_{\mathrm{bed}}$ (Fig. 6.4). To observe a thick-thin structure we need to go to lower ambient pressures: At 100 mbar, a thick-thin structure with sharp shoulders can be observed in the unconfined case, i.e., for large $h_{\mathrm{bed}}$ (Fig. 6.15). Below a certain threshold ($h_{\mathrm{bed}} \leq 4d$), the thick-thin structure gradually disappears (Fig. 6.16). This disappearance coincides with the disappearance of the entrapped air bubble below $3d$ in which case the collapse happens more or less on top of the ball.

The effect of the proximity of the side walls (within a sufficiently deep bed) is reported in the three phase diagrams of Fig. 6.17, where the jet shapes are classified as a function of container diameter and pressure, for three different Froude numbers. For the lowest Froude number (Fr = 25), a thick-thin structure with a transition is found only for the smallest pressure at intermediate container diameter. Thick-thin structures with a sharp shoulder are not found for this Froude number. When we increase the Froude number, the thick-thin-structure region is found to grow. Within the region containing the transition variety of the thick-thin structure we observe the formation and growth of a region containing the sharp-shoulder variety. Although the thick-thin-structure region grows to include the largest container diameters that we have used in our experiment [**], thick-thin structures are never found in the smallest container diameter for the parameter space explored in this study.

Remarkably, in our experiments a granular eruption (almost) never coincides with a thick-thin structure (one can, e.g., compare Figs. 6.14a and 6.17c). Combined with the fact that a granular eruption only takes place for large entrapped air bubbles (as explained in Section 6.5.4), this implies that thick-thin structures are only formed for smaller entrained air bubbles. This in turn seems to be in contradiction with a mechanism in which the pressurized air bubble pushes up bed material that forms the thick part of the jet [6], since such a mechanism is likely to be stronger for a larger entrapped air bubble. In addition, for varying container diameter, we observe both thick-thin structures and normal jets for the same amount of entrapped air.

We will therefore in the next subsections propose an alternative mechanism for the formation of the thick-thin structures. At this point it should be stressed that there is no direct experimental evidence for the proposed mechanism as this would require the ability of imaging the events inside the sand, which until now is possible only in a small setup [6]. This issue needs to be settled in future research.

[**]Note that the largest container size (the one without an inserted cylinder) has not been included because of its square cross section, which is found to have a marked influence on the jet shape.

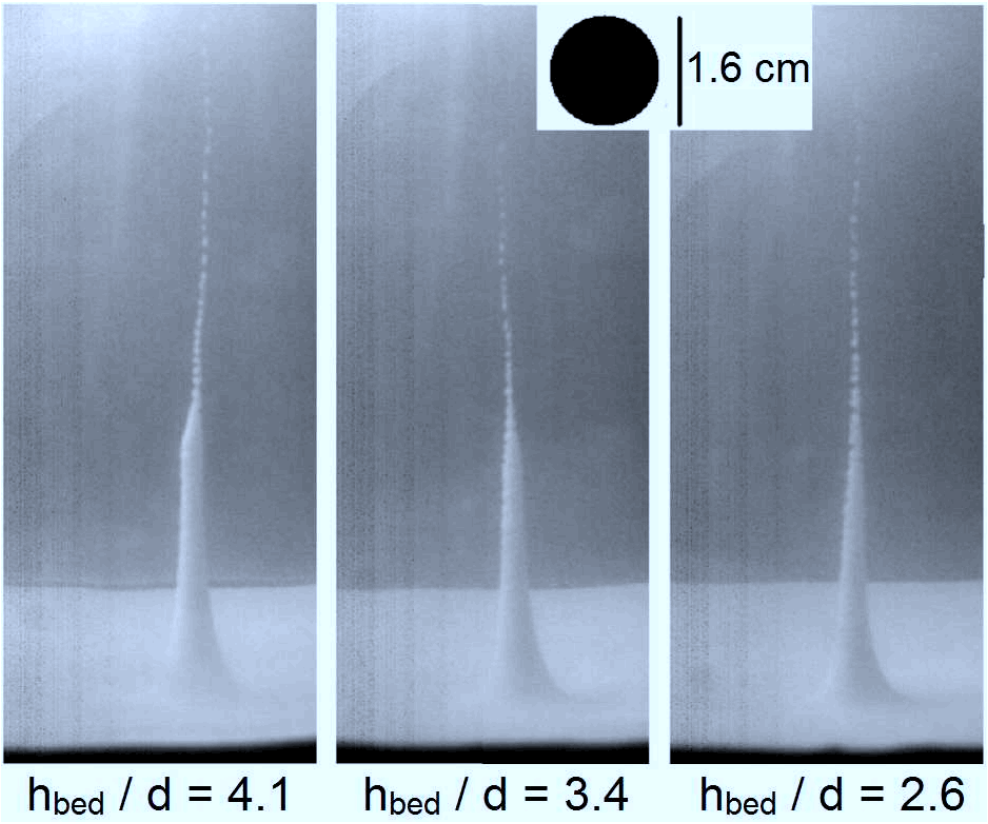


Figure 6.16: Three snapshots of the shape of the jet at different values of the height $h_{\text{bed}}$ of the sand bed, taken 120 ms after the ball impact for $p = 100$ mbar and $\text{Fr} = 70$. For $h_{\text{bed}} = 4.1\,d$ there is a clear thick-thin structure (with a transition region), which gradually disappears when the bed height is decreased to $3.4\,d$ and $2.6\,d$.

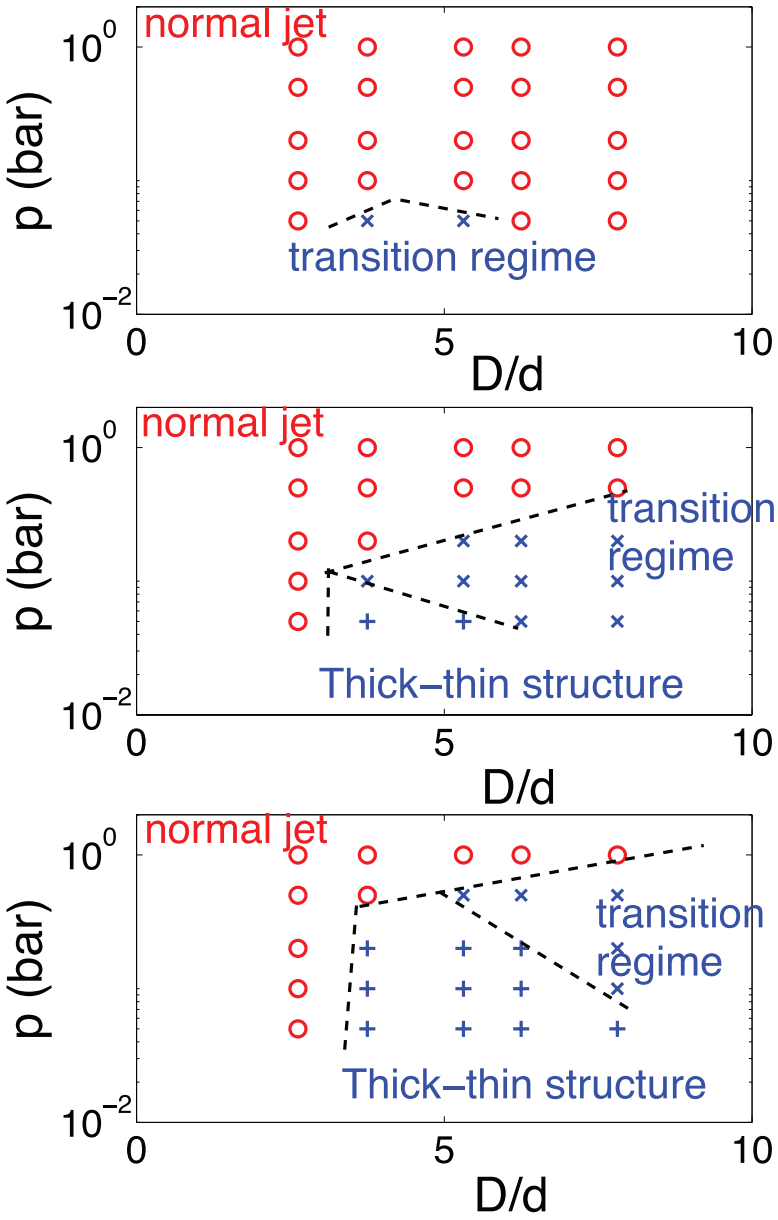


Figure 6.17: Phase diagram of the observed jet shapes as a function of the ambient pressure $p$ and the container diameter $D$ for three different Froude numbers: (a) Fr = 25; (b) Fr = 50; and (c) Fr = 100. The dashed lines are a guide to the eye to separate the different regions in the phase diagrams.

### 6.6.2 Hypothesis

We propose an alternative model for the formation of the thick-thin structures based on the hypothesis that there is a second collapse that takes place on top of the ball forming a second jet. Such a second collapse can be motivated from experiments in a quasi-twodimensional setup [18] and from X-ray measurements [4, 6], where multiple collapses have also been observed. The idea is as follows: Since the ball is still moving when the first collapse occurs (section 6.5a), the second collapse happens at a later point in time and therefore the first jet is already well on its way in the formation process when the second one is being formed. We now speculate that, if the second jet can catch up with the first fast enough, it will hit its base and produce a thick-thin structure. When the time span between the two jets is too long however, the first jet will have (almost) fully formed and the collision of the second jet with its base will not disturb its shape [††] and hence not create a thick-thin structure.

In order to test the above hypothesis, we need to estimate from our experimental data the time interval between the moment that the first jet is formed at the closure depth $z_c$ and the moment that the hypothetical second jet reaches $z_c$. This will be done in the next subsection. If the hypothesis is correct, we will find that thick-thin structures are only formed below a certain threshold value of this time interval.

This alternative model is not in contradiction with the experimental observation that a granular eruption almost never coincides with a thick-thin structure: If an eruption is observed, this means that a relatively large air bubble must have been entrapped. This concurs with a large distance between the first and the second collapse point, which makes it unlikely that a thick-thin structure will be formed. Conversely, if a thick-thin structure is observed, this means that a (relatively small) air bubble must have been pierced by the second jet, which will facilitate its dissolution in the sand.

The proposed mechanism can at least qualitatively incorporate previous experiments done in [5, 6]. They observed that the height of the thick jet decreases when the diameter of the ball or the ambient pressure decreases. Decreasing one of these parameters decreases the final depth of the ball and therefore the position of the second collapse. As the height of the jet depends on the position of the second collapse, a lower depth will result into a less high jet.

[††] At this point it is good to note that such a mechanism explains why the occurrence of a thick-thin structure never seems to interfere with the jet height: The height is determined by the free flight of the thin part which is being formed at the first closure $z_c$, i.e., before the formation of the thick part can become of influence.

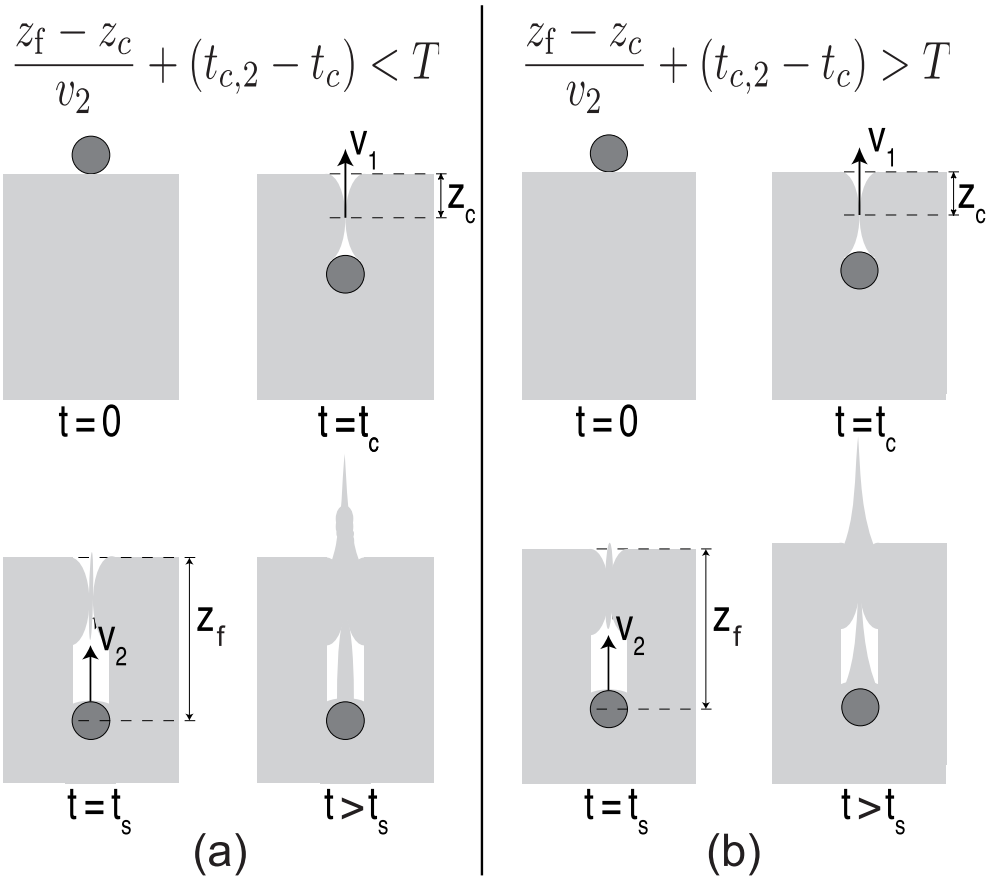


Figure 6.18: Schematic drawing of the proposed mechanism leading to the thick-thin structure. In case (a), the second collapse happens before a certain threshold time, such that the thickness of the layer of sand from the first collapse still is thin enough to be pushed up by the second jet and a thick-thin structure emerges. In case (b) we are above the threshold: The second jet collides with a thick layer of sand and is unable to disturb the formation of the first jet.

### 6.6.3 Estimating the time interval

In order to test our hypothesis, we now proceed with the estimation of the interval between the time that the first jet is formed at the closure depth $z_c$ and the moment that the second jet reaches $z_c$. This time interval consists of the difference between the two closure times $(t_{c,2} - t_c)$ (where $t_{c,2}$ is the closure time of the lower collapse), summed with the time the second jet needs to reach $z_c$, i.e., $(z_f - z_c)/v_2$ with $v_2$ the velocity of the second jet. If this time interval is shorter than some threshold value $T$, we obtain a thick-thin structure, as visualized in Fig. 6.18. This leads to:

$$\frac{z_f - z_c}{v_2} + (t_{c,2} - t_c) < T \tag{6.8}$$

Before continuing our estimate, let us first illustrate the workings of this mechanism in an example: For Fr = 75 and $p = 50$ mbar we start from the largest container size where a thick-thin structure is visible. When decreasing the size of the container, the closure depth $z_c$ and the final depth $z_f$ decrease following approximately the same behavior, such that the distance between the two collapses is more or less constant. Because $z_f$ decreases, the hydrostatic pressure and therefore the velocity of the second jet decrease as well, such that the first term in Eq. (6.8) increases. The same holds for the second term, because the closure time is found to increase with decreasing container diameter (cf. Fig 6.11b). Thus, the left hand side of Eq. (6.8) increase with decreasing the container diameter, explaining why below a certain diameter the thick-thin structure disappears.

We now approximate the several terms in Eq. (6.8) with experimentally known quantities. Because there is no direct experimental evidence for the second collapse, this involves some speculation in which we suppose that the model of section 6.2 can be extended to describe the second collapse. Doing so, in the first term of Eq. (6.8) the velocity of the second jet, $v_2$, is proportional to the square root of the driving hydrostatic pressure at depth $z_f$, i.e., $v_2 = C\sqrt{gz_f}$, with $C$ constant. Because, similarly, for the velocity of the first jet we have $v_{jet} = C\sqrt{gz_c}$, we find $v_2 \approx \sqrt{z_f/z_c}\, v_{jet}$ which is inserted into the first term of Eq. (6.8). In turn, $v_{jet}$ can be deduced from the jet height $h_{jet}$ as $v_{jet} = \sqrt{2gh_{jet}}$.

In the second term, the unknown quantity is the second closure time $t_{c,2}$ –i.e., of the cavity just above the ball– which consists of the sum of the time $t_s$ the ball needs to come to a standstill and the time $t_{coll,2}$ the cavity needs to collapse at that point. Since according to the Rayleigh model discussed in Section 6.2 the collapse times should scale as $t_{coll,2} = C'd/(2\sqrt{gz_f})$ and $t_{coll} = C'd/(2\sqrt{gz_c})$ respectively (with $C'$ constant), we have $t_{coll,2} \approx \sqrt{z_c/z_f}\, t_{coll}$. Inserting all of the above in Eq. (6.8) we

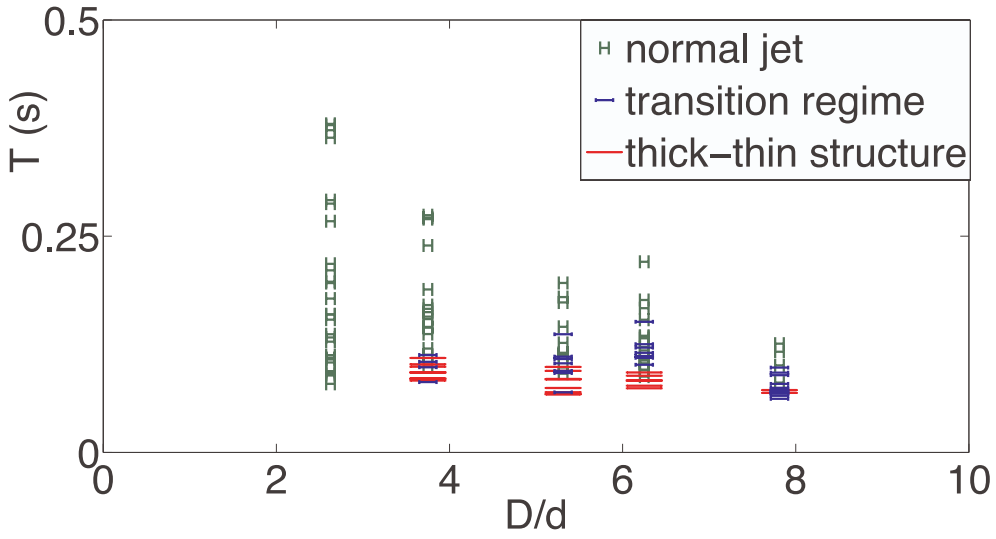


Figure 6.19: Phase diagram with on the vertical axis the left hand side of Eq. (6.9) and on the horizontal axis the container diameter $D$. The plot contains all measurements from Fig. 6.17. Short, green dashes indicate normal jets, intermediate, blue dashes the thick-thin structure with a transition, and long, red dashes thick-thin structures with a shoulder.

obtain

$$\left[\frac{z_\mathrm{f}-z_c}{\sqrt{2gh_\mathrm{jet}}}+t_\mathrm{coll}\right]\sqrt{\frac{z_c}{z_\mathrm{f}}}+(t_\mathrm{s}-t_c)<T\,. \tag{6.9}$$

In Fig. 6.19 we find a phase diagram in which all measurements from Fig. 6.17 are plotted again, but now with the left hand side of Eq. (6.9) on the vertical axis. Clearly, all thick-thin structures (intermediate and large dashes) lie below some time-threshold, in agreement with the formation mechanism discussed above. The smallest container diameter forms an exception, in the sense that here thick-thin structures are also not found for time scales where they could have been expected (i.e., that lie clearly below the threshold $T$). This behavior may be due to the fact that lack of material to sustain the collapse leads to an underestimation of the actual times in Eq. (6.9). But in general the estimate seems to work fairly well.

## 6.7 Conclusions

In conclusion, we have studied the influence of the boundaries on the various phenomena that can be observed after impact of a ball on a loosely packed sand bed: The penetration of the ball into the bed, the formation of a void, its collapse and the creation of a granular jet, the shape of the granular jet, and the presence of a granular eruption. We have shown that the observed behavior of the ball inside the sand bed and the formation and collapse of the cavity created by the ball is generally well captured by the drag law and hydrostatic collapse model of Section 6.2.

In more detail, we have shown in the first part of this study that the proximity of the bottom changes these phenomena, starting with the obvious modification of the final position of the ball, which below a certain depth just hits the bottom. The height of the jet is affected, when the void closure is constrained to happen on top of the ball. A granular eruption at the surface only happens if the volume of the entrapped air bubble is large enough, and can be fully suppressed by decreasing the height of the sand bed.

In the second part we have investigated the influence of nearby side walls. Here we find a strong influence on the drag force that the sand bed exerts on the ball when it moves through the sand bed: We find that the hydrostatic drag force component becomes less important, whereas the quadratic (velocity-dependent) component becomes more important. The latter can be traced back to the increased importance of the air flow in the container due to the confinement. Apart from the question why and how the coefficients depend on ambient pressure and container diameter, the drag model of Section 6.2 provides a quite accurate description of the observations for most of the parameter space. Only the results for the smallest container at low ambient pressure cannot be explained using this framework, due to the constant velocity plateau that is observed during the motion.

The formation and subsequent collapse of the cavity is not only influenced by the modification of the trajectory of the ball; also a smaller amount of sand is involved in its collapse which therefore takes longer for decreased container size. Apart from this, the simple hydrostatic collapse model of a cylindrical cavity presented in Section 6.2 accounts well for most of the observations. In this way, the modification of the closure time, and closure depth observed in our experiments, can be understood.

As a result of both the changes in the ball's trajectory and the smaller amount of sand that is involved in the collapse, the jet height is affected by the proximity of the wall. In the parameter range of our experiments the unconfined behavior is retrieved when the diameter of the container is larger than $7d$; this value however does seem to depend on the Froude number, and is larger when the Froude number is larger. The occurrence of a granular eruption was shown to be correlated with the size of the air bubble entrapped inside the sand bed.

Finally, this chapter culminates in the proposal of a new mechanism for the formation of the thick-thin structure, based upon a second collapse that occurs on top of the ball when it has come to a standstill. To obtain a thick part in the jet, the second jet coming from this secondary collapse needs to be formed fast enough to penetrate the rapidly growing layer of sand that is being created around the point where the first jet had originated.

## References

[1] H. Jaeger, S. Nagel, and R. Behringer, "Granular solids, liquids, and gases", Rev. mod. Phys. **68**, 1259–1273 (1996).

[2] S. Thoroddsen and A. Shen, "Granular jets", Phys. Fluids **13**, 4 (2001).

[3] D.Lohse, R. Bergmann, R. Mikkelsen, C. Zeilstra, D. van der Meer, M. Versluis, K. van der Weele, M. van der Hoef, and H. Kuipers, "Impact on soft sand: Void collapse and jet formation", Phys. Rev. Lett. **93**, 198003 (2004).

[4] J.R.Royer, E. Corwin, A. Flior, M.-L. Cordero, M. Rivers, P. Eng, and H. Jaeger, "Formation of granular jets observed by high-speed x-ray radiography", Nature Phys. **1**, 164–167 (2005).

[5] J. Royer, E. Corwin, P. Eng, and H. Jaeger, "Gas-mediated impact dynamics in fine-grained granular materials", Phys. Rev. Lett. **99**, 038003 (2007).

[6] J. Royer, E. Corwin, B. Conyers, A. Flior, M. Rivers, P. Eng, and H. Jaeger, "Birth and growth of a granular jet", Phys. Rev. E **78**, 011305 (2008).

[7] G. Caballero, R. Bergmann, D. van der Meer, A. Prosperetti, and D. Lohse, "Role of air in granular jet formation", Phys. Rev. Lett. **99**, 018001 (2007).

[8] J. Marston, J. Seville, Y.-V. Cheun, A. Ingram, S. Decent, and M. Simmons, "Effect of packing fraction on granular jetting from solid sphere entry into aerated and fluidized beds", Phys. Fluids **20**, 023301 (2008).

[9] J. S. Uehara, M. A. Ambroso, R. P. Ojha, and D. J. Durian, "Low-speed impact craters in loose granular media", Phys. Rev. Lett. **90**, 194301 (2003).

[10] M. Pica Ciamarra, A. Lara, A. Lee, D. Goldman, I. Vishik, and H. Swinney, "Dynamics of drag and force distributions for projectile impact in a granular medium", Phys. Rev. Lett. **92**, 194301 (2004).

[11] D. Lohse, R. Rauhé, R. Bergmann, and D. van der Meer, "Granular physics: Creating a dry variety of quicksand", Nature **432**, 689–690 (2004).

[12] J. R. de Bruyn and A. Walsh, "Penetration of spheres into loose granular media", Can. J. Phys. **82**, 439–446 (2004).

[13] M. Hou, Z. Peng, R. Liu, K. Lu, and C. K. Chan, "Dynamics of a projectile penetrating in granular systems", Phys. Rev. E **72**, 062301 (2005).

[14] L. S. Tsimring and D. Volfson, "Modeling of impact cratering in granular media", in *Powders and Grains 2005, Proceedings of International Conference on Powders and Grains 2005*, edited by R. García-Rojo, H. J. Herrmann, and S. McNamara, volume **93**, 1215–1218 (London: Taylor & Francis) (2005).

[15] H. Katsuragi and D. J. Durian, "Unified force law for granular impact cratering", Nature Phys. **3**, 420–423 (2007).

[16] E. L. Nelson, H. Katsuragi, P. Mayor, and D. J. Durian, "Projectile interactions in granular impact cratering", Phys. Rev. Lett. **101**, 068001 (2008).

[17] A. Seguin, Y. Bertho, and P. Gondret, "Influence of confinement on granular penetration by impact", Phys. Rev. E. **78**, 010301(R) (2008).

[18] R. Mikkelsen, M. Versluis, G. Bruggert, E. Koene, D. van der Meer, K. van der Weele, and D. Lohse, "Granular eruptions: Void collapse and jet formation", Phys. Fluids **14**, S14 (2002).

[19] S. de Vet and J. de Bruyn, "Shape of impact craters in granular media", Phys. Rev. E. **76**, 041306 (2007).

[20] D. Gilbarg and R. Anderson, "Influence of atmospheric pressure on the phenomena accompanying the entry of spheres into water", J. Appl. Phys. **19**, 127 (1948).

[21] R. Bergmann, D. van der Meer, S. Gekle, A. van der Bos, and D. Lohse, "Controlled impact of a disk on a water surface: cavity dynamics", J. FLuid Mech. **633**, 381 (2009).

# 7
# Conclusions and Outlook

The response of dense suspensions to an external force was investigated in two special experiments. Although all dense suspensions show qualitatively the same behavior in basic rheological experiments, namely slight shear thinning followed by more sudden shear thickening with increasing shear rate, in these experiments, the behavior of the suspensions was found to be very different.

In our first experiment we let objects settle in a deep bath of various suspensions (chapters 2 and 3). In every suspension but one, we observed similar behavior as in Newtonian liquids: The velocity accelerates (cq. decelerates) towards a terminal value, and the object simply stops at the bottom. Only in dense ($\phi > 0.38$) cornstarch suspensions we saw completely new phenomena, which suggest that contact forces must play an important role. First, instead of exponentially moving towards a terminal velocity, the velocity of the object actually starts oscillating between two values. In contrast to earlier work, e.g., that describing oscillations in viscoelastic liquids, these oscillations do not damp out, at least not within our experimental conditions. We found that modeling such behavior is challenging: We argue that shear thickening and viscoelastic models fail to describe the observed behavior. The most promising candidate is a hysteretic drag model, in which the system alternates between two branches of the drag force and thus between two different terminal velocities. Before either of those velocities is reached, there is a change in drag, and thus a switch to acceleration or deceleration. Details of this hysteretic drag model are still missing, such as the fact that crossover velocities have to be varied manually for different masses of the settling object, whereas it would be more logical that those would be liquid

properties. We show that the bulk oscillations are not caused by interactions with the wall, as the proximity of the walls actually damps out the oscillations. The second phenomenon is seen when the object approaches the bottom of the container, where it comes to a full stop at a short distance from the bottom. We believe this effect is caused by a layer of jammed particles between the object and the bottom. After the jamming, due to a small difference in pressure between the jammed and surrounding region, there is a flow back into the jammed layer. This layer subsequently unjams and the object reaccelerates. As only a slight decrease from jamming was needed to reaccelerate, the layer can get jammed again easily, restarting the process. This can occur several more times before actually reaching the bottom. This jamming and unjamming was modeled and we were able to reproduce the behavior very accurately for a settling cylinder, and reproduce the first cycle for a settling sphere.

Although a wide variety of parameters has been studied, and we obtained a good understanding of the effect at the bottom, a more complete understanding of the bulk oscillations is still lacking. Rheology experiments that would focus on the hysteresis may give more insight in this phenomenon. It would also be interesting to examine whether the phenomena would be visible when we would have a suspension flowing through a pipe or around an obstacle, which would be more directly applicable to industry.

In our second experiment, we exerted vertical vibrations to a thin layer of dense suspensions (chapters 4 and 5). For almost every different suspension we used, we observed a different phenomonology when vibrated. Again, a dense cornstarch suspension ($\phi > 0.37$) was found to have the richest of phenomenologies of all used suspensions: Depending on the packing fraction and the shaking parameters, we observed stable holes, rivers, jumping liquid and fingerlike protrusions. Other suspensions actually showed none of these phenomena: Polydisperse particle suspensions give holes that continuously split, collide, and merge over the entire surface of the layer. In monodisperse particle suspensions holes were found to grow over time and, depending on shaking and suspensions parameters, this hole can either grow to form a separated state (or kink) in which half of the container contains suspension, and the other half is dry. The similarity between all these phenomena is that a convection roll was observed on the edge of the liquid.

In the same experiment, we studied the dynamics of these growing holes in more detail, and compared it to collapsing holes in Newtonian liquids. We found that the closing of the hole in a Newtonian liquid is largely independent of the shaking parameters and inversely proportional to the viscosity of the liquid. When shaken, a hole was found to close on average at the same rate as it would when the liquid would be at rest. The hole size is found to oscillate around this average at the same frequency as driving. For a dense suspension containing monodisperse particles, in

the regime where the hole is found to grow, we investigated the effect of particle size and the viscosity of the liquid. We found that for lower viscosities the hole opens faster, but also the hole edge becomes less stable and is more likely to fall into the hole and close it again. The most remarkable phenomenon is that, although the hole opens, the velocity during the closing half of the cycle is actually larger than during opening. This is where the difference with the Newtonian liquid is found: Whereas the hole in the Newtonian liquid oscillates along with the driving, following an almost perfect sinusoidal pattern, the hole in the suspension oscillates in a far from symmetric manner. Not only are the peak velocities different, with a larger inward velocity, also the width of the halves are very different. The closing half is very peaked, where the opening half is more sinusoidal in shape. It was found that the results for these experiments scaled very nicely with $\mu/\sigma$, leading us to believe that due to the vertical vibrations a difference in volume fraction is created over the height of the suspension, resulting in a thin lubrication layer of suspending liquid during the opening half of the cycle. This last statement needs to be confirmed in future experiments.

The biggest question that remains after these two experiments is: What makes a cornstarch suspension so special? Their physical properties –their edgy shape and relatively flat size distribution– are unique, and were not found in other commonly available –and neither in even quite exotic– particles. But whether it is truly the geometrical properties of the cornstarch particles that sets them apart from other particle suspensions remains to be investigated thoroughly.

In chapter 6 we performed experiments in a different ‘suspension’, namely in sand (silica) particles surrounded by air. We studied the impact and settling dynamics of an object in a loosely packed sand bed of restricted dimensions. After impact, a splash is observed, which is in contrast to impact on a dense suspension. The object then penetrates further into the bed, creating a void, which will collapse under the influence of hydrostatic pressure. This collapse leads to a jet, which shoots out of the bed (which was also not observed for a dense suspension).

In this work we varied the proximity of the boundaries, namely container width and bed depth. In this experiment, we observed that the boundaries can influence the experimental results in four ways: First, by changing the object’s trajectory, which in turn influences the collapse of the formed cavity. This in turn influences the resulting jet height and shape and finally there will be an effect on the time and strength of the eruption at the very end, the surfacing bubble. The influence of the bottom on trajectory, cavity, and jet could be deduced in a straightforward manner. When the layer is shallow enough, the ball will stop on the bottom, changing the height of the collapse and thus the velocity of the jet. The influence of the side walls is more complicated. Due to the confinement, air flow caused by the object itself becomes a

more dominant factor. The object's trajectory was found to be well described by a drag law, containing a hydrostatic pressure and a quadratic drag. Only when the side walls are very close to the impact the model fails and the object reaches a temporarily constant, "terminal" velocity, before slowing down to zero.

The cavity formation and collapse is thus changed by the modification of the trajectory of the ball. But, in addition, also the amount of sand involved in the collapse changes the dynamics and therefore the resulting jet height. When the object penetrates very far into the bed, a second collapse will happen, much deeper in the bed. When this second jet overtakes the first jet, which can happen due to a more violent collapse, a very remarkable jet structure can be formed, in which there is a broad shoulder separating a thin jet from a very broad jet. We created a model that predicts when this second jet will influence the shape of the jet we observe above the bed surface.

The eruption, which is caused by an entrapped air bubble after pinch off rising to the surface, was found to depend on the size of the bubble, and the dissolving time. This causes the eruption to alternately be not visible and visible two times, when increasing the sand depth.

In the settling experiments in our two "suspensions", cornstarch in water and sand in air, we can find similarities and differences. Both experiments lead to behavior different from that in a Newtonian liquid, but the observed behavior is very different in the two materials. Whereas, there is a sort of constant velocity in cornstarch, there is a continuous decrease in velocity for the granular case.

A similarity is that in both systems, the objects eventually stops because of jamming. In both baths, the movement of the object causes a change in packing fraction in front of it until jamming is reached. The difference is that for the granular bed, this happens somewhere in the bulk, whereas this only happens close to the bottom for the cornstarch suspension. The reason for this is the difference in surrounding liquid. Water is strong enough to counteract this increase in packing fraction, whereas air is not. This also explains why this behavior only happens close to the bottom for cornstarch, and why unjamming takes place after the object comes to a stop.

Research on the granular jet now turns to the observation of what happens inside the sand bed, using X-ray technology and pressure measurements. With these techniques we can get a better view of the processes inside the bed, which was not possible in the experiments that were done for this thesis.

# Summary

In this thesis, we studied the response of dense suspensions to an external force in two different experimental situations.

In our first experiment we let objects settle in a deep bath of a dense cornstarch suspension. Here, we observed two unexpected phenomena: First, instead of exponentially moving towards a terminal velocity, like in a Newtonian fluid, the velocity of the object actually starts oscillating between two values. In contrast to earlier work, e.g., that describes oscillations in viscoelastic liquids, these oscillations do not damp out, at least not within our experimental conditions. We found that modeling such behavior is challenging: We argue that shear thickening and viscoelastic models fail to describe the observed behavior. A hysteretic drag model proved to come closest to our experimental results. In this model the system alternates between two branches of the drag force and thus alternatively moves towards two different terminal velocities. Before either of those velocities is reached, there is a change in drag, and thus a switch to acceleration or deceleration.

The second phenomenon is encountered when the object approaches the bottom of the container, where it comes to a full stop at a short distance from the bottom. We believe this effect is caused by a layer of jammed particles between the object and the bottom. We argue that after the jamming, due to a small difference in pressure between the jammed and the surrounding region, there is a flow back into the jammed layer. The layer subsequently unjams and the object reaccelerates. As only a slight decrease in packing fraction from the jammed state was needed to reaccelerate, the layer easily gets jammed again, restarting the process. This cycle can repeat several more times before actually reaching the bottom. This jamming and unjamming cycle was modeled, and we were able to reproduce the behavior quite accurately.

In our second experiment, we exerted vertical vibrations to a thin layer of dense suspensions. In testing various particle suspensions, a dense cornstarch suspension was found to have the richest of phenomenologies of all used suspensions. Depending on the suspension type and the shaking parameters, we observed stable holes, rivers, jumping liquid, fingerlike protrusions, splitting and colliding holes, and growing holes and kinks. The similarity between all these phenomena is that a convection roll was observed on the edge of the liquid.

We studied the dynamics of the growing holes in more detail, and compared it to collapsing holes in viscous Newtonian liquids. We found that the gravity-driven closing of the hole in a Newtonian liquid is largely independent of the shaking parameters and inversely proportional to the viscosity of the liquid. When shaken, a hole was found to close at the same rate as it would when the liquid would be at rest, with an additional oscillation of the hole edge at the driving frequency. This behavior, including both the closing and the oscillations, was modeled with a lubrication model.

For a dense suspension containing monodisperse particles, we investigated the effect of particle size and the viscosity of the liquid, in the regime where the hole is found to grow. We found that for lower viscosities of the suspending liquid the hole opens faster, but also the hole edge becomes less stable and is more likely to fall into the hole and close it again. The most remarkable phenomenon is that, although the hole opens, the maximum velocity during the closing half of the cycle is actually larger than during opening. The hole in the suspension oscillates in a far from symmetric manner, which is markedly different from the Newtonian case. Not only the peak velocities are different, also the shape of the two halves differ significantly. The closing half is very peaked, whereas the opening half is more sinusoidal in shape. It was found that the results for these experiments scaled very nicely with $\mu/\sigma$, leading us to believe that due to the vertical vibrations a difference in volume fraction is created over the height of the suspension, resulting in a thin lubrication layer of suspending liquid during the opening half of the cycle.

We also performed experiments in a granular material that is related to a suspension, namely in very fine, loosely packed sand (silica) particles surrounded by air. When an object impacts on such a sand bed, a cavity is known to be formed, which subsequently collapses, leading to the formation of a jet. We studied the impact and settling dynamics of an object in a sand bed of restricted dimensions.

We observed that the boundaries can influence the experimental results in four ways: First, by changing the object's trajectory, which in turn influences the collapse of the cavity that is formed after impact. This in turn influences the resulting jet height and shape and finally there will be an effect on the time and strength of the eruption at the very end, caused by a surfacing air bubble.

The influence of the bottom on trajectory, cavity, and jet could be deduced in a straightforward manner. When the layer is shallow enough, the ball will stop on the bottom, changing the height of the collapse and thus the velocity of the jet.

The influence of the side walls is more complicated. Due to the confinement, air flow caused by the object itself becomes a more dominant factor. The object's trajectory was found to be well described by a drag law, that contains a hydrostatic pressure and a quadratic drag term. Only when the side walls are very close to the impact the

model fails and the object reaches a temporarily constant, “terminal” velocity, before slowing down to zero.

The cavity formation and collapse is thus changed by the modification of the trajectory of the ball, and in addition, also the amount of sand involved in the collapse changes the dynamics and therefore the resulting jet height. When the object penetrates very far into the bed, we argue that a second collapse will happen, much deeper in the bed. When this second jet overtakes the first jet, a very remarkable structure can be formed, in which there is a broad shoulder separating a thin jet on top of a very broad jet at the bottom. We presented a quantitative argument to predict when this second jet will influence the shape of the jet we observe above the surface of the bed.

The eruption, which is caused by an entrapped air bubble after pinch off rising to the surface, was found to depend on the size of the bubble, and the dissolving time. This causes the emergence of alternating regimes with and without eruptions, while increasing the depth of the sand bed.

# Samenvatting

In dit werk hebben we gekeken naar het gedrag van geconcentreerde suspensies wanneer er een externe kracht op wordt uitgeoefend. Alle geconcentreerde suspensies vertonen kwalitatief hetzelfde gedrag in standaard rheologische experimenten, namelijk een afname van de viscositeit (shear thinning), gevolgd door een meer abrupte toename van de viscositeit (shear thickening) wanneer de afschuifsnelheid op de vloeistof toeneemt. In onze experimenten bleek dat het gedrag van verschillende suspensies ook zeer verschillend uitpakte. Wij hebben onderzocht hoe in hoeverre de dynamica van de deeltjes in de suspensies dit gedrag kan verklaren.

In ons eerste experiment lieten we objecten zinken in een diep bad van een suspensie onder invloed van zwaartekracht (hoofdstukken 2 en 3). In elke suspensie, behalve één, zagen we hetzelfde gedrag wat we ook zien in Newtoniaanse vloeistoffen, namelijk een snelheid, die naar een terminale snelheid convergeert. Deze snelheid zal aangehouden worden tot de bodem wordt bereikt. Alleen in geconcentreerde ($\phi > 0.38$) suspensies van maïzena observeerden we een aantal nieuwe fenomenen. Het eerste fenomeen is dat het object geen terminale snelheid bereikt, maar dat de snelheid afwisselend toe- en afneemt, en daarbij tussen twee waarden heen en weer blijft schommelen. In andere complexe vloeistoffen zijn ook oscillaties waargenomen, maar deze dempten echter snel uit, terwijl de oscillaties die wij waarnemen als eigenschap hebben dat ze niet noemenswaardig uitdempen in ons experiment. Dit gedrag bleek zeer moeilijk te modelleren. We tonen aan dat shear thickening en viscoelasticiteit dit gedrag niet kunnen beschrijven, aangezien deze respectievelijk leiden tot een enkele curve die de weerstand beschrijft en gedempte oscillaties, beide in tegenspraak met onze experimenten. Het dichtste bij het modelleren van deze experimenten komen we door een model te gebruiken met een hysteretische weerstand. In dit model wordt aangenomen dat de suspensie twee verschillende weerstanden kan aannemen, afhankelijk van de snelheid en de geschiedenis van de snelheid. Doordat er twee snelheden zijn waarbij er tussen deze twee weerstanden wordt gewisseld komen we inderdaad uit bij een oscillerende snelheid. Het nadeel van dit model is echter dat we voor elk experiment deze snelheden moeten herdefiniëren, waar we eigenlijk verwachten dat deze alleen afhankelijk van de suspensie zouden zijn.

Het tweede fenomeen nemen we waar wanneer het object de bodem nadert. Het

object stopt al enkele centimeters voor het bereiken van de bodem, doordat er zich een vaste laag van deeltjes bevindt tussen het object en de bodem (jamming). Na deze stop stroomt er echter vloeistof terug in dit gejamde gebied waardoor het object weer kan accelereren. Doordat het object verder zinkt vormt er zich opnieuw een gejamde laag tussen object en bodem waardoor dit proces zich nog enkele malen zal herhalen totdat de bodem wordt bereikt. Dit proces hebben we gemodelleerd en de resultaten kwamen zeer goed overeen voor een experiment met een cilinder, en kwamen voor een bal in elk geval goed overeen voor de eerste cyclus.

Ondanks dat we een grote hoeveelheid parameters hebben gevarieerd, is het oscilleren van de snelheid in de bulk van de suspensie nog niet geheel begrepen. Waarschijnlijk kunnen rheologische experimenten die zich concentreren op hysterese meer inzicht geven in deze oscillaties. Daarnaast zou het interessant zijn om te zien of hetzelfde fenomeen optreedt wanneer we een soortgelijk experiment zouden herhalen, maar dan door suspensies door een pijp te laten stromen, of bij stroming van suspensies rondom een object, zeker aangezien deze experimenten dichterbij toepassingen in de industrie zullen staan.

In ons tweede experiment, hebben we dunne lagen van geconcentreerde suspensies verticaal laten trillen (hoofdstukken 4 en 5). Wanneer je in een vloeistof in rust een gat maakt zal dit snel weer dichtgaan. Dit is echter niet het geval in suspensies, wanneer deze verticaal trillen. Voor bijna elke suspensie die we gebruikt hebben, vinden we verschillend gedrag in dit experiment. Opnieuw zien we dat een geconcentreerde suspensie van maïzena ($\phi > 0.37$) de rijkste fenomenologie vertoont. Afhankelijk van de eigenschappen van de maïzena suspensie en de frequentie en amplitude van de aandrijving, zien we stabiele gaten, rivieren, rondspringende klodders en vingervormige groeisels. Andere suspensies daarentegen vertonen deze fenomenen niet, maar laten weer andere opmerkelijke gedragingen zien. Wanneer een suspensie polydisperse deeltjes bevat zien we gaten die zich in de loop van de tijd continu blijven delen, maar ondertussen ook botsen met elkaar en daardoor samensmelten of dichtvallen. In suspensies met monodisperse deeltjes zien we dat gaten groeien tijdens het experiment. Wanneer dan de rand van de container wordt bereikt opent dit gat zich, waarna de ene helft van de container droog valt en de andere helft alle suspensie bevat. De overeenkomst tussen al deze fenomenen is dat op de overgang van een droog deel naar de suspensie zich altijd een convectierol bevindt.

In ditzelfde experiment hebben we ook specifiek gekeken naar de dynamica van deze groeiende gaten in suspensies en naar sluitende gaten in Newtonse vloeistoffen. Het dichtvallen van een gat in een Newtonse vloeistof blijkt alleen af te hangen van de viscositeit van de vloeistof; het maakt daarbij niets uit of de vloeistof ondertussen trilt of niet. Wanneer er getrild wordt, zien we wel dat de rand van de vloeistof met dezelfde frequentie en sinusvorm oscilleert als waarmee de gehele vloeistof getrild

wordt. De trilling van de rand van de vloeistof loopt wel een kwart periode achter op de trilling van het systeem. Dit systeem hebben we ook kunnen modelleren met behulp van lubricatie theorie en de resultaten hiervan komen zeer goed overeen met de experimenten.

Voor een sterk vibrerende, geconcentreerde suspensie met monodisperse deeltjes groeit een gat gedurende de tijd. We hebben in dit regime de invloed van de grootte van deeltjes en de viscositeit van de vloeistof onderzocht. Ook in deze experimenten trilt de rand van de vloeistof weer met dezelfde frequentie als waarmee we het systeem aandrijven en het faseverschil was voor alle experimenten ook hier weer een kwart periode. Een lagere viscositeit leidt tot een sneller groeiend gat, maar maakt deze ook minder stabiel. Dit komt doordat de rand van het gat verder boven het oppervlak uitsteekt en daardoor een grotere kans heeft om in het gat te vallen en deze daardoor te doen sluiten. Het meest opmerkelijke in dit experiment is dat, ondanks dat het gat opent, de snelheid tijdens het naar binnen bewegen hoger is dan tijdens het naar buiten bewegen. Dat het gat toch groeit, komt doordat de vorm van het snelheidsprofiel zeer gepiekt is gedurende het sluiten, en de sluitsnelheid daardoor gemiddeld toch lager uitvalt dan de gemiddelde openingssnelheid. De resultaten van het openen van de gaten en de snelheid waarmee dit gebeurt, vallen voor al onze experimenten, met verschillen viscositeiten en deeltjesgroottes heel goed over elkaar als we de viscositeit schalen met de deeltjesgrootte. Dit betekent volgens ons dat er een verschil in deeltjesconcentratie zit over de hoogte van de suspensie. Deze aanname zal in toekomstige experimenten nog moeten worden bevestigd.

De grootste vraag die overblijft is waarom maïzena in water een zo speciale suspensie vormt. Zowel bij het vibreren als bij het zinken vonden we hier de rijkste fenomenologie. Het kan zijn dat de unieke geometrische eigenschappen van de maïzenadeeltjes, hoekige vormen en de grootteverdeling, niet eenvoudig te vinden zijn in andere deeltjes.

We hebben onze zinkexperimenten herhaald in een granulair materiaal dat overeenkomsten vertoont met een suspensie, namelijk een los gestapeld bed van fijne zandkorrels in lucht. In dit experiment hebben we het inslaan en zinken van een bal in een bad van dergelijk droog drijfzand beschreven (hoofdstuk 6). Na inslag op het zand zinkt de bal in het bed en laat hierbij een cilindervormige opening achter. Deze valt dicht door de hydrostatische druk en leidt tot de vorming van een jet die uit het bed omhoog schiet.

In dit werk hebben we gekeken naar de invloed van de containerwanden en de bodem op de vorm en hoogte van deze jet en het zinkgedrag van de inslaande bal. We observeren dat de wanden onze experimenten op vier manieren kunnen beïnvloeden. Als eerste zal het traject van de bal veranderen, wat op zijn beurt invloed heeft op het dichtvallen van de opening in het zand die in het zog van de bal achterblijft. Hierdoor

zal de jet niet allen in hoogte, maar ook van vorm veranderen. Tot slot is er nog invloed op de eruptie die plaatsvindt wanneer de achtergebleven lucht in het bed het oppervlak bereikt.

De invloed van de aanwezigheid van de bodem was redelijk eenvoudig te verklaren. Doordat de bal stopt op de bodem zal er een kleinere opening worden gemaakt in het zand waardoor ook de jet minder hoog reikt. De invloed van de zijwanden is complexer. Door de kleinere container wordt de invloed van de luchtstroom, gecreëerd door de bal zelf, een zeer belangrijke factor in het resulterende traject. Het traject blijkt goed te beschrijven met een model dat de hydrostatische druk en een kwadratische weerstand op de snelheid bevat. Alleen onder speciefieke experimentele omstandigheden, vertoont het object een onverwacht resultaat, waarbij zelfs voor korte tijd een terminale snelheid wordt bereikt. De door de bal gemaakte opening en het dichtvallen hiervan wordt hierdoor ook veranderd, maar ook de veranderende hoeveelheid zand in een kleinere container heeft invloed op de uiteindelijke jet die wordt gevormd. Tot slot is er nog beredeneerd dat wanneer de bal diep genoeg komt er een tweede, diepere plaats is waar de opening dichtvalt. Hierdoor zal er een tweede jet ontstaan, die afhankelijk van de experimentele variabelen al dan niet de eerste jet kan inhalen. Wanneer dit het geval is zal de uiteindelijke zichtbare jet boven het oppervlak een zeer specifieke structuur hebben met een smal deel aan de bovenkant, gevolgd door een abrupte verbreding naar een bredere basis.

De eruptie die het experiment beëindigd bleek afhankelijk te zijn van de balans van twee tijdschalen, namelijk hoe snel de luchtbel naar het oppervlak komt tegenover de tijd die nodig is voor deze bel om op te lossen in het bed.

# Acknowledgements

All the work I did in the past 4 years could not be done without the help and support of a fantastic group to work in. Let me start with thanking prof. Detlef Lohse for offering me the chance to do a PhD in his group. It was great that he showed his trust in my abilities even far before my Master thesis was finished. Besides that, his insights in everything related to fluids is amazing and always can give you new paths to explore. His short comment: ”What will happen if we drop a ball in a cornstarch suspension” actually became a big part of this work.

Then I would like to thank prof. Devaraj van der Meer, my first supervisor, for all his guidance during these four years (5 if you include the Master project as well). You always could find a minute to answer a quick question, and also our weekly discussions always brought new ideas and helped removing obstacles in my way.

During one of the first meetings, dr. Jacco Snoeijer asked whether he could join as well, as he showed to be very interested in this field of work. A lot of credit goes to him as well for all the results we obtained. His more theoretical point of view helped me a lot. He also found ways to make my mess of equations presentable.

For their parts in the granular jet part of the thesis I want to thank dr. Sylvain Joubaud and dr. Gabriel Caballero-Robledo. Gabriel, you were already finishing up your work and leaving for a new position in Mexico, but your expertise gave me a nice start for this work. Sylvain, you were a lot of fun to work with, or have a fun non-work related discussion. Without your work, I believe that the granular jet chapter would have looked quite different.

A lot of credit also should go to my two master students, Matthias van de Raa and Stef Carelsen who helped with some of the experiments in this thesis. Matthias deserves it for his work on the growing holes in the suspensions with the polystyrene beads and Stef for his work on the linear motor experiments, pushing objects through cornstarch suspensions. It is too bad that this nice work was not finished in time to be included in this thesis.

Off course, every project needs funding, and in my case I would like to thank FOM for the financial support and also for the courses and meetings they organized. Thanks to you I met a lot of other young scientists and I received some extra preparation for the future.

My work was part of a larger project, called Rheophysics: Connecting Jamming and Rheology. I want to thank all other professors, post-docs and PhDs that were part of this larger project, and for the discussions and fun we had during our meetings.

As I said in the beginning, the whole group contributes to everybody's work, so I want to thank everybody in our group; starting with the technicians Bas, Gert-Wim and Martin for the help with setups and computers and our secretary Joanita for all administrative work she has done.

I want to thank everybody I shared a room with during these four years; Todd, Tuan, Shing, Yoshi and Bram. Besides this I want to thank all other group members, scientific staff, postdocs, PhDs, and all Master and Bachelor students. A fun group of people to work with makes it worth the long trip to the office every day.

I want to thank all my former student friends, whether we are still in contact or not. My 9.5 years in Enschede were great, even though I never actually lived there. Extra credit goes to the ones who joined in on a friendly game of toepen.

During working hours it was always nice to have some relaxation as well, this was done with the internal futsal competition, so I want to thank all soccer players that joined me on the field, and off course our opponents as well, as without them there would be no match to play. An extra thank you to Arjan and Erik-Jan for making me captain, and for taking over respectively.

Finally I want to thank my parents, my sister and her husband for all support and motivation to push myself to the limits. I thank my friends at home for all enjoyable weekends, a nice contrast to the working week. Last and not least thanks to Jeanine, after 9.5 years, I can not imagine life without you.

# About the author

Stefan von Kann was born the 13th of November 1985 in Winterswijk, the Netherlands. He finished his high school education in 2003 at the RKSG Marianum in Groenlo. The same year he started with his study Applied Physics at the University of Twente in Enschede. During his education he did a minor in Economy and Business, and did a 3 month internship at ECN in Petten, the Netherlands. There he worked on thermoacoustics, a way of cooling using sound waves. He obtained his MSc. degree in 2008 with an experimental study of granular jets in the Physics of Fluids group of Prof. Detlef Lohse under supervision of Dr. Devaraj van der Meer. After that, he continued as a Ph.D. in the same group, studying the non-Newtonian behavior of dense suspensions when a force is applied to them.